The Dissertation Committee for Mason Joseph Fried certifies that this is the approved version of the following dissertation:

Dynamic changes at tidewater glacier termini in central west Greenland

Committee:

Ginny A. Catania, Supervisor

John W. Holt

Jacob I. Walter

Wonsuck Kim

Patrick Heimbach

Dynamic changes at tidewater glacier termini in central west Greenland

by

Mason Joseph Fried

Dissertation

Presented to the Faculty of the Graduate School of

The University of Texas at Austin

in Partial Fulfillment

of the Requirements

for the Degree of

Doctor of Philosophy

The University of Texas at Austin

May 2018

Dedication

To Timothy Foley and Morris Fried, who would have loved to go on this exploration.

"And you may ask yourself, well,

how did I get here?"

David Byrne

Acknowledgements

I completed this dissertation with the help and support of many. I thank my advisor, Ginny Catania, for giving me the opportunity, guidance and freedom to explore important questions. Her strength is continuously inspiring. As I like to say, she also got me to Austin. I would like to thank my committee members, Jack Holt, Jake Walter, Wonsuck Kim and Patrick Heimbach for their help, generosity and valuable scientific insights. I've benefitted greatly from a broad, interdisciplinary group of collaborators including Timothy Bartholomaus, Dan Duncan, Leigh Stearns, Dustin Carroll, Dave Sutherland, Emily Shroyer, Jonathan Nash, and Marcy Davis. I couldn't ask for a better group of colleagues, friends and field accomplices. Cheers. To my mentors who played such a large role in getting me here, Christina Hulbe and Eugene Domack: thank you.

Many others deserve sincere thanks. My family, Jane, Stephen and Hope Fried have always made me strong. Reed helped me love Austin and Texas and proved to be an excellent friend and musician. David Conwell undoubtedly set the town on fire. As always, I thank Christian Kunhardt for thinking of better things. I shared wonderful experiences with many fellow graduate students, including those in my research group, Denis Felikson, Lauren Andrews, Liz Logan, and Sophie Goliber. In particular, Denis Felikson was always there for advice when it was needed most. Finally, I want to thank Casey O'Brien for her support and so many wonderful memories. It's been great.

Much of this work was supported by NASA grant NNX12AP50G. I also benefitted from several fellowships, including the Eqing/Worzel fellowship from the University of Texas Institute for Geophysics.

Dynamic changes at tidewater glacier termini in central west Greenland

Mason Joseph Fried, Ph.D.

The University of Texas at Austin, 2018

Supervisor: Ginny A. Catania

The Greenland Ice Sheet rapidly lost mass over the last two decades, in part due to increases in ice loss from termini of large tidewater glaciers. Terminus melting and calving can drive glacier retreat and the pattern of ice sheet mass loss through reductions in resistive stresses near the glacier front and, in turn, increases in ice flow to the ocean. Despite their importance to ice sheet mass balance, factors controlling terminus positions are poorly constrained in ice sheet models, which fundamentally obscures sea level rise predictions.

In this dissertation, I use a suite of novel observations and techniques to quantify controls on frontal ablation and terminus positions at tidewater glaciers in central west Greenland. Until recently, frontal ablation processes were obscured due to limited observations of submarine termini. Here, I use observations from multibeam echo sonar to show the morphological complexity of the submarine terminus face and identify previously unrecognized melting and calving processes. The terminus features numerous secondary subglacial plume outlets outside of the main subglacial channel system that

drive and disperse large submarine melt rates across the glacier front. Submarine melting drives steep, localized terminus undercutting that can trigger calving by connecting to finely-spaced surface crevasses. In turn, large calving events cause the terminus face to become anomalously overcut. Incorporating observed outlet geometries in a numerical plume model, I estimate small subglacial discharge fluxes feeding secondary plume outlets that are reminiscent of a distributed subglacial network. Regional remote-sensing observations reveal that, for most glaciers in central west Greenland, seasonal terminus positions are more sensitive to glacial runoff than ice mélange or ocean thermal forcing. Shallow, serac-failing tidewater glaciers are most sensitive, where subglacial plumes melt the terminus and locally enhance retreat. Glaciers with large ice fluxes and deep termini retreat sporadically through full ice-thickness calving events less dependent on runoff. Together, these results provide process-oriented constraints on the shape of the submarine terminus face, the geometry of subglacial discharge and submarine melting, the influence of environmental forcing mechanisms and the impact that these variables have on terminus positions and dynamics in a warming climate.

Table of Contents

List of Tables

List of Figures

Chapter 1. Introduction

1.1. Background

Understanding physical process underlying systems considered vulnerable to rapid climate change is critical to preparing for the effects of global warming. The Greenland Ice Sheet (GrIS) comprises one of these systems. Beginning in the mid-1990s, the GrIS began losing mass at an accelerated rate [up to 400 Gt yr^{-1}; *Shepherd et al.,* 2012; *Velicogna et al.,* 2014; *van den Broeke et al.*, 2016]. Greenland mass balance is modulated, in equal parts, by two main components: 1) changes in melting and meltwater transport out of the ice sheet system; and 2) changes in dynamic ice discharge from the ice sheet to the ocean. Here I focus on the second. Recent studies estimate dynamic mass loss from tidewater (or ocean-terminating) glaciers accounts for 40% of total observed GrIS mass loss during the recent time period [*van den Broeke et al., 2016*]. Thus, understanding dynamic ice loss from tidewater glaciers is critical to predicting sea level rise contributions from the GrIS over the next century.

Tidewater glaciers are troughs of fast flowing ice that terminate in the ocean where their grounding lines rest up to a kilometer below sea level [*Rignot et al*., 2016a]. Melting at the glacier surface and bed generates water that lubricates the ice/bed interface and facilitates fast flow [*Andrews et al*., 2014], sometimes exceeding 10 m d^{-1} at the terminus [*Joughin et al*., 2011]. Extending hundreds of kilometers into the thick ice sheet interior, tidewater glaciers transport ice from an inland catchment to the terminus where ice is lost to the ocean through calving and melting, collectively referred to as frontal

ablation. The terminus integrates numerous processes impacting frontal ablation. For example, warm ocean waters born from the North Atlantic Current encircle Greenland, advect through deep coastal fjord systems and supply heat to tidewater glacier fronts for melting [*Straneo and Cenedese*, 2015]. Alternatively, sediment loads eroded, bulldozed and flushed from the subglacial system accumulate to form stabilizing morainal banks at the terminus that counteract ice loss [*Brinkerhoff et al*., 2017].

Tidewater glacier terminus positions are determined by competing rates of ice flow and frontal ablation. Terminus retreat occurs when calving and melting exceed ice flow and more ice mass is lost to the ocean. In turn, terminus retreat perturbations trigger a range of feedbacks and transients that further adjust inland glacier dynamics [*Nick et al.*, 2008; *McFadden and Howat*, 2011; *Seale et al*., 2011; *Motyka et al*., 2011]. Terminus retreat reduces back-stresses at the glacier bed and margins restricting driving stresses, which accelerates ice discharge and glacier thinning. Thinning transients propagate up glacier as a diffusive wave, steepening the glacier surface slope and further increasing driving stresses and downstream ice flow. Ultimately, these feedbacks force larger contributions to sea level rise. Despite this importance, projecting terminus behavior at tidewater glaciers remains elusive due to the absence of several critical observational datasets and uncertainty in the climatic and physical processes controlling frontal ablation [*Truffer and Motyka*, 2016]. Indeed, direct observations of tidewater glacier termini are largely obstructed by dangerous, ice-choked fjords and logistical obstacles. To address this shortcoming, my focus in this dissertation is to use a suite of novel in-situ and remotely-sensed observations and supporting models to build a process-oriented

understanding of tidewater glacier terminus morphology, frontal ablation and position. In turn, these factors help regulate dynamic ice loss to the ocean.

1.2. Processes Driving Terminus Position Change

Projecting future terminus positions requires adequate knowledge of processes underlying their behavior, as well as the time and spatial scales on which they change. Tidewater glacier termini dynamically couple ice sheet, ocean, atmosphere and sedimentary systems (Figure 1.1). As a result, processes impacting the terminus are myriad and complex.

Numerous studies show a causal link between several potential forcing mechanisms and tidewater glacier terminus positions that incorporate various parts of the glacier system, including glacier hydrology, oceanography, geometry and sedimentology [*Mercer*, 1961; *Murray et al.*, 2010; *Howat et al.*, 2010; *Joughin et al*., 2012; *Straneo and Heimbach*, 2013; *Carr et al*., 2013; *Moon et al*., 2015; *Luckman et al*., 2015]. Recent evidence has implicated submarine melting at the ice/ocean interface as an important process driving terminus change [*Motyka et al*., 2003; *Jenkins et al*., 2011; *Motyka et al*., 2013; *Straneo and Heimbach*, 2013]. Surface meltwater (often termed runoff) is efficiently transported to the glacier bed where it flows to the terminus as subglacial discharge (Figure 1.1). Discharge released across the grounding line rises buoyantly in the proglacial fjord, turbulently mixing warm, dense Atlantic water that, in turn, drives heat transfer and melting (Figure 1.1) along the glacier front [*Motyka et al*., 2003; *Rignot et al*., 2010; *Motyka et al*., 2013]. In general, increases in subglacial discharge increase

submarine melt by a factor less than 1 [*Jenkins, 2011*; *Xu et al., 2013*]. Submarine melting additionally requires background ocean thermal forcing in the proglacial fjord (Figure 1.1). Evidence connects widespread retreat of Greenlandic tidewater glaciers to warming of the subpolar North Atlantic, due to the superposition of multidecadal natural ocean variability on a long-term warming trend in the North Atlantic's upper ocean heat content [*Straneo and Heimbach*, 2013]. Ultimately, warming of North Atlantic water combined with increases in meltwater runoff and subglacial discharge increased submarine melting at GrIS tidewater glaciers over the last two decades [*Straneo et al*., 2010; *Straneo and Heimbach*, 2013]. In turn, submarine melting can trigger subaerial calving by thermally eroding the submarine terminus face and destabilizing ice above [*O'Leary and Christoffersen*, 2013; *Bartholomaus et al*., 2013; *Chauché et al*., 2014; *Fried et al*., 2015].

Previous studies show that warm, ambient ocean water can drive substantial submarine melt in winter [e.g. *Jackson et al*., 2014], potentially impacting terminus behavior in the absence of buoyancy-driven estuarine exchange flow at the glacier front (*Luckman et al*., 2015). Melting controlled by ocean thermal forcing requires inland advection of deep, salty Atlantic water forced by density variations at the fjord mouth [*Nilsen et al*., 2008; *Straneo et al*., 2010] and local wind-driven flow [*Klinck et al*., 1981]. In turn, these inflows are strongly mediated by proglacial bathymetry and sedimentary features along the seafloor. Relict morainal banks, or sills, impede deep warm water inflows [*Sutherland et al*., 2014] and active moraines at the grounding line potentially limit warm water entrainment. Alternatively, deep bathymetric troughs excavated during

previous glaciations enable efficient shelf-fjord exchange and heat transport to the terminus [*Rignot et al*., 2016a].

Mélange, a dense concentration of icebergs in a sea or landfast ice matrix, can act as a weak, granular ice shelf at the terminus front [Figure 1.1; *Amundson et al.,* 2010; *Walter et al.,* 2012]. Thus, mélange can apply a back-stress on the terminus [*Walter et al.,* 2012; *Cassotto et al.,* 2015], which reduces calving and, in turn, stimulates terminus advance [*Amundson et al.,* 2010; *Walter et al.,* 2012; *Todd and Christoffersen,* 2014; *Cassotto et al.,* 2015]. Field observations show that mélange removal through melting or wind shear can coincide with increased calving [*Cassotto et al.,* 2015], glacier speed up [*Walter et al*., 2012] and terminus retreat [*Moon et al.,* 2015]. Mélange rheology and extent depends on local calving flux and varies between tidewater glacier systems. In contrast to dense mélange at the largest tidewater glaciers (e.g. Jakobshavn Isbrae) that contain 10s of kilometers of 100+ m icebergs [*Cassotto et al.,* 2015], smaller systems may only feature seasonal sea ice and small, sparse icebergs.

Additional processes influence iceberg calving at the terminus. Longitudinal stresses at the terminus create depth penetrating surface crevasses that intersect elevated columns of ice termed seracs. Serac failures produce high-frequency, small-magnitude (1-10's m) calving events at many tidewater glaciers [*Bartholomaus and Basis*, 2014]. Water filling in crevasses can induce failure through hydrofracturing [*Cook et al*., 2012; *Cook et al*., 2014]. Deep terminus systems support basal crevasses created through basal water pressure and buoyant flexure at the terminus [*James et al*., 2014; *Cook et al*., 2014; *Wagner et al*., 2016]. Such conditions cause large magnitude (10-100's m) capsizing slab

calving events [*Bartholomaus and Basis*, 2014]. Opposite these processes, submarine sedimentation can ameliorate calving at the terminus. For example, sediment accumulation decreases water depth above grounding line moraines, which mitigates calving and further stabilizes the glacier front [*Powell*, 1991].

Terminus positions are also sensitive to bed topography, because glacier outlet geometry controls the stress field at the terminus [*Mercer*, 1961; *van der Veen*, 1996; *Pfeffer*, 2007]. In general, tidewater glaciers retreat rapidly through broad, bathymetric overdeepenings that contain retrograde bed slopes [*Meier and Post*, 1987; *McNabb and Hock*, 2014; *Catania et al*., 2018]. In contrast, terminus positions are more stable at topographic pinning points; areas where outlets narrow or become more shallow. Such geometric controls are thought to help explain heterogeneous retreat and retreat rates at neighboring Greenlandic tidewater glaciers [*Catania et al*., 2018] In turn, glacier outlet geometries evolve through sediment accumulation and erosion. Prolonged glacier advance through overdeepend parts of the bed depends on sediment-driven shallowing of the terminus [*Brinkerhoff et al*., 2017].

Finally, glacial meltwater can lubricate the ice/bed interface and increase basal sliding [*Howat et al*., 2010], potentially causing glacier advance. This relationship varies significantly around the ice sheet. For example, ice velocity time series reveal divergent seasonal velocity patterns among Greenlandic tidewater glaciers [*Moon et al*., 2014]. This suggests that, in response to common seasonal meltwater pulses, some glacier catchments transition from inefficient, distributed hydrologic networks (promoting fast flow) to efficient, channelized drainage (promoting slow flow) and others do not [*Moon et al*.,

2014]. On interannual timescales, observed glacier accelerations cannot be explained solely by enhanced bed lubrication [*Joughin et al*., 2008], suggesting terminus perturbations and resulting reductions in resistive stresses are also responsible for glacier speedup [*Nick et al*., 2009].

1.3. Importance and Scope

1.3.1. Study area

My dissertation focuses on a suite of tidewater glaciers along the ~250 km central west coast of the GrIS (Figure 1.2). Here, the Nussuaq Peninsula separates the deep (> 1 km below sea level) Uumannaq and Disko Bay fjords systems, to the north and south, respectively [Rignot et al., 2016]. Fjords are fed by seasonal fluctuations of warm, salty Atlantic Water advected landward from the West Greenland Current below cold, fresh Polar Water [*Holland et al.*, 2008; *Straneo and Cenedese*, 2015]. Tidewater outlet glaciers drain the ice sheet through steep mountain troughs and terminate in the fjord waters (Figure 1.2). Below the glacier equilibrium line, the central west Greenland coast maintains a relatively dry, tundra climate, and several months support mean temperatures high enough to melt snow and glacier ice each year [*Noël et al.*, 2017].

1.3.2. Regional context and advances

Synchronized changes in ice discharge [*Howat et al.*, 2008] and terminus retreat [*Catania et al.*, 2018] at Greenlandic tidewater glaciers, despite being located several hundred kilometers apart, suggests sensitivity to environmental (atmospheric or ocean) forcing [*Luckman et al.*, 2006; *Murray et al.*, 2010; *Catania et al.*, 2018]. Indeed,

terminus positions at the majority of glaciers in the region of interest initiated retreat in the late 1990's, coincident with increased atmospheric and ocean warming [*Holland et al*., 2008; *Catania et al*., 2018]. However, within this regional pattern lies significant local variability [*Joughin et al*., 2010; *Howat et al*., 2011; *Bartholomaus et al*., 2016; *Felikson et al*., 2017]. In some cases, glaciers directly adjacent to one another in central west Greenland exhibit markedly different changes in flow speed [*Joughin et al*., 2010], dynamic thinning [*Felikson et al*., 2017] and terminus position [*Catania et al*., 2018]. For example, since the 1990's, some glaciers in this region underwent rapid terminus retreat (e.g. Umiammakku Sermiat and Sermeq Silarleq), while other glacier termini were stable (e.g. Rink Isbrae and Store Gletsjer). This suggests 2nd-order processes (i.e., not regional climate) mediate how external forcing manifests glacier change. These processes include small differences in glacier boundary conditions, such as unique outlet geometries, ice fluxes and catchment sizes. For example, *Bartholomaus et al.* [2016] found that individual glacier and fjord geometries modulate subglacial discharge, which leads to contrasts in both fjord and glacier dynamics for three adjacent tidewater glaciers in the study area. As a result, reproducing terminus retreat records due to external forcing in ice sheet models remains elusive because the underlying processes driving differences in glacier behavior are not well represented. Precise predictions of terminus positions require a processes-based understanding of these tidewater glacier systems that combine insights from coincident ice-ocean-atmosphere observations. Recent advances in this area have been achieved through the interpretation and integration of new geophysical datasets that constrain boundary conditions at the terminus, including bed topography

[*Morlighem et al.*, 2017], proglacial fjord bathymetry [*Rignot et al.*, 2016], oceanography [*Holland et al., 2008*; *Carroll et al.*, 2016], surface mass balance [*Noël et al.*, 2017] and multibeam sonar imaging of the submarine terminus face [*Rignot et al.*, 2015; *Fried et al.*, 2015].

In order to quantify controls on spatiotemporal terminus position variability, I contributed to a rich database of digitized terminus positions for tidewater glaciers in the region of interest (Fig. 3). The database makes use of several high-resolution remotely sensed datasets, including Landsat (Level 1T, 30-m resolution), Advanced Spaceborne Thermal Emissivity and Reflection Radiometer (ASTER, 15-m resolution) and TerraSAR-X imagery (courtesy of the German Aerospace Center, DLR, 20-m resolution). The database provides near bi-weekly temporal coverage since 2000. To interpret terminus position records, I used several in-situ and remotely-sensed geophysical datasets, including images of submarine terminus face morphologies from multibeam echo sonar, ocean temperatures from moorings deployed in the proglacial fjord (*Bartholomaus et al*., 2016), ice velocity fields from optical [*Fahnestock et al.*, 2015; *Roseneau et al.*, 2015; *Scambos et al.*, 2016; *Howat et al.*, 2017] and radar [*Joughin et al.*, 2010; *Joughin et al*., 2011] imagery, glacial runoff and subglacial discharge from regional climate models [*Noël et al.*, 2017], air temperatures from on-ice meteorological stations, and observations of turbid subglacial plumes and mélange conditions from satellite imagery and time lapse photography. More detailed explanations of how I apply these datasets are given in the subsequent chapters. Together, these observations enable a process-oriented approach to better understand terminus

morphology and positions across the diversity of tidewater glaciers within the study area (Figure 1.2). In turn, I expect insights gained from this study in central west Greenland apply to similarly diverse tidewater glacier systems around the GrIS.

1.4. Chapter Structure

Chapter 1 introduces key processes underlying tidewater glacier terminus dynamics and describes the many mechanisms impacting terminus position change (e.g. Figure 1.1). In addition, I outline the motivation and geographic extent of the study (Figure 1.2), as well as the suite of geophysical datasets that I employ to form a process-oriented understanding of terminus morphology and position change in the subsequent chapters. Chapters 2-4 have been prepared or submitted for journal publication.

In chapter 2, I use complimentary datasets of submarine bathymetry, terminus position, sediment plume location and a predictive model of subglacial water routing to present a complete view of the ice/ocean interface and near-terminus hydrology at Kangerlussuup Sermia, a tidewater glacier in central west Greenland (Figure 1.2). I then use multibeam echo sonar to estimate submarine melt rates at each point along the terminus face. My findings suggest that submarine melting at the terminus is more complex than previously appreciated [e.g. *Rignot et al*., 2015]. While some of our observations support the previous prevailing understanding, I find that significant melt occurs in numerous, secondary discharge outlets outside of the main subglacial channel network. As a result, secondary outlets disperse focused undercutting and melting across the glacier front, a pattern that strongly controls the magnitude of ice flux lost to

submarine melting. This work provides much-needed observational constraints on the geometry and magnitude of melt in buoyant subglacial plumes [e.g. *Slater et al*., 2015]. Ultimately, these results directly address uncertainties in prognostic models of the GrIS, because melt and calving triggered from melt-driven undercutting are primary controls on terminus positions and, in turn, dynamic ice sheet mass loss [*Csatho et al*., 2014].

In chapter 3, I present a comparative study to quantify and attribute seasonal terminus position changes to different forcing mechanisms, such as glacial runoff, mélange, and ocean thermal forcing in the proglacial fjord, and in contrasting tidewater glacier systems. I use in-situ and remote sensing datasets to show the impact of environmental forcings on terminus positions largely depends on glacier calving style and flux set by terminus geometry. Terminus positions at relatively shallow, serac failure calving glaciers vary strongly with runoff production, rather than mélange or ocean temperature. At these glaciers, the impact of subglacial plumes is more significant than previously recognized, whereas ocean thermal forcing plays a secondary role. In contrast, the few glaciers with the largest ice discharges to the ocean dominated by large-magnitude, sporadic, full-thickness calving feature terminus positions less sensitive to runoff variations.

In chapter 4, I use the multibeam echo sonar survey collected at Kangerlussuup Sermia to characterize previously unrecognized submarine terminus face morphologies that enable exploration of a range of frontal ablation processes at the glacier front. I identify several characteristic morphologies that populate different terminus regions. Calving primarily overcuts the terminus, while submarine melting forms undercut

cavities at depth. The majority of the terminus is undulating and undercut, while large calving surfaces are sporadic and infrequent. In turn, I pair observations of the terminus with a plume model [*Jenkins*, 2011] and find that small subglacial discharge fluxes reminiscent of a distributed subglacial network produce buoyant plumes that match observed subglacial plume outlet morphologies. While these small discharges disperse melting and undercutting across the glacier front, they do not drive calving rates commensurate with the main subglacial plume at the terminus center. Given observed outlet geometries, unrealistically large discharge fluxes are required to produce plumes that break through the strong shallow fjord stratification and rise to the fjord surface. As a result, maximum plume heights and terminus undercutting are predominantly confined below the fjord pycnocline.

Chapter 5 summarizes key conclusions from chapters 2-4 and contextualizes their insights within the larger framework of the dissertation. In addition, I consider future research efforts that would advance and better constrain the topics investigated in this study.

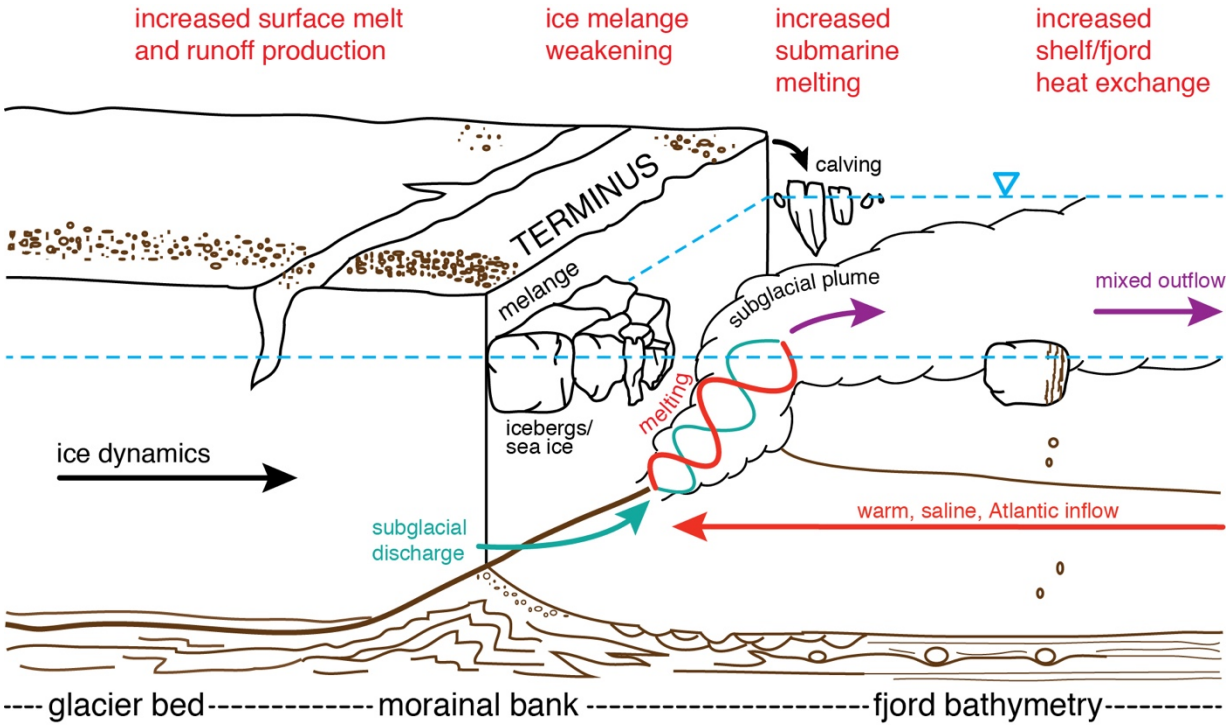

Figure 1.1. Overview of a tidewater glacier terminus system, including buoyancy-driven estuarine exchange flow in the proglacial fjord and related submarine melting at the ice/ocean interface. Overview of potential mechanisms impacting terminus retreat are annotated in red above the schematic.

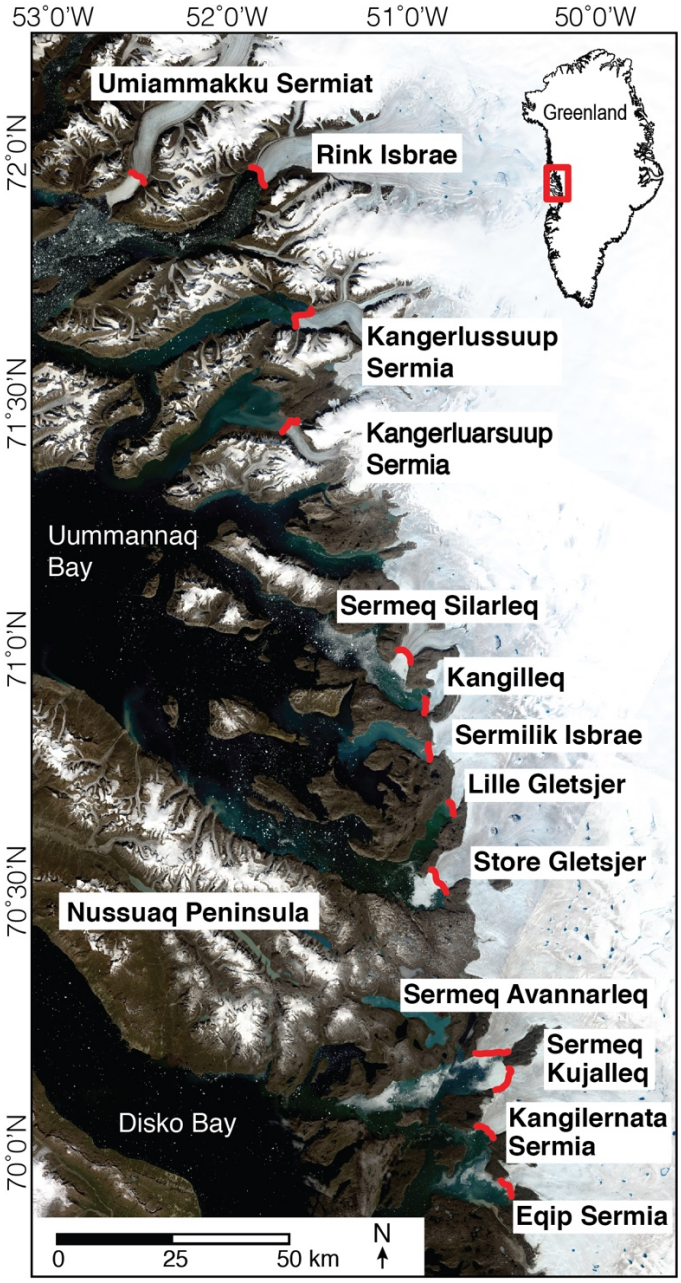

Figure 1.2. Tidewater glaciers in the central west Greenland study area. Glaciers in the region of interest include, from north to south: Umiammakku Sermiat (UMI), Rink Isbrae (RNK), Kangerlussuup Sermia (KAS), Kangerluarsuup Sermia (KSS), Sermeq Silarleq (SIL), Kangilleq (KAN), Sermilik Isbrae (LIK), Lille Gletsjer (LIL), Store Gletsjer (STR), Sermeq Avannarleq (AVA), Sermeq Kujalleq (KUJ), Kangilernata Sermia (KAN), Eqip Sermia (EQP). Glacier fjords connect to Uummannaq and Disko Bays, which are separated by the Nussuaq Peninsula.

Chapter 2. Distributed subglacial discharge drives significant submarine melt at a Greenland tidewater glacier

This chapter was previously published in *Geophysical Research Letters*[1].

2.1. Abstract

Submarine melt can account for substantial mass loss at tidewater glacier termini. However, the processes controlling submarine melt are poorly understood due to limited observations of submarine termini. Here, at a tidewater glacier in central West Greenland, we identify subglacial discharge outlets and infer submarine melt across the terminus using direct observations of the submarine terminus face. We find extensive melting associated with small discharge outlets. While the majority of discharge is routed to a single, large channel, outlets not fed by large tributaries drive submarine melt rates in excess of 3.0 m d^{-1} and account for 85% of total estimated melt across the terminus. Nearly the entire terminus is undercut, which may intersect surface crevasses and promote calving. Severe undercutting constricts buoyant outflow plumes and may amplify melt. The observed morphology and melt distribution motivate more realistic treatments of terminus shape and subglacial discharge in submarine melt models.

[1] Fried, M. J., G. A. Catania, T. C. Bartholomaus, D. Duncan, M. Davis, L. A. Stearns, J. Nash, E. Shroyer, and D. Sutherland (2015), Distributed subglacial discharge drives significant submarine melt at a Greenland tidewater glacier, *Geophys. Res. Lett.*, *42*(21), 9328–9336. M. F. analyzed the data, performed the research and wrote the manuscript.

2.2. Introduction

The Greenland Ice Sheet lost mass at an increasing rate during the last decade, in part due to the increase in ice loss from the fronts of large marine-terminating outlet glaciers [*van den Broeke et al*., 2009; *Rignot et al*., 2011; *Shepherd et al*. 2012; *Enderlin et al*., 2014]. A change in the ocean's forcing at the ice/ocean boundary is a leading hypothesis to explain these increased mass losses [*Murray et al.*, 2010; *Rignot et al*., 2010; *Straneo et al*., 2011]. At the terminus, subglacial discharge plays an important role in controlling ice loss to the ocean by driving submarine melt and promoting calving [*O'Leary and Christoffersen*, 2011; *Straneo et al*., 2011; *Bartholomaus et al*., 2013; *Motyka et al*., 2013; *Inall et al*., 2014; *Rignot et al*., 2015]. These processes can result in rapid outlet glacier dynamic changes through reduction of along-flow gradients in resistive stresses, affecting fast ice flow and, in turn, terminus retreat [*Nick et al*., 2009; *Seale et al*., 2011].

Despite its importance, several factors limit our understanding of how subglacial discharge influences submarine melt and calving. First, thick glacier ice and iceberg-choked fjords generally obscure meltwater routing to and discharge across the terminus. While it is hypothesized that the discharge of subglacial water into the proglacial fjord at discrete points influences submarine melt rates [*Jenkins*, 2011; *Slater et al*., 2015; *Straneo et al*., 2015], few observations of the size, number and locations of channels exist. The extent to which more abundant, secondary channel outlets influence melt at the terminus remains unexplored despite the large rates of submarine melt they can potentially drive [*Slater et al*, 2015]. Second, the morphology of the submarine terminus

face is largely unknown [with the exception of *Rignot et al*., 2015]. The shape of the terminus face may affect the formation of buoyant melt plumes, their ability to melt the glacier front, and calving [*Jenkins*, 2011; *Xu et al*., 2012; *Xu et al*., 2013; Kimura et al., 2014]. Finally, previous submarine melt rate estimates – those derived from both heat and salt budgets [*Rignot et al*., 2010; *Motyka et al*., 2013] and mass continuity [*Motyka et al*., 2011] – are unable to elucidate how the magnitude of submarine melt varies spatially across the terminus and in relation to the location of subglacial channels. In this paper, we work to resolve these issues and identify the impact that distributed subglacial discharge has on submarine melt.

We pair observations from multibeam bathymetry and satellite imagery with a predictive model of subglacial water routing to identify subglacial discharge outlets and their influence on the morphology of the terminus face at Kangerlussuup Sermia (KS), a tidewater glacier in central West Greenland (71°27'N, 51°20'W; Figure 2.1). We then use the observed terminus face morphology to estimate submarine melt rates at each point along the glacier terminus. Finally, we provide further support for a mechanism by which observed melt-driven undercutting facilitates calving via connections to closely-spaced surface crevasses [*Motyka et al*., 2003].

2.3. Data and Methods

2.3.1. Multibeam bathymetry

To investigate how subglacial discharge affects the shape of the glacier terminus, we surveyed the submarine portion of the KS terminus using a Multibeam Sonar System

(Figure 2.2). Multibeam bathymetry data were collected on 21 and 23 July 2013 using a pole-mounted RESON SeaBat 7111 Multibeam Sonar System. Positioning data were acquired using an Applanix POS/MV model 320 positioning and orientation system. The survey operated at 100kHz with 301 equi-angle beams and we constrained the sound velocity profile at the time of the survey using in-situ CTD casts. We collected data along the submarine calving face by inserting a 15° wedge into the Multibeam Sonar System mount to maximize vertical imaging. The resulting point cloud data represent individual measurements of the terminus location and were processed using Caris software to remove anomalous pings and to merge multibeam returns with positioning and orientation data.

In order to quantify the shape of the submarine terminus face across the entire width of the glacier, we extracted 193 terminus cross-sections (spaced every ~27 m) through the multibeam point cloud, each oriented locally normal to the terminus face. For each cross-section we identified the seafloor depth, d, at the grounding line and the height, h, of the seaward-most point on the terminus face above the seafloor (Figure 2.3b). We also define the undercut length, l, as the horizontal distance between the seaward-most point and the grounding line at each cross-section (Figure 2.3b).

2.3.2. Submarine melt estimates

We estimate the submarine melt rate by assuming that any overhang of the submarine glacier terminus is due to melt, since calving from the bottom of the terminus is unlikely to occur without disrupting the ice above it and internal ice deformation is minimal compared to sliding for fast flowing, thin, gently-sloping glaciers [*Cuffey and*

Paterson, 2010]. These assumptions are supported both by the smooth appearance of imaged overhangs (mass lost due to calving would likely produce corners and sharp edges) and the prevalence of sub-vertical surface crevasses throughout the terminus region (calving is most likely to occur along these pre-existing crevasses, and not at the ~45° angles commonly found for overhang roofs). Thus, we use the size of the overhang cavity to estimate the depth-averaged submarine melt rate. We assume that the mid-summer face we imaged was in dynamic equilibrium, that is, while individual cross-sections may change shape due to stochastic calving events, the overall amount of undercutting, averaged over the entire width of terminus, is steady. Satellite observations of glacier speed and terminus position (Figure 2.3a) and RACMO2.3 runoff estimates (*Ettema et al*., 2009) immediately prior to and during our survey do not suggest any significant changes in glacier dynamics that might violate this assumption. Thus, the terminus face within the overhang (over height *h*) melts at the rate $\dot{m}_h = \vec{u} \cdot \hat{n} - dL/dt$, where $\vec{u} \cdot \hat{n}$ is the ice velocity normal to the terminus and dL/dt is the rate of change of the glacier terminus position. Following convention, $\dot{m}_h$ is defined positive up-glacier, whereas $\vec{u} \cdot \hat{n}$ and dL/dt are positive towards the fjord. We obtain ice velocities from 16 July – 27 July 2013 TerraSAR-X data [*Joughin et al*., 2014] and use the associated TerraSAR-X imagery to identify *dL/dt* during the time of our multibeam survey. While the overall terminus position did not change significantly over the observation period, large *dL/dt* values caused by localized calving events represent a source of local noise that obscures the patterns we seek to reveal. Thus, we calculate the mean *dL/dt* (0.30 m d^{-1}) from the distribution of observed length changes and use this value at each cross-

section in our melt estimates. The depth-averaged melt rate at a given cross-section through the submarine terminus is thus $\dot{m} = h(\vec{u} \cdot \hat{n} - dL/dt)/d$. Our calculation does not consider ice loss above the seaward-most point, which may occur through either melt or calving; in this regard our melt rates are conservative. The flux of ice lost due to submarine melt, Q_i, is calculated as, $Q_i = \overline{m}A_w$, where $\overline{m}$ is the terminus-averaged submarine melt rate and A_w is the vertical, submerged terminus area.

Uncertainty in our calculation of the depth-averaged submarine melt rate is related to the uncertainties in both the ice velocity and multibeam datasets and our consideration of *dL/dt*. Measured ice velocities have a mean error of 0.08 m d^{-1} [*Joughin et al*., 2014]. The multibeam point cloud is accurate to within 3-5 m horizontally and 15-25 cm radially from the ship, as reported by the POS/MV and RESON systems, respectively. We assume a digitizing error of <10 m when extracting cross-sections and include a 1-σ error associated with the mean *dL/dt* of 1.5 m d^{-1}. Propagation in quadrature of these uncertainty contributions gives an uncertainty of ±1.5 m d^{-1} in our melt rate estimates. We present further support for our assumptions as supporting information.

2.3.3. Subglacial hydrology

We constrain the geometry of the near-terminus subglacial hydrologic system using two lines of evidence. First, we identify sediment plumes emerging at the terminus of the glacier from 63 Landsat-7, Landsat-8 (30 m horizontal resolution) and Advanced Spaceborne Thermal Emissivity and Reflection Radiometer (ASTER; 15 m horizontal resolution) images between 2008-2013, with an average time interval between images of ~1.5 weeks during the summer. We manually digitize sediment plume boundaries and

interpret the glacier terminus/sediment plume interface as the location where subglacial meltwater actively outflows from a subglacial channel (Figure 2.4b).

Second, we determine the likely locations of subglacial channels by calculating the gradient in the hydraulic potential (Φ) [*Shreve*, 1972];

$$\nabla\Phi = \nabla(\rho_i g(Z_s - Z_b) + \rho_w g Z_b)$$

where ρ_i and ρ_w are the densities of ice and fresh water, Z_s and Z_b are the ice surface [*Howat et al*., 2014] and bed elevation [*Morlighem et al*. 2014], and g is the acceleration due to gravity. We present uncertainty in the location of modeled subglacial flowpaths by adding white noise scaled to the reported uncertainty of the input datasets at each grid point and recalculate the hydraulic potential gradient for 100 calculations (Figures 2.1 and 2.4b).

2.3.4. Surface crevasses

In order to evaluate the ability of terminus undercutting to vertically connect with surface crevasses, we compare the spacing of adjacent surface crevasses to the length of undercutting beneath them. Surface crevasses near the KS terminus are identified along a longitudinal profile striking up-glacier using a WorldView-2 satellite image (0.5 m horizontal resolution) from 13 July 2012 (A-A' in Figure 2.3). We measure distances between observed crevasses near the terminus and quantify their mean spacing (Figure 2.3b). We then sample the ice surface elevation along the longitudinal profile to get the elevation of observed crevasses using a SETSM DEM tile derived from the same WorldView-2 image [*Noh and Howat*, 2015] (Figure 2.3a).

2.4. Results

KS terminates in water up to 275 m deep atop a broad morainal bank; the glacier fjord is 5-km wide at the ice front (Figures 2.1 and 2.2). At the center of the KS terminus is a region, which we term the "prow," which extends into the fjord and divides the terminus into northern and southern portions (Figure 2.1). Satellite imagery reveals the seasonal evolution of the glacier terminus; between May and September 2013, the largest terminus retreat (~500 m) occurred at the prow, with <50 m retreat elsewhere (Figure 2.3a).

The subglacial hydraulic potential reveals two well-defined subglacial channel flowpaths within 10 km of the KS terminus that sit beneath surface elevation troughs ~70 m lower than their adjacent across-flow high points (Figures 2.1 and 2.4b). Closer to the terminus, the majority of meltwater coalesces into a single subglacial channel (channel 1 in Figures 2.1 and 2.4b) that discharges at the terminus prow (Figure 2.1). A second channel (channel 2) may – within the hydropotential uncertainty – discharge across the northern terminus face (Figures 2.1 and 2.4b). Along the southern terminus face the hydropotential results suggest that melt water is drawn from a small region close to the terminus that is not part of the main upstream-channelized system; i.e., no large subglacial discharge flow paths are mapped in this vicinity (Figures 2.1 and 2.4b).

Sediment plumes identified in satellite imagery at the fjord surface are consistent with the geometry of the modeled near-terminus subglacial hydraulic gradient and associated subglacial flowpaths. Approximately 95% of sediment plumes observed between 2008-2013 occur at the terminus prow (Figure 2.4b). The persistent occurrence

of sediment plumes at the terminus prow verifies that the large subglacial channel discharging there is a stable feature within the subglacial hydraulic gradient over multiple years. The remaining sediment plumes occur along the northern portion of the terminus, adjacent to smaller, secondary channels identified within the hydropotential uncertainty (Figure 2.4b). We do not observe plumes along the southern terminus face, where we also do not expect major subglacial discharge flow paths.

Side-looking multibeam bathymetry reveals lateral and vertical heterogeneity in the submarine terminus face morphology (Figures 2.2, 2.3b and 2.4a). We find that roughly 80% of the submarine terminus face is undercut with a mean undercut length across the entire terminus of 45 m (Figure 4a). Buoyancy forces do not increase either h or l because the terminus is well-grounded, with the ice surface elevation > 10 m above flotation almost everywhere within the terminus region (Figure 2.5). The largest undercut feature in our survey is found at the terminus prow (h ~150 m and 220 m wide) (outlet #5 in Figures 2.2, 2.4 and 2.6). This laterally constricted submarine tunnel has an arched roof rising to within 50 m of sea level and a back that was not imaged by our multibeam system (l > 200 m). It coincides with the outlet of the predicted subglacial channel at the terminus prow (channel #1) and the most common location for sediment plume formation (Figure 2.4b). Based on this evidence, we interpret the observed submarine tunnel mouth as the discharge outlet for the main subglacial channel (channel #1).

The multibeam bathymetry also reveals significant terminus face complexity outside of the main discharge outlet at the terminus prow. We identify six vaulted and laterally constricted submarine cavities in the terminus face (outlets #1-4 and #6-7) that

are smaller than the tunnel mouth (with *l* and *h* both greater than 150 m, Figure 2.2 and 2.4a). These cavities are unassociated with sediment plumes observed at the fjord surface. While the outlet at the main subglacial channel appears as an open tunnel within the terminus face, these cavities share a relatively smooth, sloping cavity roof that dips up-glacier (Figure 2.3b). The angle between a vertical line and the cavity roofs within these large cavities is consistently between 40–47 degrees (Figure 2.3b). Based on their unique morphology, that is, severely undercut with sloping cavity roofs over a narrow width of the terminus (~50 m), we interpret these features as additional outlets for concentrated subglacial discharge, which we term secondary discharge outlets. Outside of these outlets, the submarine terminus face is more gently and moderately undercut or, in rare cases, overcut (Figure 2.4a).

We find four large discharge outlets along the southern terminus face (outlets #1-4 in Figure 2.4) that appear outside of the modeled subglacial channel system. Here, the outlets are spaced approximately 200 m apart and the largest cavity, outlet #4, is similar in size to the tunnel mouth at the terminus prow (*h* ~150 m, *l* ~220 m and ~150 m wide; Figure 2.2). We also see evidence in the multibeam bathymetry for two zones of deltaic sediment deposition (outwash fans) from subglacial discharge, which rise up to 30 m above the morainal bank immediately seaward of discharge outlets #3 and #4 (Figure 2.4a). This deposition occurs despite no evidence of sediment plumes at the fjord surface or subglacial channels in the hydropotential gradient there. The outwash fan deposits have sediment volumes of ~7.2×10^5 m^3 and 5.0×10^5 m^3 above the surrounding morainal bank crest, respectively, representing the sediment load deposited from the adjacent

discharge outlets. Our observations suggest that these outlets draw water from a small subglacial catchment close to the terminus.

Computed depth-averaged melt rate estimates are heterogeneous across the terminus with the largest melt rates located at the seven submarine discharge outlets, ranging from 2.3 – 3.7 m d^{-1} (Figure 2.4b). These seven discharge outlets account for 45% of the total submarine melt across the glacier terminus with an average of 1.6 m d^{-1} melt outside of the discharge outlets. The main subglacial channel outlet at the terminus prow (outlet #5) drives approximately 12% of the total estimated submarine melt across the terminus. This indicates that when combined, secondary discharge outlets drive the majority of melt despite drawing discharge from outside the main subglacial channel system (Figure 2.4b). As a result, the observed discharge outlet configuration disperses melt across the terminus face rather than focusing melt at one centralized location near the terminus prow [cf. *Xu et al*., 2013]. Across the entire terminus, the melt rate averages 2.0 m d^{-1}; the total flux of ice lost due to submarine melt is 0.0018±0.0011 km^3 d^{-1}, 36±20% of the total, full-thickness ice flux delivered to the KS terminus.

WorldView-2 satellite images show that the near-terminus glacier surface is heavily crevassed. The mean distance between adjacent surface crevasses is 80 m directly above discharge outlet #4, a spacing that enables at least two crevasses above the section of the terminus undercut there by ~200 m (Figure 2.3). Satellite imagery confirms that the distance between adjacent surface crevasses here is representative of crevasse spacing across the entire terminus.

2.5. Discussion

While the magnitude of the calculated submarine melt rate at KS is similar to that determined elsewhere for similarly-sized Greenlandic tidewater glaciers [*Rignot et al*. 2010], we find heretofore unidentified heterogeneity in melt rates, largely driven by the presence of seven identified discharge outlets distributed across the terminus. While the largest discharge outlet at the terminus prow is associated with predicted subglacial flowpaths, persistent sediment plumes and anticipated large submarine melt [*Xu et al*., 2013; *Kimura et al*., 2014], we also demonstrate that the near-terminus, distributed hydrologic system drives significant submarine melt through minor discharge outlets elsewhere. We observe melt rates exceeding 3.0 m d^{-1} at smaller, secondary discharge outlets outside of the main subglacial channel system, particularly along the southern terminus face. We expect relatively small subglacial discharge fluxes here compared to the main subglacial channel since these locations are unassociated with sediment plumes or predicted subglacial discharge flow paths. The lack of sediment plumes observed at the fjord surface does not necessarily discount subglacial discharge entirely. However, fluxes from these outlets must be small or they would appear at the surface of the shallow, 275 m-deep KS fjord [*Carroll et al*., 2015]. Our observations highlight the importance of considering smaller discharge outlets within a more distributed system when modeling terminus-averaged submarine melt rates.

Our results show the morphological complexity of the submarine terminus and provide observational support for long-standing assumptions of terminus undercutting due to submarine melt [*Motyka et al*., 2003]. We find significant undercutting across the

terminus face, due in large part to distributed subglacial discharge through secondary discharge outlets. This complexity has several important consequences. First, undercutting of the terminus face through melting can trigger calving [*O'Leary and Christoffersen*, 2011; *Bartholomaus et al*., 2013; *Chauché et al*., 2014]. The dominant mode of calving at KS is through serac failure, likely by mechanical failure of the ice column from upward melting of undercut cavity roofs eventually connecting to finely-spaced surface crevasses (Figure 2.3b). Indeed, we see in both field observations and satellite imagery that the along-flow width of icebergs calving near the heads of discharge outlets along the southern terminus face often matches the spacing between adjacent surface crevasses there (~80 m), most likely isolated by undercutting following extensional crevassing. We also find greater rates of calving at the subglacial channel near the terminus prow, where melting is largest. Here, satellite images often show the formation of a laterally constricted calving embayment at the location of the subglacial channel outlet below (Figure 2.1 and 2.3a). Similar crenulated terminus geometries have been linked to submarine melt from channelized runoff at other tidewater glaciers [*Sikonia and Post*, 1980; *Bartholomaus et al*., 2013; *Chauché et al*., 2014].

Existing models of submarine melt and near-terminus water circulation assume vertical, planar tidewater glacier termini [*Jenkins, 2011*; *Xu*, 2012, 2013; *Sciascia et al*., 2013; *Carroll et al*., 2015; *Slater et al*., 2015]. Our observations emphasize the need to account for the full 3-D context at the ice/ocean interface when considering buoyant outflow plume dynamics. We expect that buoyant outflow plumes are constricted both by the overhanging roof and the lateral walls within the observed discharge outlets. A

small discharge flux released at an undercut, sloping (~45°) interface might produce a plume that has more time to entrain ambient water, thus achieving neutral buoyancy at a lower depth than if the terminus were vertical. Such feedbacks would explain how relatively small discharge fluxes from secondary outlets can drive melt rates nearly as high as are found at the main subglacial channel. Current models suggest undercutting could reduce plume entrainment by forcing non-vertical upwelling (*Jenkins*, 2011), or by restricting plume/fjord water contact. We argue that the discrepancy between these models and our results must be rectified.

2.6. Conclusion

Discharge-driven submarine melt provides a dynamic coupling between glacier and ocean systems. Our results present much-needed constraints on the geometry of subglacial discharge outlets, the shape of the submarine terminus face and the impact that these variables have on the spatial distribution of melt across the terminus. We find that distributed discharge outside of dominant channels can induce significant melt at locations not identified using hydraulic potential analyses alone [e.g. *Rignot et al*., 2015]. While concentrated subglacial discharge can play an essential role in fjord circulation [*Motyka et al*., 2013; *Carroll et al*., 2015; *Straneo and Cenedese*, 2015], subglacial water dispersed over the width of the submarine terminus through smaller discharge outlets can also control the rate and distribution of submarine melt. The combination of ice/ocean interface observations with ice surface and bed elevation datasets has revealed new insights into the geometric and mechanical relationship between undercutting and

calving. We suggest terminus undercutting can destabilize the ice front by connecting to surface crevasses. To better represent the ice-ocean boundary in prognostic models of the Greenland Ice Sheet, numerical models may need to account for the three-dimensional complexity of the submarine terminus face and assess the importance of rapid melt at more abundant, small-discharge outlets.

2.7. Acknowledgements

This work was completed at the University of Texas at Austin and funded by NASA grant NNX12AP50G and a seed grant from the Jackson School of Geosciences, University of Texas at Austin. We thank Alun Hubbard, an anonymous reviewer and the editor for helpful comments that greatly improved the manuscript.

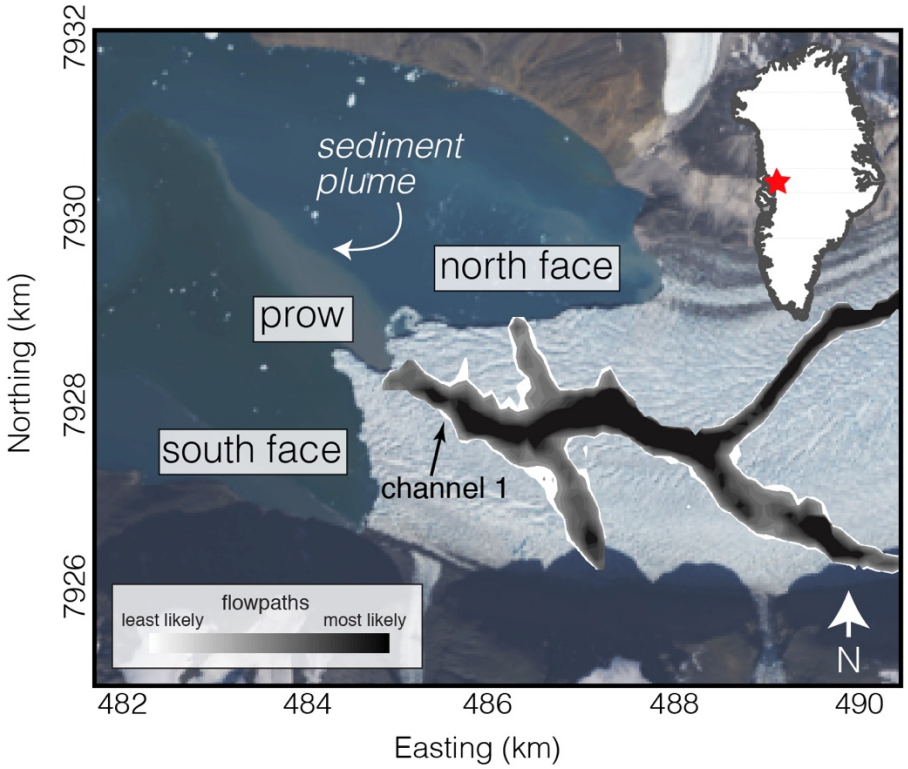

Figure 2.1. KS study area. Landsat 8 image (14 July 2014) showing the KS terminus region. Modelled subglacial water flowpath likelihoods are shown in gray-scale.

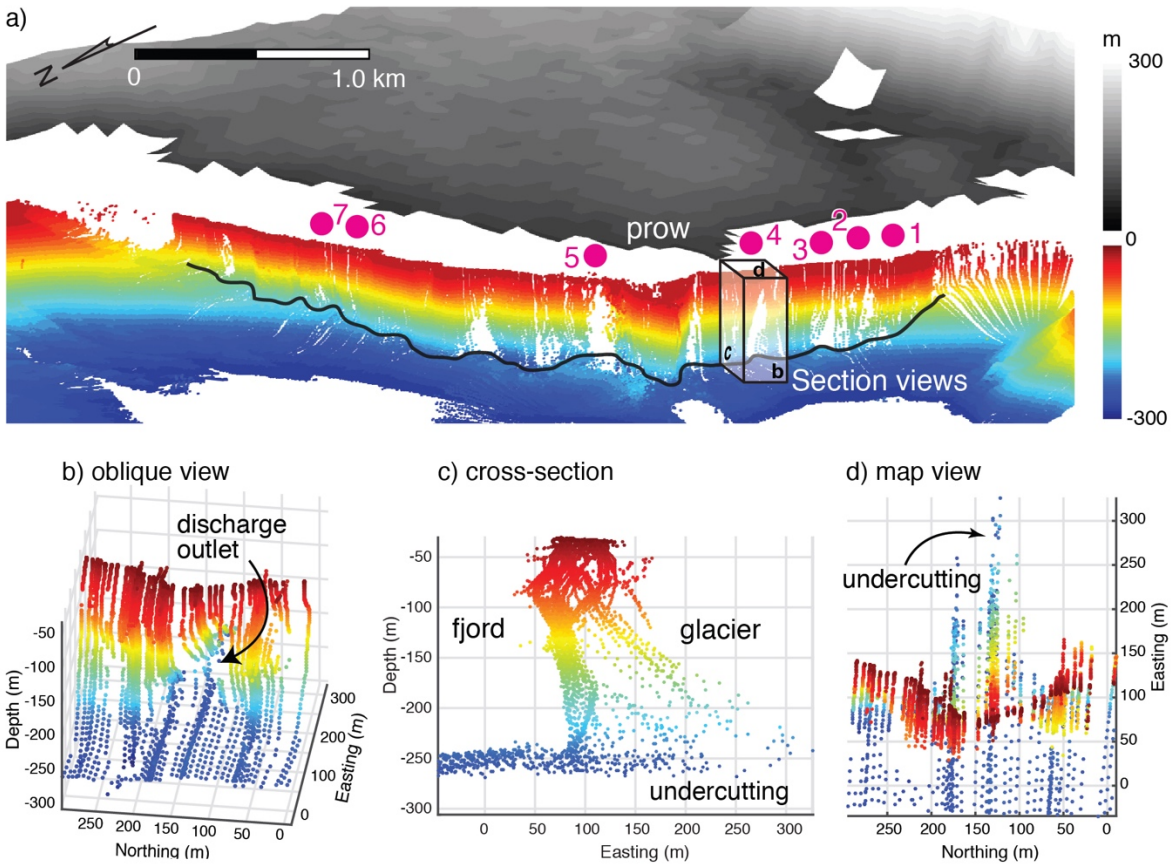

Figure 2.2 Perspective view of the KS ice/ocean interface and near-terminus hydrology. Glacier terminus shown with GIMP topography (gray-scale) and multibeam bathymetry (jet color-scale). Grounding line identified from multibeam bathymetry is shown in black. Pink dots 1-7 refer to identified subglacial discharge outlet locations. Section views (b-d) show close-ups of the multibeam point cloud illuminating localized undercutting at discharge outlet #4 from three different angles.

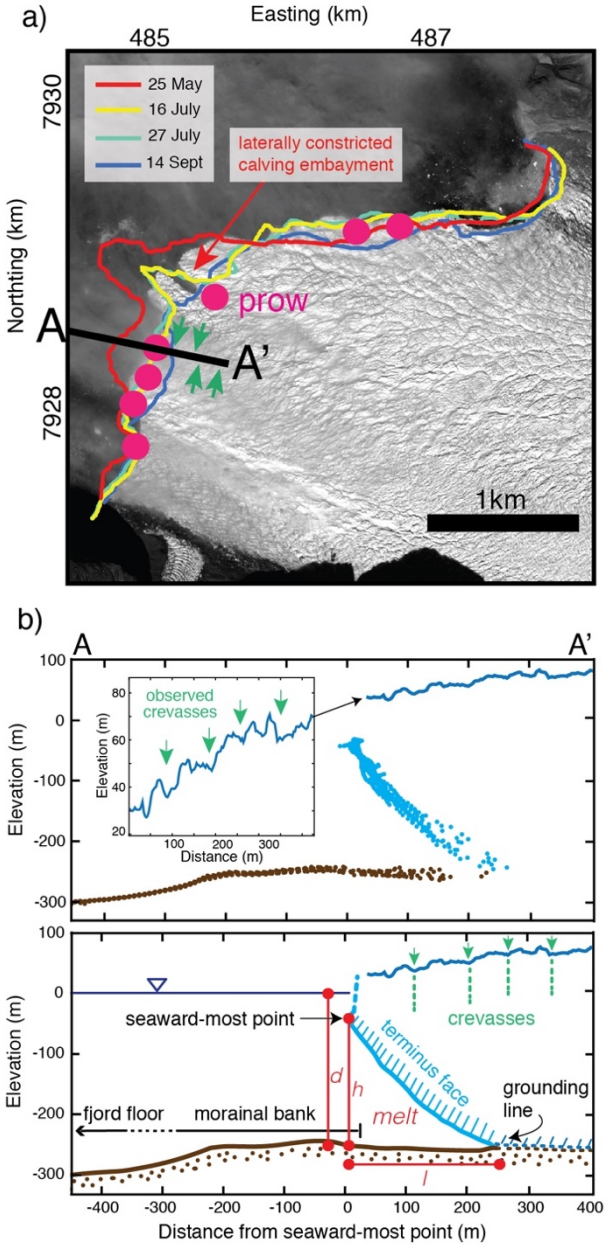

Figure 2.3. Terminus position and morphology. (a) WorldView-2 imagery (13 July 2012, © DigitalGlobe, 2012) with summer 2013 terminus positions (© DLR, 2013). Pink dots are channel outlets and green arrows are locations of surface crevasses along transect A-A'. Transect (A-A') marks the location of the multi-beam point cloud shown in (b). (b) Top panel shows raw multibeam data: bathymetry (brown) and submarine calving face (light blue). Glacier surface (dark blue) is from 2m-resolution SETSM DEM, derived from the image in (a). Inset shows vertically exaggerated glacier surface and crevasse locations. Bottom panel shows labeled schematic of top panel.

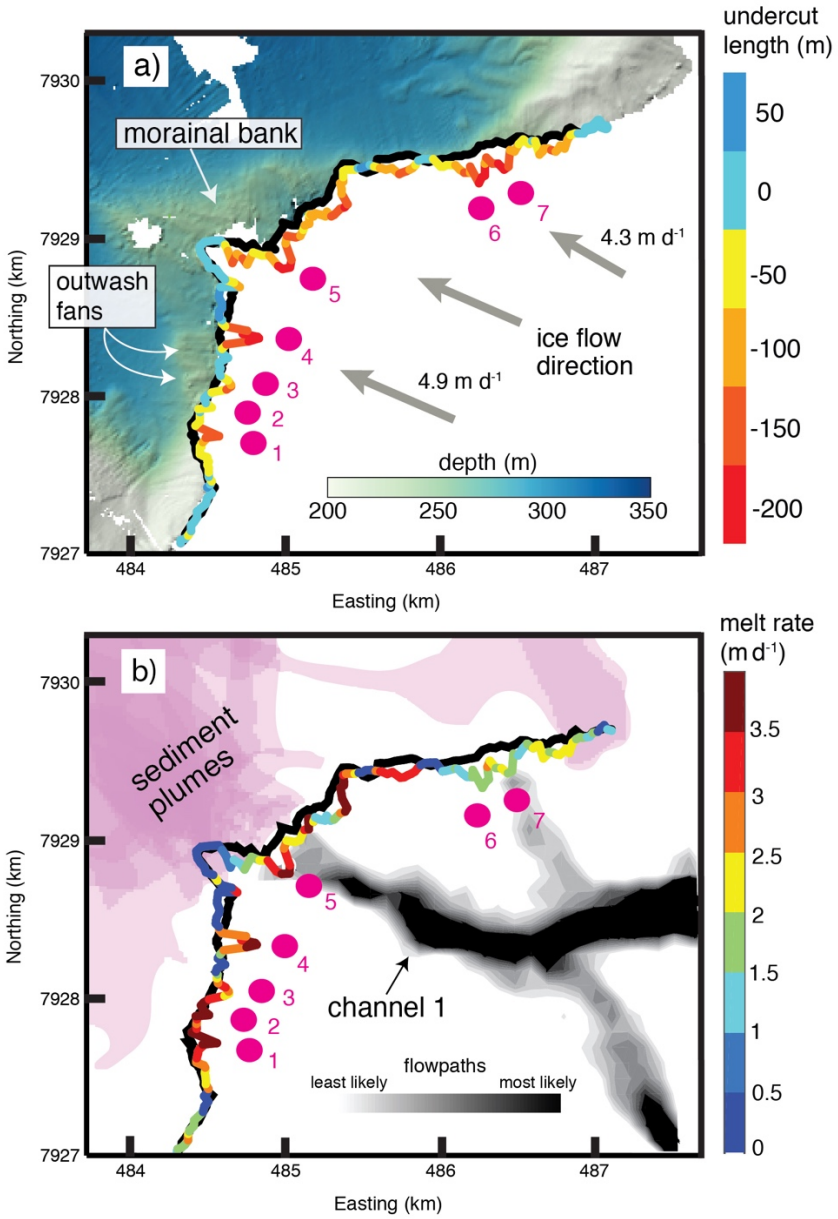

Figure 2.4. Terminus undercutting and submarine melt rates. Map view of KS near-terminus region and pro-glacial bathymetry. Pink dots show locations of subglacial discharge outlets. Black line at terminus represents top-most (closest to tidewater line, approximating glacier terminus) multibeam returns. Colored line marks the position of the grounding line constrained from multibeam data (refer to Fig. 3b) with colorscale representing a) the terminus overhang length and b) the estimated submarine melt rate for each terminus-normal cross section. Morainal bank and associated outwash fan deposits are shown for reference. Observed sediment plumes (2008-2013) are shown as pink overlays. Modelled subglacial water flowpaths are shown in gray-scale.

2.8. Supporting Information

We assess other potential contributors to undercutting at the glacier front by evaluating the likelihood of upward flexure at the terminus due to buoyancy forces and estimating the size of subglacial channels. We find that the KS terminus is above flotation using several lines of evidence. First, we produce a height above flotation map (Figure 2.5) using GIMP ice surface [*Howat et al*., 2014] and mass conserving bed elevation [*Morlighem et al*. 2014] datasets in the equation for hydrostatic equilibrium. The map reveals that the entire terminus region is 10 - 200 m above flotation. Second, we do not find surface relaxing or closing of surface crevasses in longitudinal profiles near the terminus (in available World-View images) that would accompany upward flexure.

We use a model of subglacial channel cross-sectional area [*Schoof*, 2010] to estimate the upper limit of conduit enlargement at the terminus. We assume that channels there are on the order of 20 m wide, flow at capacity along the hydraulic gradient and experience no creep closure due to water pressure at overburden. Under these conditions, modeled channels widen radially at ~1 m d^{-1}. Integrated over the observation period coincident with our measurements of terminus position change, this yields a 20 m conduit radius and accounts for 11% of the observed outlet size at the terminus prow. At secondary discharge outlets, particularly along the southern terminus face, conduit sizes and their discharge are likely smaller, diminishing the potential contribution of conduit enlargement by viscous energy dissipation.

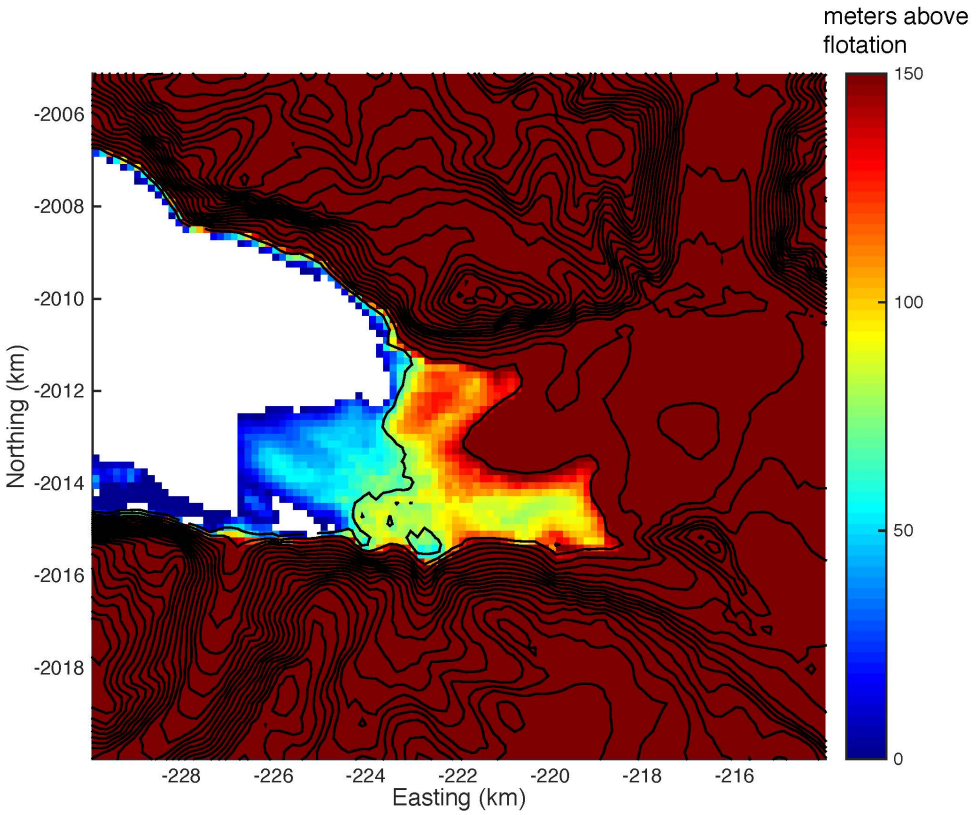

Figure 2.5. Height above flotation map for KS terminus region. Colorscale is meters above flotation.

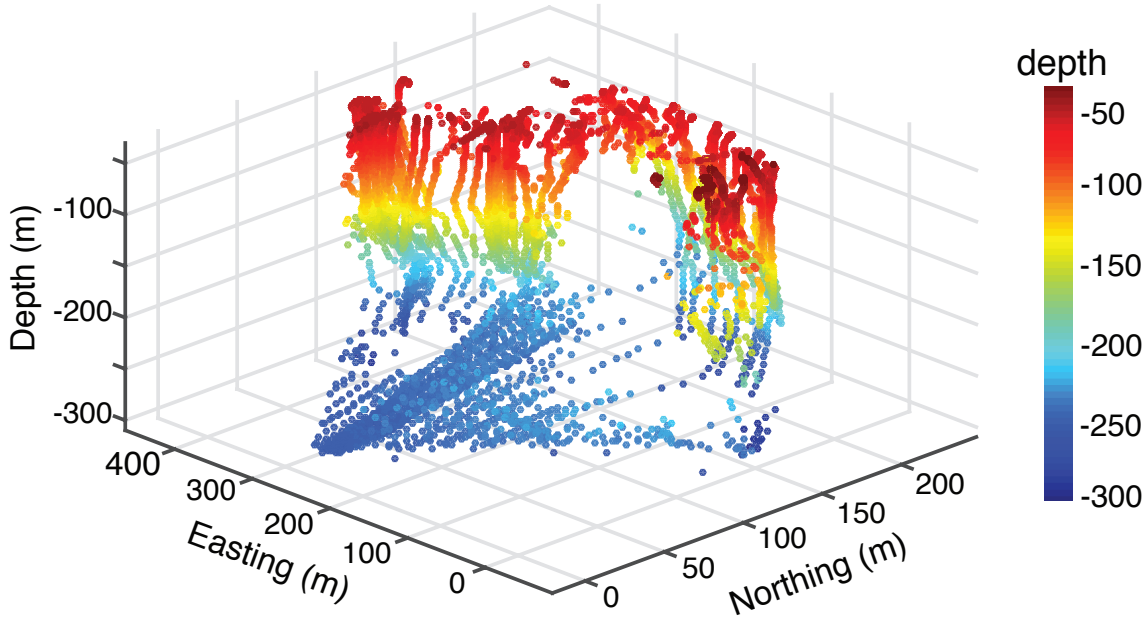

Figure 2.6. Oblique-view through multibeam data showing the terminus prow discharge outlet (discharge outlet #5).

Chapter 3. Reconciling controls on seasonal terminus advance and retreat at central west Greenland tidewater glaciers

3.1. Abstract

Each year, most Greenland tidewater glaciers undergo a seasonal cycle in terminus position, characterized by wintertime advance and summertime retreat. Understanding mechanisms that control seasonal cycles might elucidate how tidewater glaciers regulate dynamic ice loss on longer timescales. However, controls on terminus position are numerous and complex. To address this, we compare time series of satellite-derived terminus positions for tidewater glaciers in central west Greenland with observations of environmental forcings, including runoff at the glacier grounding line, mélange presence and ocean temperature in the proglacial fjord. We show that, for most glaciers in our region, seasonal terminus positions are more sensitive to glacial runoff than mélange or ocean thermal forcing. The strength of this relationship differs for two end-member glacier types in the region, defined by their terminus geometry and dominant calving style. First, we find a strong relationship between magnitudes of runoff and terminus retreat at shallow tidewater glaciers that calve primarily through small-magnitude serac failures. At these glaciers, subglacial plumes drive submarine melt and locally enhance retreat, causing heterogeneous position change across the terminus and the development of local embayments where seasonal terminus changes are largest. In contrast, deep termini susceptible to buoyant flexure retreat sporadically through full ice-thickness calving events less dependent on runoff. While less common, these glaciers deliver large

ice fluxes to the ocean. With predicted surface melt increases and diminished mélange coverage in a warming climate, our results reveal the impact of environmental forcings on the diversity of tidewater glacier systems in the region.

3.2. Introduction

The Greenland Ice Sheet (GrIS) rapidly lost mass over the last two decades (up to 400 Gt yr^{-1}) [*Shepherd et al.,* 2012; *Velicogna et al.,* 2014; *van den Broeke et al.*, 2016], with the greatest thinning focused where the ice sheet intersects the ocean at glacier termini [*Csatho et al.,* 2014; *Kjeldsen et al.,* 2015; *Felikson et al.,* 2017]. The termini of tidewater glaciers respond to processes acting in the ocean, atmosphere and ice sheet systems. Recent work shows that terminus perturbations at tidewater glaciers are responsible for the observed pattern of interior mass loss [*Felikson et al.,* 2017] and are likely initiated by processes acting at the ice/ocean interface [*Nick et al.,* 2009; *Murray et al.,* 2010; *Straneo and Heimbach,* 2013; *Cook et al.,* 2016].

Most Greenland tidewater glaciers undergo seasonal cycles in terminus position, characterized by wintertime advance and summertime retreat [*Moon et al.,* 2008; *Howat et al.,* 2010; *Schild and Hamilton,* 2013; *Moon et al.,* 2014]. For glaciers undergoing long-term dynamic adjustments, this seasonal cycle is superimposed onto a multi-year terminus retreat [*McFadden et al.,* 2011; *Carr et al.,* 2014; *Murray et al.,* 2015a]. While terminus positions reflect integrated effects from a range of forcing mechanisms, several leading mechanisms have emerged as potential drivers of seasonal terminus change including; 1) ice mélange buttressing; 2) increased runoff and related discharge-driven

submarine melt and; 3) warm ambient ocean-driven melt. In this paper, we evaluate these potential forcings in detail.

First, some mélange with dense concentrations of large icebergs in a sea ice matrix acts as a weak, granular ice shelf. This mélange can impart a back-pressure on the terminus [*Walter et al.,* 2012; *Cassotto et al.,* 2015], inhibiting calving and promoting glacier advance [*Admundson et al.,* 2010; *Walter et al.,* 2012; *Todd and Christoffersen,* 2014; *Cassotto et al.,* 2015]. Supporting observations show that mélange breakup can correlate with increased calving [*Cassotto et al., 2015*] and terminus retreat [*Moon et al., 2015*]. Second, increases in seasonal runoff can affect terminus position by either promoting faster glacier flow through enhanced basal lubrication [*Joughin et al.,* 2008; *Moon et al.,* 2014], and by enhancing submarine melt at the terminus through discharge-driven, upwelling plumes [*Motyka et al.,* 2003; *Rignot et al.,* 2010; *Motyka et al.,* 2013; *Carroll et al.,* 2015; *Slater et al.,* 2015; *Fried et al.,* 2015; *Carroll et al.,* 2016]. These plumes trigger calving through submarine thermal undercutting [*Motyka et al.,* 2003; *O'Leary and Christoffersen,* 2013; *Bartholomaus et al.,* 2013; *Fried et al.,* 2015]. Finally, glacier termini melt subaqueously when ambient seawater is above the pressure-salinity-dependent freezing point [*Straneo et al.,* 2010; *Straneo et al.,* 2013; *Truffer and Motyka,* 2016]. Ocean observations reveal that relatively warm ocean waters originating outside of glacier fjords can melt the terminus during winter [*Jackson et al.,* 2014], potentially influencing terminus behavior in the absence of subglacial discharge [*Luckman et al.,* 2015; *Shroyer et al.,* 2017].

While these processes can all impact the terminus, we lack comparative studies that use contemporaneous observations to quantify and attribute terminus position changes to individual forcing mechanisms. To address this, we examine seasonal terminus changes due to different forcing mechanisms for a suite of glaciers in central west Greenland (Figure 3.1). We survey 13 tidewater glaciers that span a range of grounding line depths, calving styles, and fjord environments – including Rink Isbrae (RNK), the seventh largest discharger of ice in Greenland [*Enderlin et al.,* 2014] – in order to identify processes that best explain seasonal terminus variability within our region of interest. In turn, this analysis may aid understanding of how tidewater glaciers regulate dynamic ice loss on longer timescales. While four major GrIS tidewater glaciers accounted for half of the total ice sheet mass loss between 2000-2012, the remaining loss came from over 80 smaller glaciers [*Enderlin et al.,* 2014; *McMillan et al.,* 2016] that often lack persistent year-round mélange in their fjords. Despite their cumulative importance to ice sheet mass balance, small tidewater glaciers suffer from observational bias and are underrepresented in process studies. Thus, we meet an additional goal: better understanding of the processes controlling seasonal terminus cycles across a range of glacier geometries within our study area in order to highlight the diversity of GrIS tidewater glaciers.

3.3. Data and Methods

3.3.1. Terminus position data

We characterize seasonal terminus cycles using high-temporal resolution, satellite-derived terminus position records for 13 tidewater glaciers in the Uummannaq Fjord and upper Disko Bay regions of central west Greenland (Figure 3.1a) from 2013-2016. To accomplish this, we use Landsat (Level 1T, 30-m resolution), Advanced Spaceborne Thermal Emissivity and Reflection Radiometer (ASTER, 15-m resolution) and TerraSAR-X imagery (courtesy of the German Aerospace Center, DLR, 20-m resolution) to manually digitize successive glacier terminus positions following *MacGregor et al.* [2012] using Esri ArcGIS software. Cloud obscured imagery precludes a constant terminus sampling frequency; however, the typical resolution is 1.5 weeks for each glacier. TerraSAR-X images were manually georeferenced relative to a single Landsat scene (LC80120101201418 9LGN00) if they had poor co-registration. TerraSAR-X images have the advantage of providing terminus information during the winter when optical imagery (Landsat and ASTER) cannot. We study terminus positions over the time period between 2013-2016 for several reasons; 1) to better isolate seasonality from longer-term changes in retreat rate; 2) increased sampling frequency of imagery during this period – critically in late fall and early spring following the deployment of Landsat 8 in 2013 and; 3) to overlap with the deployment of several in-situ observational datasets in the region. We present and analyze extended time series for three glaciers (UMI, RNK and KAS identified in Figure 3.1a), where additionally

acquired TerraSAR-X imagery facilitates sufficient fall, winter and spring observations back to 2009 at RNK and KAS and 2012 at UMI (Supporting Information).

We use this database of terminus positions to calculate the change in terminus area between consecutive terminus traces, the glacier fjord margins and a constant upstream gate (Figure 3.1b). The average glacier length change is then computed by normalizing terminus area by the glacier width (Figure 3.2a). From these terminus length changes, we remove the long-term (interannual) trend by subtracting the least-squares linear fit from the terminus time series and normalize by removing the terminus length in the first record to obtain terminus position (blue line in Figure 3.2a). Our survey of 13 glaciers does not include two neighboring glaciers, Ingia Isbrae and Perlerfiup Sermia, that underwent large, multiyear retreats for the entire duration of the study period (3.2 km and 2.5 km, respectively), which significantly altered their seasonal cycle. Terminus position uncertainties are evaluated based on image co-registration error and operator error during manual digitization estimated from repeated digitization of the same terminus. Using these error sources, standard error propagation yields a total uncertainty of ±13 m. Using these terminus records, we then evaluate whether seasonal terminus cycles best correspond to variability in mélange, runoff or ocean temperature.

3.3.2. Atmospheric data

We use downscaled RACMO2.3p2 1-km surface mass-balance products [*Noël et al.*, 2017] to produce records of daily runoff for each glacier between 2013-2016. Runoff produced at the glacier surface can drain efficiently to the bed via moulins [*Catania and Neumann,* 2010; *Smith et al.,* 2015], where it flows towards the terminus as subglacial

discharge. We calculate the gradient in the subglacial hydraulic potential [*Shreve,* 1972] using GIMP ice surface [*Howat et al.,* 2014] and mass conservation bed topography [*Morlighem et al.,* 2017] in order to delineate individual subglacial catchments and integrate daily runoff values from RACMO2.3p2 exported to each glacier terminus (Figure 3.2c). In light of the focus of this study on seasonality, we assume that all runoff in the catchment arrives at the terminus instantaneously (e.g. *Carroll et al.*, 2016; *Bartholomaus et al.*, 2016).

Modelled RACMO2.3p2 2-m air temperatures and surface mass balance (SMB, m w. e. yr^{-1}) are in good agreement with air temperature measurements from 23 automatic weather stations (r^2 = 0.95 and root-mean-square error of ~2.4 ºC) and 1073 SMB stake observations (r^2 = 0.73 and root-mean-square error of 0.87) across the GrIS ablation zone [*Noël et al.*, 2017]. Together, these metrics give confidence that we appropriately resolve runoff over the study area. We further validate the timing of runoff using an air temperature time series from an on-ice Vaisala WXT520 automatic weather station installed in our study area (Figure 3.1a and black line in Figure 3.2c).

The turbid surface expressions of subglacial plumes in fjords at tidewater glacier termini act as a proxy for the location and timing of runoff [*Chu et al.,* 2012] and submarine melt [*Fried et al.,* 2015]. However, their absence does not necessarily contradict subglacial discharge because subglacial plumes may not reach the fjord surface during times when the upper water column stratification in the fjord is strong, discharge fluxes are small, or for glaciers with deep grounding lines [*Bartholomaus et al.,* 2016, *Carroll et al.,* 2016]. To track the occurrence of subglacial plumes, we manually digitize

the turbid extent of plumes observed at the fjord surface near the glacier terminus using Landsat 7, Landsat 8 and ASTER images during the 2013-2016 melt seasons (timing of observed plume emergence is shown as pink circles in Figure 3.2c). Manual digitization has the added benefit of discriminating against subaerially derived sediments, such as from surface streams along the fjord margins. Time-lapse cameras (30-minute sampling rate when operational) installed at three tidewater glaciers in our study area (Figure 3.1; KAS, RNK and UMI) supply additional observations and validation of subglacial plumes identified from satellite imagery (Figure 3.2c). Time lapse imagery confirm the location and persistence of dominant subglacial plumes identified in satellite imagery.

3.3.3. Oceanic data

Unlike persistent, year-round mélange that occurs in a few large Greenland fjord systems (e.g. Jakobshavn Isbrae in *Cassotto et al.,* 2015), fjords in our region of interest contain seasonal mélange occurring from mid-winter to early summer. The character of this mélange is also starkly different than that found at Jakobshavn Isbrae or Helheim Gletscher. Rather than 10s of kilometers of densely packed, 100+ m icebergs [*Cassotto et al.,* 2015], the mélange in our study area has more in common with seasonal sea ice containing sparse icebergs. We characterize the timing of mélange coverage following methods outlined in *Moon et al.* [2015], and track mélange presence in each glacier fjord throughout the observational period using Landsat, ASTER and TerraSAR-X imagery (black and yellow circles in Figure 3.2d). We augment this record from 07/2013 to 09/2015 using time-lapse cameras at KAS, RNK and UMI. In addition, we validate and constrain the timing of early-summer mélange breakup in each fjord using 250-m

resolution, daily Moderate Resolution Imaging Spectroradiometer (MODIS) surface reflectance data (level 2G). To accomplish this, we survey mélange and fjord surface reflectance values within a polygon in the proglacial fjord (typically within 4 km of the terminus; e.g. Figure 3.1b) and classify mélange as present when more than 90% of pixel values exceed ocean reflectance (blue line in Figure 3.2d). We exclude MODIS images obscured by clouds.

We use moored ocean temperature records in order to infer the impact of ocean thermal forcing on seasonal terminus positions at UMI, RNK and KAS. We deployed moored SBE 56 and SBE 37-SM temperature recorders in KAS and RNK fjords (moorings KSD and RKD, respectively, in Figure 3.1a) and near the head of UMI and RNK fjords (mooring RKS in Figure 3.1a) between 2013-2015. These moorings measured ocean temperature at ~20 m depth intervals that span the majority of the water column (between 450 and 130 m below sea level in KAS fjord; 950 and 670 m in RNK fjord; and 400 and 250 m at the head of UMI and RNK fjords), including the grounding line depth [*Rignot et al.,* 2016a] for each glacier (grey and blue lines in Figure 3.2b and 3.5). We use the RKS mooring at the head of UMI and RNK fjords to infer ocean temperature between 400 and 250 m below sea level in both of these fjord systems. These deep records are supplemented with a shallow moored Onset temperature recorder near KAS terminus (mooring KSP in Figure 3.1a,b) capturing temperatures in the upper 20 m (green line in Figure 3.2b). SBE 56 and SBE 37-SM recorders are accurate to ±0.002˚C ($1x10^{-4}$ ˚C resolution) and Onset recorders to 0.2 ˚C (0.025 ˚C resolution). Direct comparisons between ocean temperature and terminus positions are limited to these three

glacier systems where mooring data exists. However, we note that seasonal water properties within these fjords reflect those in outer Uummannaq Bay [*Bartholomaus et al.,* 2016].

3.3.4. Terminus velocity data

We constrain seasonal velocity variations for each glacier between 2013-2016 using a combination of publically available ice velocity products derived from optical (*Fahnestock et al.*, 2015; *Roseneau et al.*, 2015; *Scambos et al.*, 2016; *Howat et al.*, 2017) and radar (*Joughin et al.*, 2010; 2011) imagery. For each velocity epoch, we determine the width-averaged velocity within 2 km of the terminus and account for concurrent terminus advance or retreat. We describe the seasonal velocity cycle for each glacier in more detail in the Supporting Information (Figure 3.13).

3.4. Results

3.4.1. Seasonal terminus cycles and calving styles

In our study area, seasonal tidewater glacier terminus position cycles range from 150 to 1000 m and are typified by terminus advance occurring between fall and spring (~September to May) followed by rapid summertime retreat (~June to August) (Figure 3.3). The amplitude and smoothness of seasonal cycles varies between glaciers, indicative of their varying calving styles and helping to define two end-member glacier types within the study area (Figure 3.3). One glacier type is characterized by large amplitude seasonal cycles (mean ~750 m) and sporadic, year-round retreat events (Figure 3.3a). Three of these glaciers are found in our region of interest (RNK, SIL and STR) where field

observations and satellite imagery reveal that they are dominated by full-thickness, capsizing slab and rifting tabular calving events (Figure 3.4). This calving style indicates, in part, that their termini are floating. RNK maintains a ~9 km^2 floating tongue [*Bartholomaus et al.,* 2016] that periodically produces rifting tabular calving events (Figure 3.4a) and STR intermittently forms a floating tongue when the terminus advances seaward of its morainal bank [*Walter et al.,* 2012]. At SIL, we use a 2-m strip DEM (ArcticDEM release 6 from the Polar Geospatial Data Center) to identify a broad flexure zone defined by a ~20 m deep across-flow trough in the surface topography located ~250 m up-glacier (Figure 3.4b). Through comparison with observations elsewhere in Greenland [*James et al.,* 2014], we infer this transverse depression to reflect a terminus affected by buoyancy forces. This trough defined the upstream extent of a capsizing slab-style calving event that subsequently filled the fjord with broken ice debris (Figure 3.4b). In map-view, full-thickness calving events can span >75% of the glacier width, causing single day terminus retreats in excess of 250 m following steady months-long advance (Figure 3.3a). We catalogue the timing and magnitude of large retreat events at RNK, SIL and STR in the Supporting Information (Tables 3.1-3.3). In contrast, the remaining glaciers in our study area comprise a second glacier type characterized by smoother, smaller amplitude seasonal terminus cycles (mean of ~300 m; Figure 3.3b). These glaciers calve predominantly through smaller, localized serac failure events (10 – 100 m scale).

3.4.2. Terminus correspondence to ocean thermal forcing

We use coincident mooring and terminus data at KAS, RNK and UMI to investigate the correspondence between ocean temperature and seasonal terminus cycles (Figure 3.5). Deep moored ocean temperature records reveal an influx of warmer water (observed between 130 m and 950 m) from approximately January until April/May followed by a gradual decrease in ocean temperature until September in all three fjords (Figure 3.5). These changes in ocean thermal forcing are, however, anticorrelated with expected terminus positions changes; seasonal warming coincides with advance while seasonal cooling coincides with retreat (Figure 3.5). We find this relationship at all three glaciers (Figure 3.5), despite their varying grounding line depths, calving styles and bathymetric connections to warm Atlantic water in Uummannaq Bay [*Bartholomaus et al.,* 2016]. Seasonal ocean temperatures vary near-homogeneously by ~1˚C across the majority of the KAS submarine terminus face and by less than 0.75˚C in RNK and UMI fjords (Figure 3.5), however these differences do not drive commensurate amplitude changes in terminus position between the glacier systems. Deep temperatures near the grounding lines remain positive year-round, while near-surface ocean temperatures (15 m depth) warm above zero in the summer after sea ice breakup and lag air temperature and runoff production (Figure 3.2). We note that warm water at these shallow depths has a negligible impact on melting at deeper (>30 m) depths along the submarine terminus face.

3.4.3. Terminus correspondence to mélange and runoff

For most glaciers, we observe coincident terminus advance/retreat when runoff is off/on (Figure 3.2 and Supporting Information). Seasonal retreat often initiates near the start of runoff production and as mélange clears from the fjord (e.g. Figure 3.2). However, for most glaciers, the timing of terminus advance initiates within weeks of runoff cessation and several months before winter mélange formation (Figure 3.2 and Supporting Information). These observations motivate further characterization of seasonal cycles and their response to runoff and mélange variability across the region of interest.

To constrain the impact of these potential forcing mechanisms, we calculate cumulative terminus position change during periods when mélange and runoff were present or absent. We treat terminus advance and retreat separately to test the hypotheses that mélange presence/lack of runoff promotes terminus advance and mélange absence/increased runoff promotes retreat. Thus, for each glacier, we calculate the percentage of total seasonal advance/retreat in relation to the cumulative terminus position change coincident with each forcing mechanism. To illustrate this technique, we consider two hypothetical glacier terminus examples (Figure 3.6). The first example (glacier ‘a’) is runoff-driven with a terminus that advances 150 m during both time periods when runoff is off and retreats 300 m when runoff is on. Because runoff-driven terminus change may overlap with switches in mélange conditions, we additionally quantify terminus change at glacier ‘a’ coincident with the presence and absence of mélange. Thus, for glacier ‘a’, we find that changes in runoff correspond to 100% of the

observed terminus change while only 25% coincides with changes in mélange conditions (Fig. 6a). In contrast, glacier 'b' is mélange-driven and experiences a 300 m advance when mélange is present and a 300 m retreat when mélange is absent (Fig. 6b,c). Thus, mélange conditions correspond to 100% of the terminus change at glacier 'b' while only 20% coincides with switches in runoff (Figure 3.6b). To best link terminus changes with environmental forcings, we consider seasonal cycles between the first and last visible images available each year. This visible period generally excludes mid-November through January unless sufficient TerraSAR-X imagery are available.

We perform this analysis for all glaciers in our region and find that, for the majority of glaciers, more than 65% of their individual seasonal cycles (both advance and retreat phases) correspond to changes in runoff in all years (Figure 3.7). Terminus changes are most sensitive to runoff at glaciers with small amplitude seasonal cycles (< 500 m) that calve primarily via serac failures (KNG, KAS, UMI, LIK, AVA, KAN, LIL, KUJ, EQP, and KSS in Figure 3.7). Extended records at KAS and UMI confirm the correspondence of seasonal terminus cycles with runoff at serac failure glaciers for previous years (Figure 3.11). These smaller, runoff-driven tidewater glaciers strongly influence regional terminus position change. Changes in runoff correspond to 73% of total terminus retreat and advance, aggregated for all glaciers over the four-year study period (Figure 3.7).

Regionally, seasonal terminus cycles are less sensitive to mélange conditions. Changes in mélange correspond to 53% and 47% of total regional terminus retreat and advance, respectively, aggregated over the study period (Figure 3.7). Seasonal cycles are

least sensitive to mélange conditions at smaller serac failure glaciers. At these glaciers, mélange-free periods capture less than 25% of total seasonal retreat in some individual cases (e.g. KNG in 2013 and 2014). Mélange conditions also generally do not strongly correspond with their seasonal advance (Figure 3.7), except for at a few glaciers in single years (e.g. KUJ in 2014 and LIK in 2016). These mismatches are largely the consequence of serac failure glaciers initiating their seasonal advance months before mélange formation when runoff ceases (e.g. KAS in Figure 3.2). Similarly, terminus advance can persist after mélange breakup; more than 40% of springtime advance at KAN occurred after mélange breakup in both 2014 and 2016 (Figure 3.25). In contrast, terminus cycles better correspond to mélange conditions at larger, full-thickness calving glaciers in the study area (STR, RNK and SIL, bottom panels in Figure 3.7). At these three glaciers, mélange-free conditions correspond to 61% of total aggregated terminus retreat, matching the correspondence to runoff (Figure 3.7). Extended records show seasonal terminus cycles best correspond to mélange conditions at RNK between 2009 and 2012 (Fig. 3.11).

In clear contrast to serac failure glaciers, the dominant contributor to terminus change is not consistent at STR, RNK and SIL (bottom panels in Figure 3.7). Seasonal cycles for these glaciers better coincide with both mélange and runoff intermittently throughout the study period, which prevents strong correspondence with either environmental forcing mechanism. The high degree of variability at these glaciers and the absence of a clear leading control on their seasonal cycles is related to their sporadic, full-thickness calving behavior.

3.4.4 Runoff, retreat and calving styles

To correlate seasonal terminus change and runoff at glaciers with different calving styles, we separate out glaciers that calve via serac failure versus those that predominantly produce full-thickness icebergs (RNK, SIL and STR). We then calculate a time series of terminus change and runoff integrated over two week periods for each glacier group (Figure 3.8a and 3.8b). From these data, we perform linear regressions between integrated terminus retreat and runoff to evaluate whether terminus change scales with runoff (Figure 3.8c and 3.8d). We do not consider magnitudes of terminus advance as they are unrelated to runoff magnitudes in this analysis. We find a strong, linear relationship between the magnitude of runoff and terminus retreat ($R^2 = 0.76$) at serac failure glaciers (Figure 3.8c), indicating more retreat at these glaciers would occur when runoff is large. We find a weaker correlation ($R^2 = 0.45$) between magnitudes of runoff and terminus retreat at full-thickness calving glaciers (Figure 3.8d) in part because there are more frequent large retreat events outside of the melt season and terminus advance and modest retreat events within the melt season. While the correlation is weaker at these glaciers, we still observe overall terminus retreat during active runoff periods (Figure 3.8d).

We evaluate the strength of these relationships using two statistical methods. First, we calculate the nonparametric Spearman's rank coefficient (r_s, in Figure 3.8c and 3.8d) in order to measure the rank correlation between runoff and terminus retreat. Using this statistic, we find a stronger, statistically significant ranked relationship ($r_s = 0.76$ with an associated p-value of 3.5e-17) between runoff and terminus retreat at glaciers that

calve primarily from serac failures. Second, we apply a bootstrap method to assess the stability of our regression analyses (Davison and Hinkley, 1997). To accomplish this, we randomly resampled runoff and terminus retreat values with replacement to populate new datasets of the same length as the original time series. We performed 100 resamples for each glacier type and calculated linear regression slopes and R^2 values for each resample. We then sorted the resulting regression slopes and R^2 values distributions and discarded the upper and lower 2.5% to produce 95% confidence intervals for both statistics (Figure 3.12). Using this analysis, we calculate R^2 point estimates of 0.77 and 0.47 for serac failure glaciers and full-thickness calving glaciers, respectively, again confirming a stronger relationship at serac failure glaciers. Additionally, 95% confidence intervals do not include negative or zero regression slopes for either glacier type (Figure 3.12), adding further confidence in a positive, scaled relationship between runoff availability and terminus retreat.

3.4.5. Terminus retreat from discharge-driven submarine melt

We assess the influence of runoff on seasonal cycles in more detail by examining heterogeneity in across-glacier terminus positions, focusing on locations where subglacial discharge emerges and submarine melt is inferred from turbid subglacial plumes identified at the fjord surface. We find that local embayments in the terminus – where retreat rates are largest – are created in regions around subglacial plumes (Figure 3.9). For example, EQP forms a broad, seasonal retreat embayment around a subglacial plume occurring each melt season and discharging at the terminus center (Figure 3.9). The embayment expands across the glacier each July, spanning ~40% of the glacier width and

~700 m up-glacier, removing a ~0.75 km^2 area during the summer (Figure 3.9). A second plume toward the southern glacier margin forms a smaller, secondary embayment later in the season in 2014 and 2015 and removes ~0.25 km^2 from the terminus in those years (Figure 3.9). In contrast, parts of the terminus outside of the plume region remain relatively stable. Readvance within embayments initiates immediately after runoff ceases and persists throughout the autumn, well before seasonal mélange resets in winter (Figure 3.9).

We examine this relationship in more detail at three representative glaciers (two that calve primarily via serac failures and one from full-thickness, capsizing slab events) by constructing a set of three, 250 m wide sampling boxes spanning the terminus, where the local terminus position is determined as the change in box area enclosed by successive terminus traces divided by the box width. We orient sampling boxes locally normal to the terminus face and acknowledge some termini become concave during seasonal retreat. We correlate the timing of calculated terminus changes with local concentrated subglacial discharge when individual sampling boxes overlap any fraction of turbid subglacial plumes identified in satellite imagery at the fjord surface (Figure 3.10).

We find that the greatest seasonal terminus retreat occurs in regions closest to persistent subglacial plumes (Figure 3.10). At KAS, a subglacial plume forms at the center of the terminus each melt season between ~ mid-June and mid-August and is well-correlated with enhanced seasonal terminus change here; rapid retreat initiates at the onset of plume production in June and gradual terminus re-advance starts immediately

after the plume shuts off in mid-August (box 2 in Figure 3.10b). Further, the seasonal amplitude is ~750 m greater in this central portion of the terminus than in remaining sampling boxes where the seasonal cycle is muted (Figure 3.10b) and thus dominantly influences calculation of the mean terminus position (Figure 3.2a).

In the case of KAS, runoff is fed by a stable subglacial channel as indicated by the plume at the center of the terminus that persists through our observational period (*Fried et al.,* 2015; Figure 3.10a). This is not always the case at other glaciers. At KAN, plumes switch locations over time causing different portions of the terminus to undergo accelerated retreat when active (Figure 3.10d). For example, during summer 2013, the largest and most frequent plume occurred near box 2, causing ~600 m of local terminus retreat (Figure 3.10d). However, the terminus retreated less than 100 m at the same location in 2014 and 2015 when visible plumes were absent from this area (Figure 3.10d). Coincidentally, the terminus retreated >600 m each year within a second plume region near box 1.

We find limited evidence of turbid subglacial plumes emerging at the fjord surface for deep glaciers with frequent full-thickness calving events and where terminus changes are weakly correlated with modeled runoff variations (RNK, SIL and STR). Subglacial plumes are less likely to reach the fjord surface here due, in part, to their deep grounding lines [*Carroll et al.,* 2016; *Rignot et al*., 2016a]. These glaciers experience comparatively homogeneous advance and retreat rates across their termini with no prominent seasonal embayments (e.g. SIL, Figure 3.10e,f). Such terminus adjustments

can coincide with changes in mélange conditions. For example, advance rates at SIL accelerate with springtime mélange presence each year (Figure 3.10f).

3.5. Discussion

While recent studies have implicated subsurface ocean temperature [*Luckman et al.,* 2015] and mélange [*Moon et al.,* 2015; *Cassotto et al.,* 2015] as the principle controls on terminus position changes elsewhere, we find that the situation is different for the glaciers studied in central west Greenland and that, overall, seasonal tidewater glacier terminus advance and retreat best corresponds to runoff variability (Figure 3.7). Further, the strength of this correspondence differs drastically for two end-member tidewater glacier types identified in the study area, defined principally by their terminus geometry (i.e. grounding line depth and susceptibility to buoyancy forces) and therefore their dominant calving style.

Runoff is the strongest predictor of terminus change at glaciers with shallow grounding line depths that calve primarily through small-magnitude serac failures (Figure 3.7 and 3.11). At these glaciers, we observe a strong and linear relationship between runoff flux and terminus retreat (Figure 3.8c and 3.12). This correspondence is due, at least in part, to the impact of discharge-driven submarine melt at the ice/ocean interface (Figure 3.9 and 3.10). During the runoff season, submarine melt rates are most likely to match or exceed ice fluxes – and force retreat – at smaller serac failing glaciers due to their low ice velocities [*Rignot et al.,* 2016b; *Slater et al.,* 2017]. Shallow grounding line depths (<400 m) also permit subglacial plumes to rise to the fjord surface and retain their

upwelling velocity along the entire terminus face, a process that amplifies depth-averaged melt [*Carroll et al.,* 2016]. Under these conditions, submarine melt can lead to extensive terminus undercutting [*Motyka et al.,* 2003; *Motyka et al.,* 2013; *Rignot et al.,* 2015; *Fried et al.,* 2015; *Slater et al.,* 2017], which can trigger calving [*Vieli et al.,* 2001; *O'Leary and Christoffersen,* 2013; *Bartholomaus et al.,* 2013] by connecting undercut cavities with overlying surface crevasses [*Fried et al.,* 2015]. As a result, we find that plumes locally enhance summertime retreat rates, causing heterogeneous across-flow terminus position changes, or the development of seasonal terminus embayments (Figure 3.9 and 3.10), which produce characteristically crenulated terminus shapes [e.g. *Chauché et al.,* 2014]. Because subglacial discharge follows the subglacial hydraulic potential gradient, the largest discharge outlets are often located in the deepest sections of the fjords [*Truffer and Motyka*, 2016]. If large seasonal embayments occur in topographic overdeepenings, these areas may act as nucleation points for future, sustained retreat. This mechanism was hypothesized to help initiate multiyear retreat at Narsap Sermia in southwest Greenland [*Motyka et al.,* 2017].

In contrast to small-magnitude serac failure glaciers, RNK, SIL and STR have relatively deep grounding lines (>400 m) [*Rignot et al.,* 2016a] and their termini periodically or permanently forming floating tongues [e.g. *Bartholomaus et al.,* 2016; *Walter et al.,* 2012]. As a result, these glaciers produce large-magnitude full-thickness capsizing slab and rifting tabular calving events (Figure 3.4), which exceed localized retreat from submarine melt. Under these conditions, terminus positions largely depend on buoyant flexure (Figure 3.4b) at the glacier front [*James et al.,* 2014; *Murray et al.,*

2015b] set by the ice thickness/water depth ratio and the propagation of buoyancy-induced basal crevasses [*Murray et al.,* 2015b; *Wagner et al.,* 2016]. It remains poorly understood how terminus undercutting from submarine melt might affect calving frequency at these types of glaciers, as calving likely outpaces undercutting, but it is possible subglacial discharge enlarges basal crevasses initially formed due to buoyancy forces. Year-round full-thickness calving events partly obscure our ability to make strong correlations between terminus change and environmental forcings, however these glaciers typically have relatively fast ice speeds (>7 m d^{-1}), which limits their sensitivity to melting from subglacial plumes [*Truffer and Motyka,* 2016; *Carroll et al.,* 2016; *Rignot et al.,* 2016b; *Slater et al.,* 2017]. As a result, the glaciers in the study area with the largest ice fluxes and ice discharges to the ocean are least sensitive to runoff variations.

It remains difficult to fully separate the influence of all processes related to runoff acting on the terminus. For some glaciers, the observed correspondence between runoff and terminus positions could be partly controlled by ice velocity variations tied to runoff increases. However, while tidewater glaciers in the study area are typified by similarly timed terminus cycles (Figure 3.3), their seasonal velocity cycles are variable and contrasting (Figure 3.13), similar to the disparate velocity patterns highlighted in Moon et al. [2014]. Indeed, seasonal velocity and terminus cycles often differ (Figure 3.14-3.26). For example, the four southernmost glaciers in the study area (AVA, KUJ, KAN and EQP) experience coincident terminus retreat and contrasting velocity trends over the same time period (between May/June and September; Figure 3.13 and 3.23-26). During their retreat, velocities increase to annual maxima in August at KUJ and EQP and

decrease from annual maxima in June at AVA and KAN. Similarly, KAS and UMI undergo similar terminus cycles despite their velocities being anticorrelated during summer (Figure 3.13). Seasonal velocity maxima occur outside of the runoff season at full thickness calving glaciers (October at RNK, December at SIL and February at STR in Fig. 3.13). While we cannot completely rule out the effect of glacier velocity on terminus positions, we find that seasonal velocity variations are not a consistent driver of seasonal terminus cycles across the study area.

We find that the majority of glaciers in our study area – most notably smaller, serac failure glaciers – are less sensitive to mélange conditions, a result that differs from previous studies [e.g. *Moon et al.,* 2015]. Some of the contrasts in results may arise from different study areas, but we believe the more important factor is completeness of record. Attribution of mechanisms forcing retreat may be confounded if mélange breakup and runoff production occur close in time and because subglacial plumes are only observable after mélange breakup. Additional observations through fall and winter reveal a clearer regional correspondence between terminus advance and runoff cessation rather than mélange formation.

While mélange does not completely explain their seasonal cycles, we find mélange is more impactful at three large tidewater glaciers in the study area (RNK, SIL, STR). For example, RNK most commonly produces tabular rift icebergs in late spring when the glacier and floating tongue are most advanced (Figure 3.4a), possibly due to mélange inhibiting preceding calving events. This evidence corroborates previous work done at Jakobshavn Isbrae by *Cassotto et al.* [2015], where persistent mélange plays a

role in determining terminus behavior, possibly inhibiting rotation needed for capsizing slab-style calving events. The same phenomenon is not observed at smaller, serac failure calving glaciers, where terminus advance is generally constant outside of the melt season (Figure 3.8a) and seasonal terminus position minima occur up to five months before the return of mélange in mid-winter. Finally, while our method does not detect them, we expect crucial differences in mélange rheology to occur across the study area depending on each glacier's dominant calving style and flux. Seasonal mélange at small tidewater glaciers is comprised of sea ice and sparse small icebergs, which differs dramatically from mélange forming at the largest Greenland tidewater glacier systems [e.g. *Amundson et al.,* 2010]. In turn, these differences may help determine mélange influence on the terminus.

Ocean thermal forcing plays an indirect role in regulating terminus positions at the three glaciers where we deployed ocean mooring observations. While Greenlandic fjords provide a pathway for consistent ocean heat transport to glacier termini [*Straneo et al.,* 2010; *Mortensen et al.,* 2011; *Jackson et al.,* 2014], ocean thermal forcing does not appear to directly control terminus position. Our observations suggest the impact of warm ocean waters on meaningful terminus retreat is conditional on entrainment in subglacial plumes, in agreement with the long-known dependence of submarine heat exchange and melt rate on subglacial discharge observed in Alaska [*Motyka et al.,* 2003; 2013]. These findings stand in contrast with observations in Svalbard, where seasonal terminus fluctuations were found to correspond with subsurface ocean temperature, rather than runoff or sea ice presence [*Luckman et al.,* 2015]. We note, however, that there may be

important differences in ocean circulation and heat transport between Greenland and Svalbard fjords, particularly notable is the close proximity of west Svalbard fjords to the warm West Spitsbergen current.

The degree to which fjord bathymetry affects warm water transport between the continental shelf and glacier termini, particularly in the presence of down-fjord sills, remains an important point of ongoing research. For example, we observe seasonal ocean temperature increases of generally less than 1 ºC at depth (Figure 3.5), which is smaller than the ~2-4 ºC temperature increases reported in Svalbard fjords [*Luckman et al.*, 2015]. While the magnitude of near-surface (~15-m) ocean thermal forcing in our region is greater than at deeper depths (Figure 3.2), we argue that its impact on terminus retreat is small and locally confined to the upper water column. Thus, the influence of shallow-ocean temperature on terminus-averaged melt will diminish with increasing grounding line depth.

Our interpretation does not necessarily discount the impact of large, multi-year ocean temperature anomalies on tidewater glacier terminus behavior, but instead emphasizes the likely critical role of runoff at seasonal timescales. We note it is possible that widespread increases in ocean heat content related to regional ocean current changes could amplify melt rates and initiate terminus position change on interannual timescales, as hypothesized at Jakobshavn Isbrae [*Holland et al.,* 2008; *Motyka et al.,* 2011], in southeast Greenland [*Murray et al.,* 2010] and the western Antarctic Peninsula [*Cook et al.,* 2016], given necessary entrainment of warm water at glacier fronts.

Our results highlight the implications of projected increases in atmospheric warming and ice surface melting for different types of GrIS tidewater glacier systems. Pronounced surface melt over consecutive years will inevitably aggravate seasonal terminus responses documented in this study and increase the likelihood of long-term terminus instability, particularly for smaller tidewater glaciers. Because roughly half of the dynamic mass loss from the GrIS comes from similar, smaller tidewater glaciers [*Enderlin et al.,* 2014; *McMillan et al.,* 2016], we suggest prognostic models of ice sheet behavior incorporate improved runoff estimates from regional climate models and work to parametrize the impact of subglacial plumes on a range of tidewater glacier systems.

3.6. Conclusions

We have presented a suite of observations comparing seasonal terminus cycles to environmental forcing mechanisms, which enable evaluations of the potential controls on terminus behavior at glaciers with a wide variety of geometries in central west Greenland. We find that processes controlling terminus positions largely depend on glacier calving style and flux set by terminus geometry. Seasonal terminus cycles at relatively shallow, slow-moving, serac failure calving glaciers are less dependent on mélange conditions and ocean forcing, but vary strongly with runoff production. At these glaciers, we find a strong, linear relationship between magnitudes of runoff and terminus retreat. Such a simple relationship may be useful for the development of terminus position parameterizations in numerical models of glacier and ice sheet change. Here, local retreat related to runoff-driven submarine melt strongly influences terminus-averaged seasonal

cycles and drives the formation of terminus embayments. In this scenario, ocean thermal forcing plays an indirect role by supplying heat to the terminus that is entrained in buoyant subglacial plumes, but cannot seasonally affect terminus positions in the absence of subglacial discharge. Also at small-magnitude serac failure calving glaciers, lapses in retreat correspond strongly with runoff cessation rather than mélange formation, with terminus advance remaining generally constant outside the melt season. In contrast, sporadic, year-round full-thickness calving partly obscures correlations between environmental forcings and terminus position changes at three deep glaciers in the study area whose termini are most susceptible to buoyancy forces. These tidewater glaciers are more sensitive to mélange presence than smaller serac failure calving glaciers. As a result, the few tidewater glaciers that have the largest calving fluxes and ice discharge contributions to the ocean feature seasonal cycles most weakly correlated with runoff variations.

3.7. Acknowledgements

This work was completed at the University of Texas at Austin and funded by NASA grant NM12AP50G and a University of Texas Institute for Geophysics Ewing/Worzel fellowship. TerraSAR-X imagery is courtesy of DLR and proposal HYD1925 to L.A.S.. We thank C. Black, D. Peters, A. Garcia and G. Hsu for assisting with terminus digitizing.

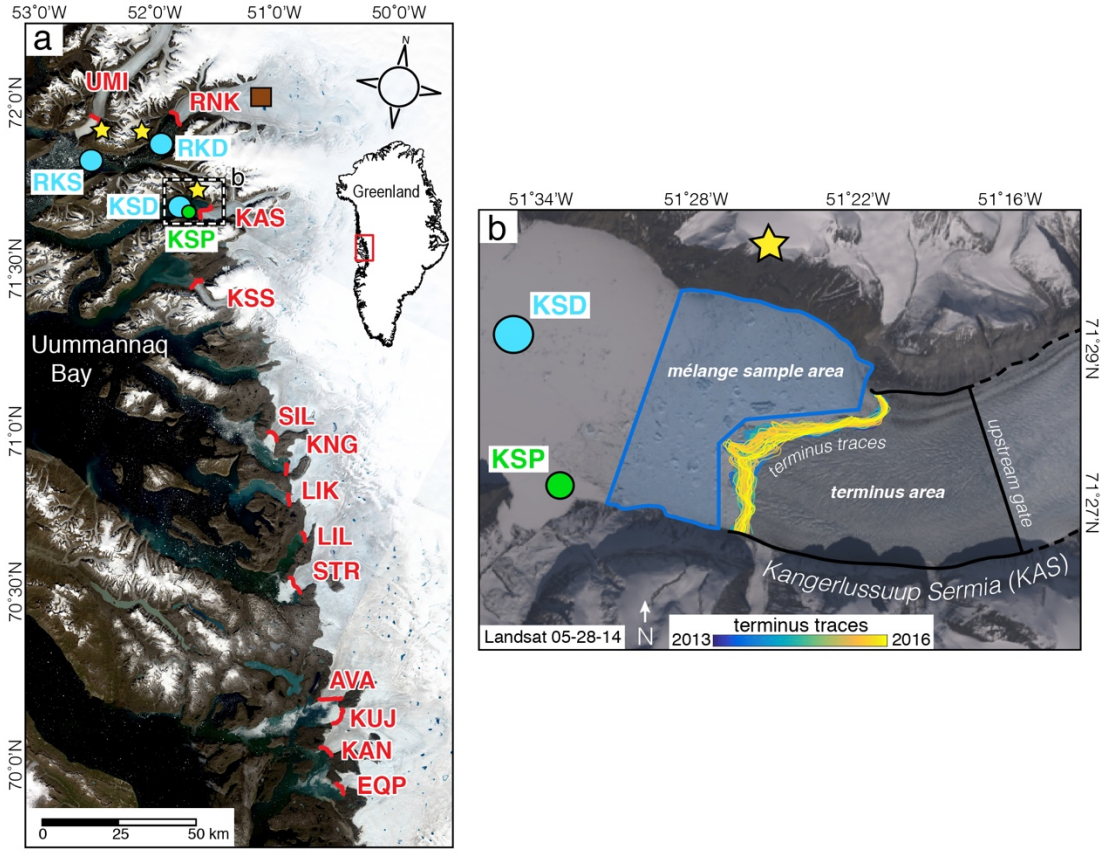

Figure 3.1. a) Tidewater glacier and instrument locations. Blue circles denote ocean-moorings (RKD, KSD, RKS); green circle denotes mooring near the fjord surface (KSP), yellow stars denote time-lapse cameras; brown square denotes on-ice meteorological station. Glaciers in the study include, from north to south: Umiammakku Sermiat (UMI), Rink Isbrae (RNK), Kangerlussuup Sermia (KAS), Kangerluarsuup Sermia (KSS), Sermeq Silarleq (SIL), Kangilleq (KAN), Sermilik Isbrae (LIK), Lille Gletsjer (LIL), Store Gletsjer (STR), Sermeq Avannarleq (AVA), Sermeq Kujalleq (KUJ), Kangilernata Sermia (KAN), Eqip Sermia (EQP). b) Overview of methods used at KAS. Terminus traces are shown as a time series of colors from blue to yellow.

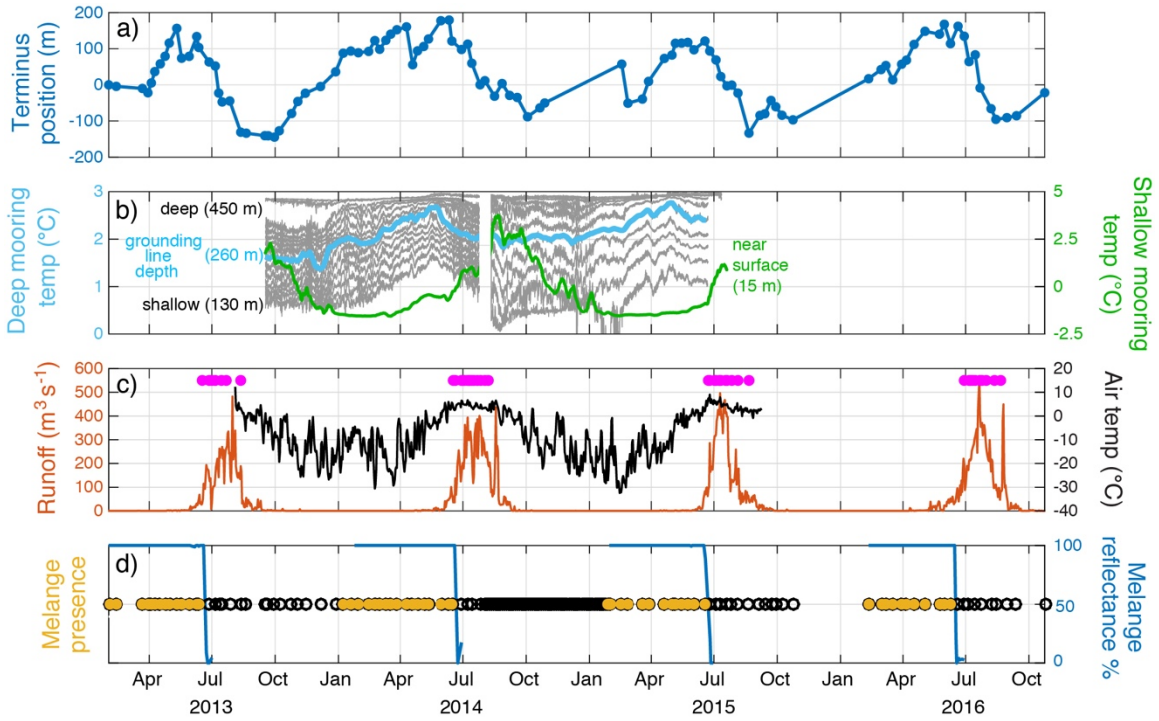

Figure 3.2. Kangerlussuup Sermia (KAS) time series illustrating temporal relationships between terminus position changes and potential forcing mechanisms: a) mean terminus position; b) Fjord ocean temperatures from the deep KSD mooring (blue/grey) and shallow KSP mooring (green) identified in Fig. 1b. Light blue line represents the mean weekly temperature at the sensor closest to the grounding line depth; c) daily RACMO2.3p2 runoff estimates for the KAS catchment (red), daily maximum air temperature (black) and turbid subglacial plume observations (pink circles are plotted at an arbitrary y-axis position); d) confirmation of mélange presence (yellow circles) and all observations (empty black circles) from satellite imagery and time-lapse cameras plotted at an arbitrary y-axis position, and MODIS-based mélange reflectance coverage as a percentage of the proglacial fjord sample area (blue) from Fig. 1b. We present similar plots for all glaciers in the Supporting Information.

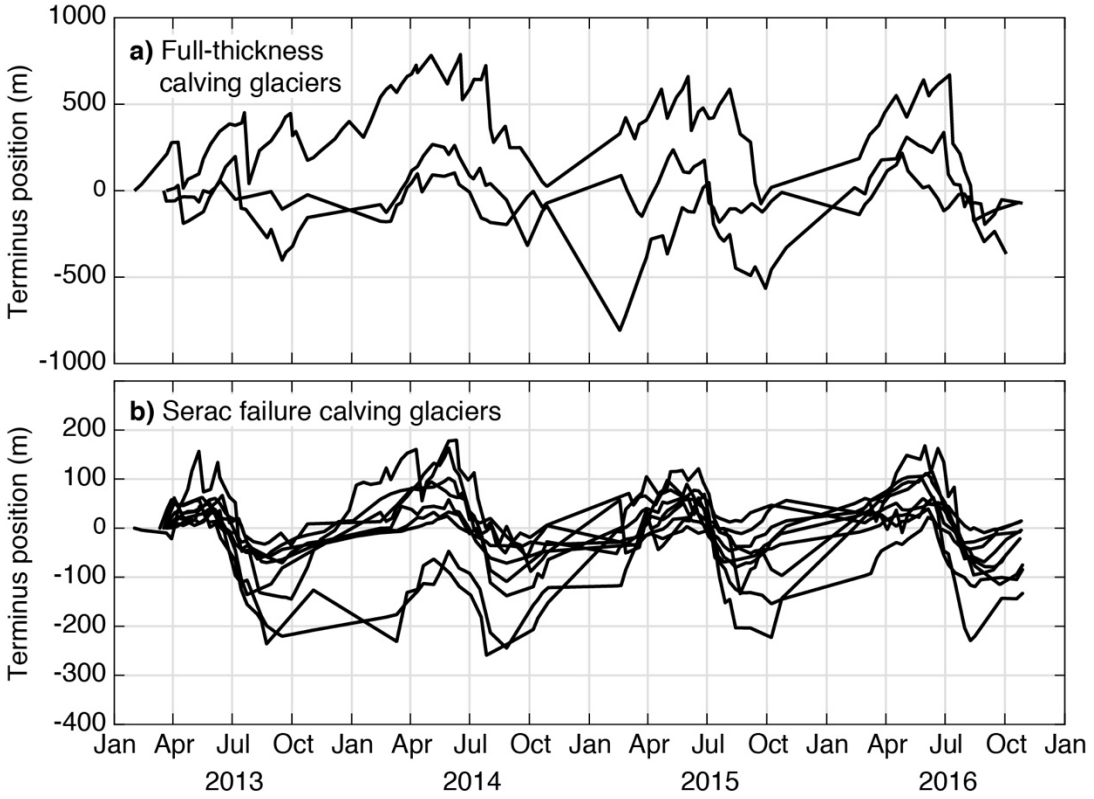

Figure 3.3. Detrended, mean terminus position records for a) full-thickness calving glaciers with large magnitude and variable seasonal cycles and b) serac failure calving glaciers with smaller magnitude and smooth seasonal cycles. Note difference in y-axis scale between subplots.

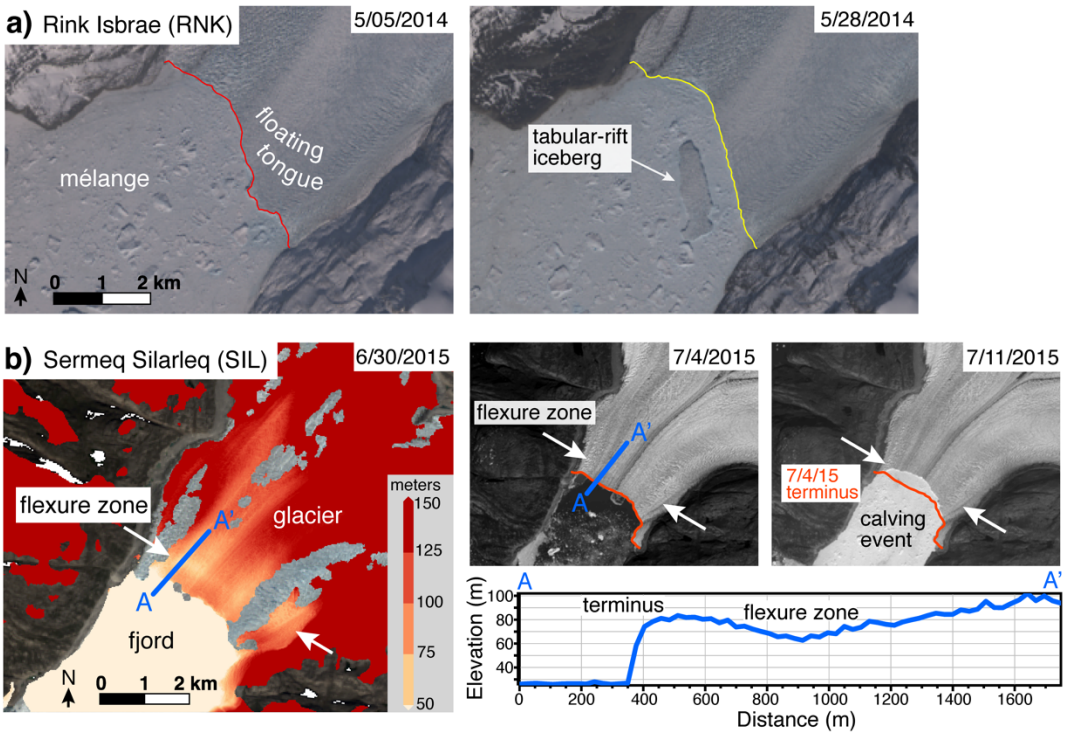

Figure 3.4. a) Landsat images showing formation of tabular-rift calving at RNK; b) DEM strip (ArcticDEM release 6 from Polar Geospatial Data Center) over SIL showing broad flexure zone forming ~250 m up-glacier from the terminus on 6/30/15. Transect A-A' shows a trough in the flexure zone that sits ~20 m below the terminus height, indicating the terminus region is at flotation and the presence of strong, upward lifting buoyancy forcing. Subsequent Landsat images show terminus conditions before and after a large, full-thickness capsizing slab calving event within the flexure zone. White arrows indicate approximate across-glacier location of flexure trough.

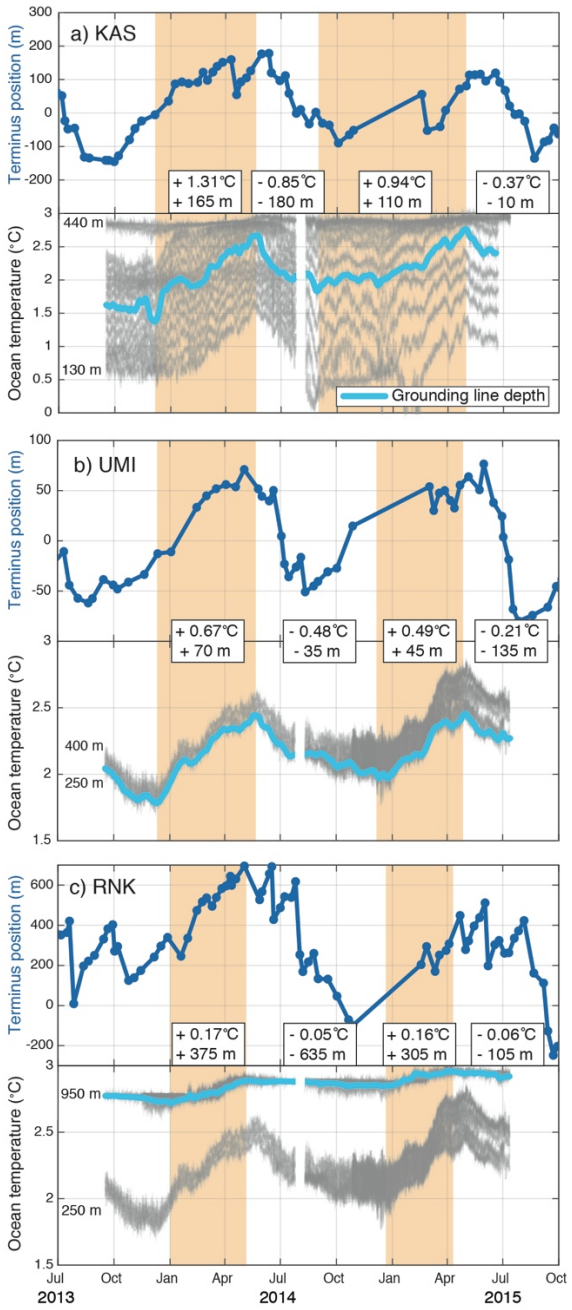

Figure 3.5. Time series illustrating temporal relationships between terminus positions and moored records of ocean temperature at a) KAS from the KSD mooring, b) UMI from the RKS mooring and c) RNK from both RKD and RKS moorings. Light blue solid lines represent observed ocean temperature corresponding to the grounding line depth for each glacier. Grey lines represent temperature records at all observed depths. Orange boxes represent periods of inferred ocean warming in each fjord. Annotated boxes note ocean temperature change at the grounding line and terminus position change during periods of seasonal warming and cooling.

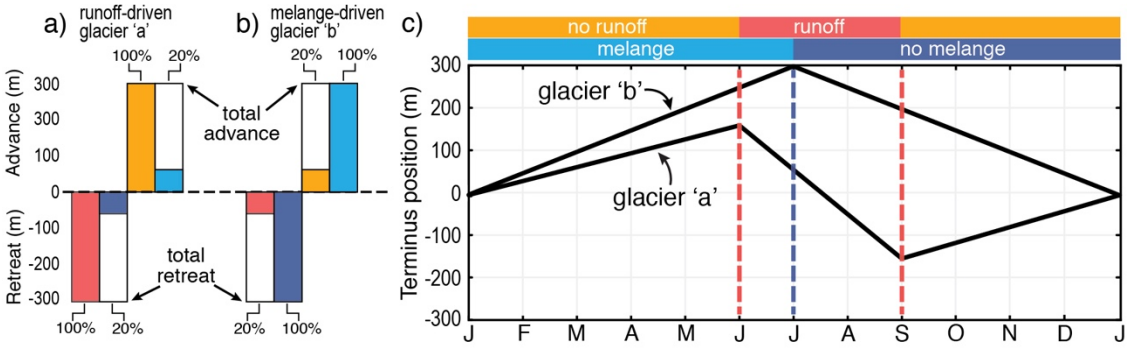

Figure 3.6. Comparison of total terminus advance/retreat in relation to cumulative terminus position change coincident with the presence/absence of runoff/mélange for two hypothetical terminus curves: a) glacier 'a' the runoff-driven case and b) glacier 'b' the mélange-driven case. Bar graphs show amounts and percent of each seasonal cycle captured by environmental forcing mechanisms. c) Corresponding hypothetical terminus position time series for the two glacier types. Seasonal cycles are normalized by initial January positions.

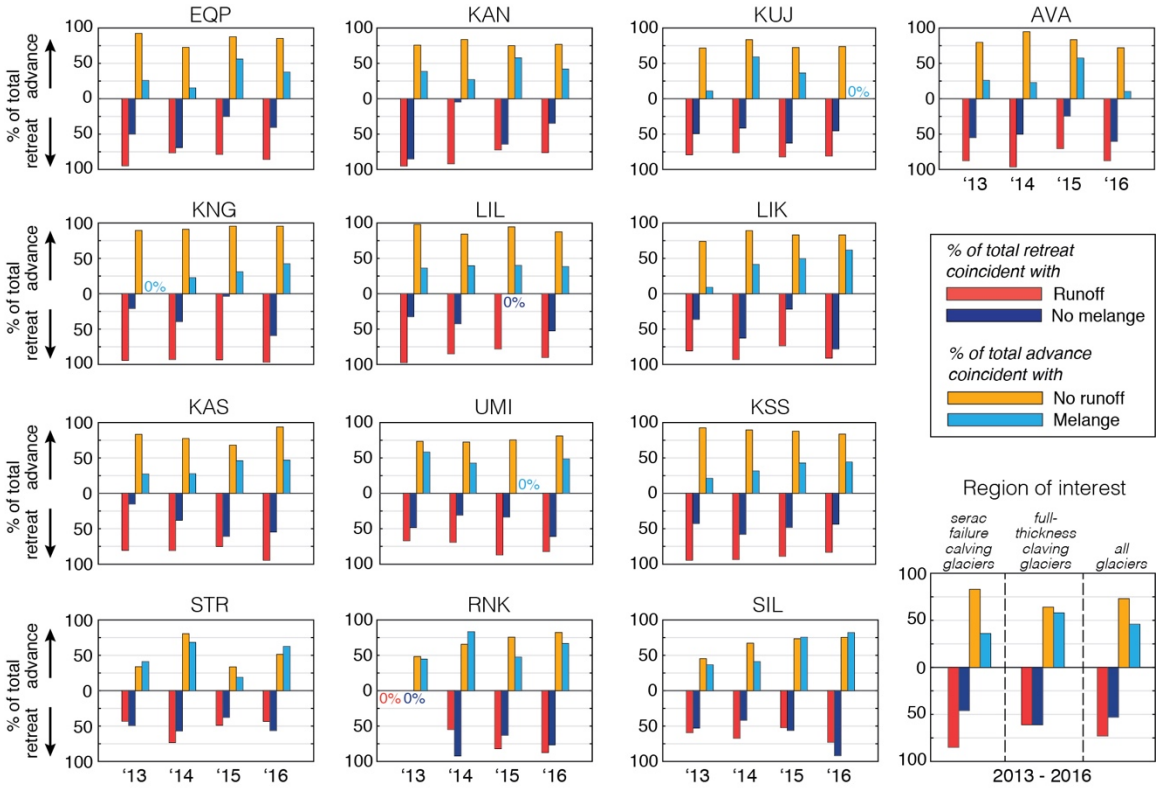

Figure 3.7. Histograms depicting the percentage of total seasonal terminus advance coincident with no runoff/mélange and retreat coincident with runoff/no mélange at each glacier between 2013-2016. Panel at bottom right shows aggregated percentages for serac failure calving glaciers, full-thickness calving glaciers and all glaciers in the study area.

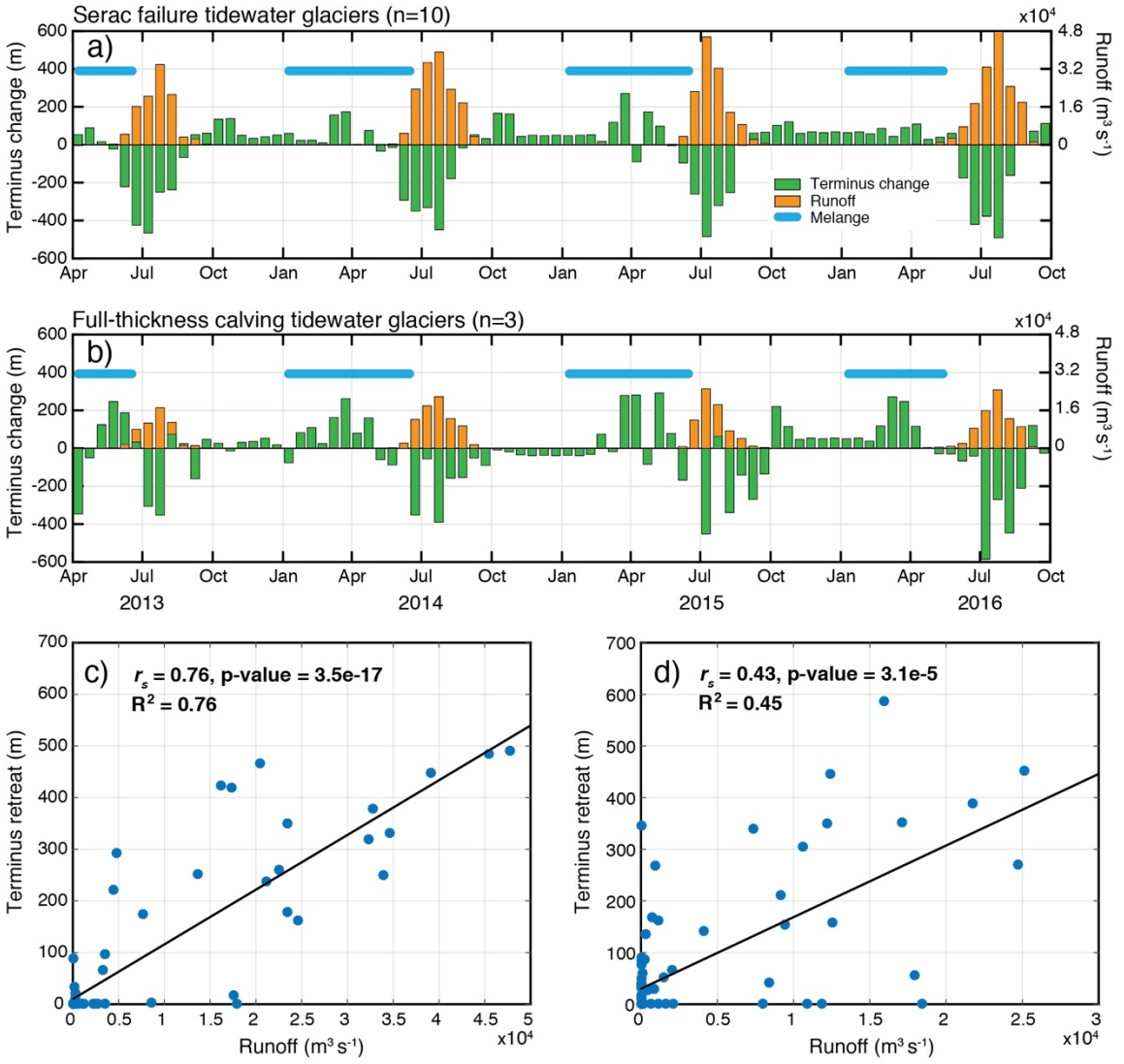

Figure 3.8. a, b) Time series of terminus change (green bars) and RACMO2.3p2 runoff (orange bars) integrated over two week periods for two glacier groups classified by their dominant calving style (serac failure and full thickness, capsizing slab/tabular rift). Approximate presence of seasonal mélange is shown with blue bars. Corresponding linear regressions between runoff and terminus retreat for c) serac failure glaciers and d) full-thickness calving glaciers from data in a) and b). r_s statistics and associated p-values represent calculated Spearman's rank coefficients for each glacier type.

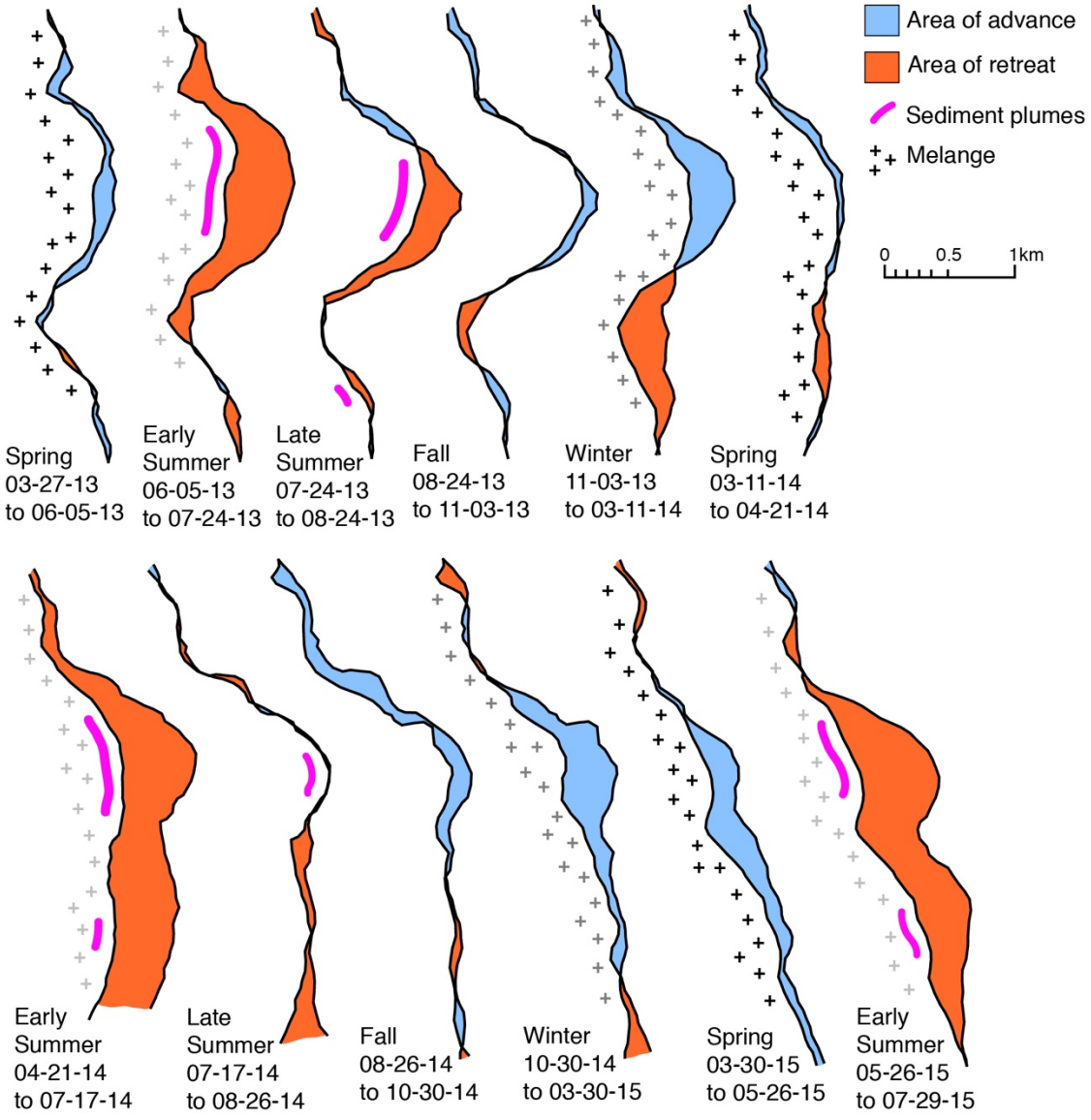

Figure 3.9. Integrated terminus changes at EQP showing areas of seasonal advance (blue) and retreat (orange) in relation to forcing mechanisms. Approximate extents of turbid subglacial plumes along the terminus are shown in pink. Crosses indicate mélange presence with lighter crosses signifying that mélange was not present for the entirety of the given time period.

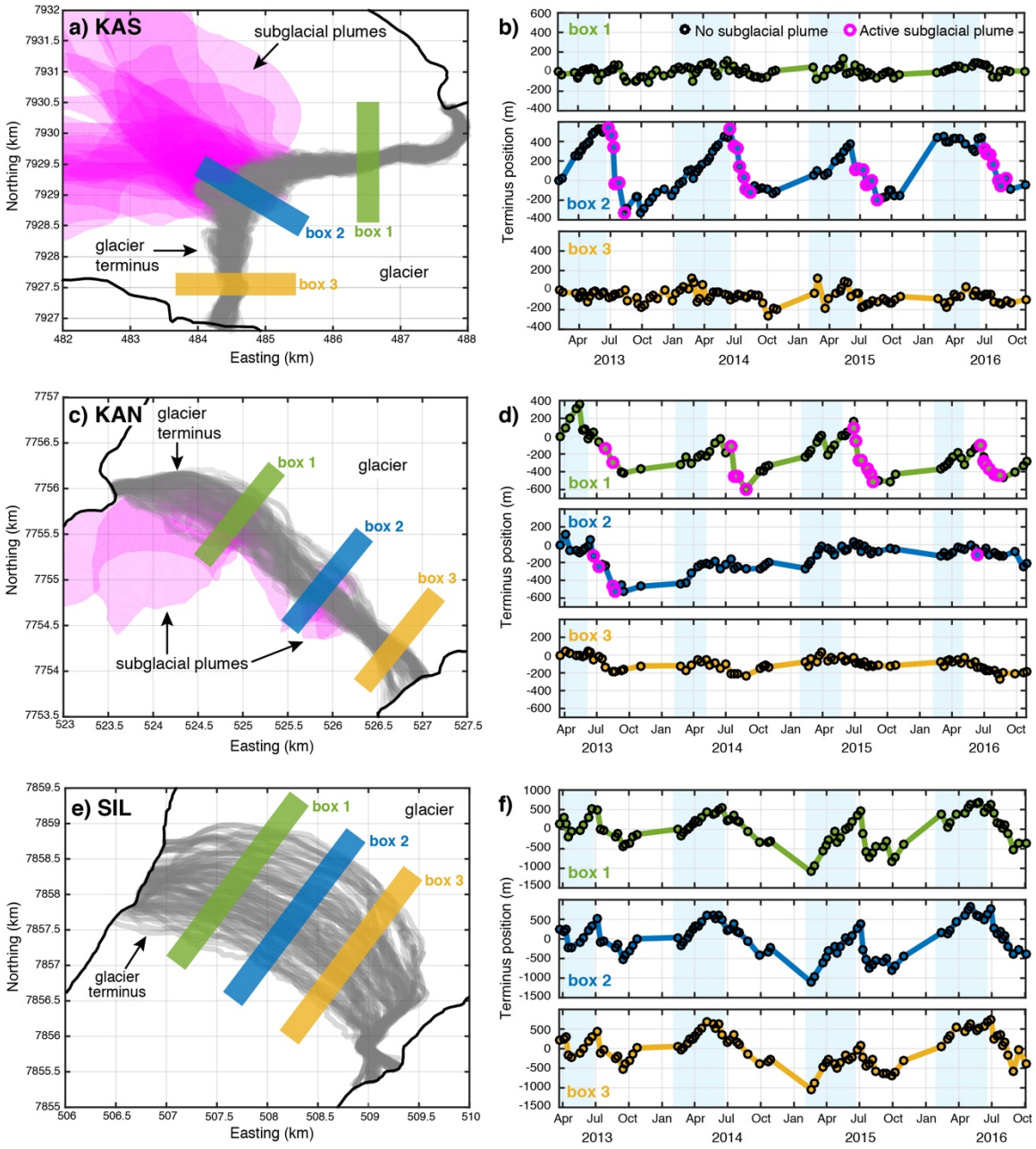

Figure 3.10. Relationship between terminus positions and turbid subglacial plumes at a) KAS and c) KAN and mélange at e) SIL. Map-views show terminus positions (gray lines), turbid subglacial plume surface expressions between 2013-2016 (pink regions), and terminus sampling boxes (1-3). Time-series show terminus positions evaluated within each sampling box for b) KAS, d) KAN and f) SIL. The presence of subglacial plumes (pink dots) and mélange (blue shaded bars) are provided when they overlap a sampling box.

3.8. Supporting Information

Table 3.1. Timing and magnitude of Rink Isbrae (RNK) retreat (calving) events between 2013-2016 greater than 50m. Start and end dates denote bounding image dates from terminus position record. Initial, absolute retreat magnitudes may not be resolved within resolution of the terminus time series.

Glacier	Start Date	End Date	Mean terminus retreat (m)
Rink Isbrae (RNK)	4/9/13	4/17/13	265
Rink Isbrae (RNK)	7/20/13	7/27/13	410
Rink Isbrae (RNK)	9/29/13	10/2/13	130
Rink Isbrae (RNK)	10/7/13	10/25/13	170
Rink Isbrae (RNK)	12/28/13	1/19/14	90
Rink Isbrae (RNK)	5/3/14	5/28/14	165
Rink Isbrae (RNK)	6/17/14	6/20/14	260
Rink Isbrae (RNK)	7/26/14	8/2/14	365
Rink Isbrae (RNK)	8/2/14	8/7/14	80
Rink Isbrae (RNK)	8/25/14	9/1/14	125
Rink Isbrae (RNK)	9/17/14	10/2/14	80
Rink Isbrae (RNK)	10/2/14	10/21/14	115
Rink Isbrae (RNK)	2/26/15	3/12/15	125
Rink Isbrae (RNK)	4/22/15	5/1/15	170
Rink Isbrae (RNK)	6/2/15	6/7/15	310
Rink Isbrae (RNK)	8/5/15	8/21/15	260
Rink Isbrae (RNK)	9/6/15	9/13/15	235
Rink Isbrae (RNK)	9/13/15	9/22/15	120
Rink Isbrae (RNK)	4/17/16	5/3/16	125
Rink Isbrae (RNK)	5/29/16	6/6/16	90
Rink Isbrae (RNK)	7/8/16	7/13/16	340
Rink Isbrae (RNK)	7/24/16	7/31/16	95
Rink Isbrae (RNK)	7/31/16	8/9/16	85
Rink Isbrae (RNK)	8/9/16	8/14/16	205

Table 3.2. Timing and magnitude of Store Gletscher (STR) retreat (calving) events between 2013-2016 greater than 50m. Start and end dates denote bounding image dates from terminus position record. Initial, absolute retreat magnitudes may not be resolved within resolution of the terminus time series.

Glacier	Start Date	End Date	Mean terminus retreat (m)
Store Gletsjer (STR)	3/18/13	3/22/13	60
Store Gletsjer (STR)	6/13/13	7/6/13	105
Store Gletsjer (STR)	8/20/13	9/16/13	100
Store Gletsjer (STR)	10/25/13	2/14/14	155
Store Gletsjer (STR)	4/12/14	4/19/14	105
Store Gletsjer (STR)	6/8/14	6/15/14	65
Store Gletsjer (STR)	7/1/14	7/18/14	150
Store Gletsjer (STR)	10/7/14	10/21/14	90
Store Gletsjer (STR)	2/19/15	2/28/15	85
Store Gletsjer (STR)	2/28/15	3/15/15	125
Store Gletsjer (STR)	5/10/15	5/26/15	130
Store Gletsjer (STR)	6/27/15	7/4/15	245
Store Gletsjer (STR)	7/11/15	7/20/15	85
Store Gletsjer (STR)	10/24/15	2/20/16	130
Store Gletsjer (STR)	4/26/16	5/5/16	100
Store Gletsjer (STR)	5/5/16	5/28/16	100
Store Gletsjer (STR)	6/6/16	6/20/16	75
Store Gletsjer (STR)	6/20/16	6/29/16	70
Store Gletsjer (STR)	7/31/16	8/9/16	55
Store Gletsjer (STR)	8/25/16	8/31/16	120

Table 3.3. Timing and magnitude of Sermeq Silarleq (SIL) retreat (calving) events between 2013-2016 greater than 50m. Start and end dates denote bounding image dates from terminus position record. Initial, absolute retreat magnitudes may not be resolved within resolution of the terminus time series.

Glacier	Start Date	End Date	Mean terminus retreat (m)
Sermeq Silarleq (SIL)	4/9/13	4/17/13	220
Sermeq Silarleq (SIL)	7/6/13	7/15/13	300
Sermeq Silarleq (SIL)	7/22/13	8/24/13	165
Sermeq Silarleq (SIL)	8/30/13	9/15/13	180
Sermeq Silarleq (SIL)	6/8/14	6/15/14	65
Sermeq Silarleq (SIL)	6/15/14	7/1/14	110
Sermeq Silarleq (SIL)	7/17/14	7/26/14	100
Sermeq Silarleq (SIL)	8/2/14	8/25/14	95
Sermeq Silarleq (SIL)	8/27/14	9/15/14	265
Sermeq Silarleq (SIL)	10/28/14	2/17/15	720
Sermeq Silarleq (SIL)	4/24/15	5/1/15	105
Sermeq Silarleq (SIL)	7/4/15	7/6/15	240
Sermeq Silarleq (SIL)	7/11/15	7/26/15	70
Sermeq Silarleq (SIL)	8/5/15	8/23/15	195
Sermeq Silarleq (SIL)	9/13/15	9/29/15	125
Sermeq Silarleq (SIL)	6/29/16	7/6/16	240
Sermeq Silarleq (SIL)	7/6/16	7/15/16	55
Sermeq Silarleq (SIL)	7/24/16	7/31/16	125
Sermeq Silarleq (SIL)	8/7/16	8/16/16	145
Sermeq Silarleq (SIL)	8/16/16	8/30/16	115
Sermeq Silarleq (SIL)	9/15/16	10/3/16	130

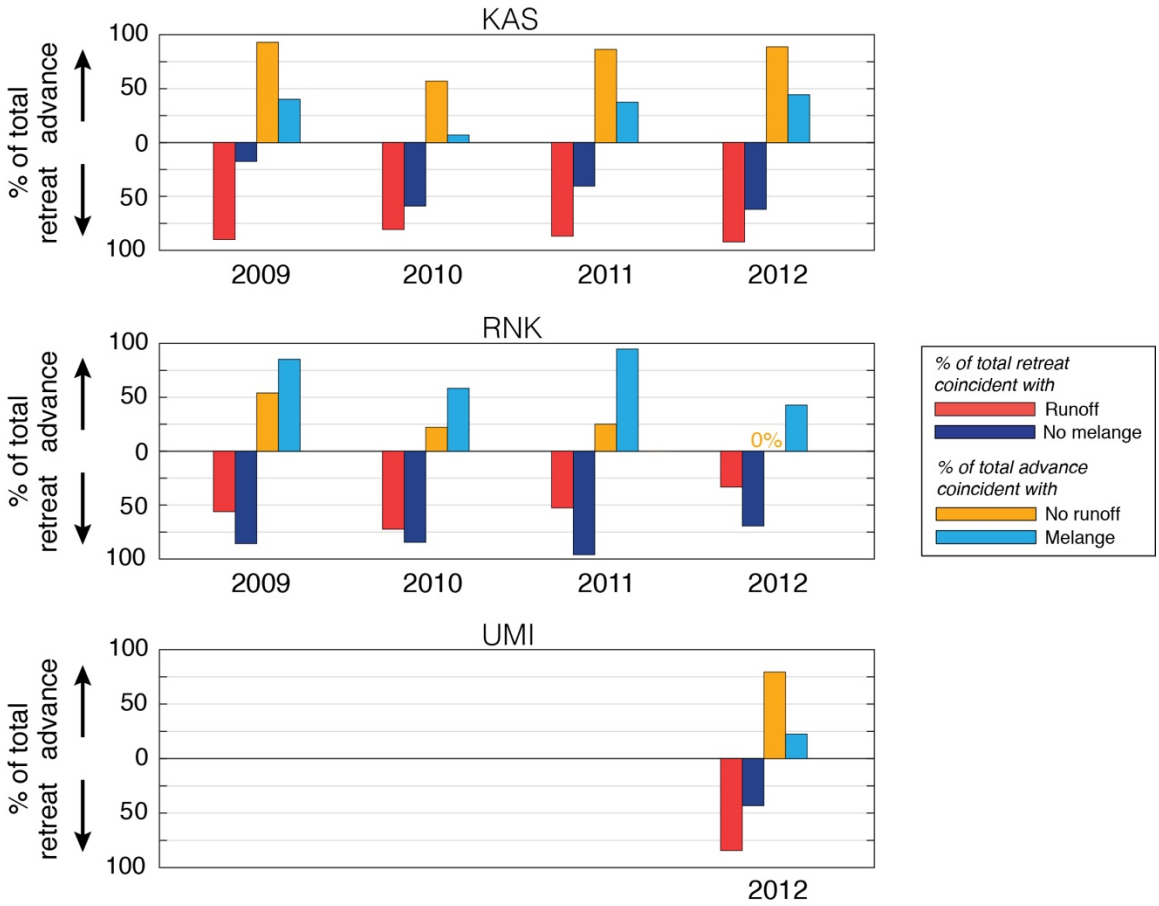

Figure 3.11. Extended histogram analyses for KAS, RNK and UMI. Histograms depict the percentage of total seasonal terminus advance coincident with no runoff/mélange and retreat coincident with runoff/no mélange.

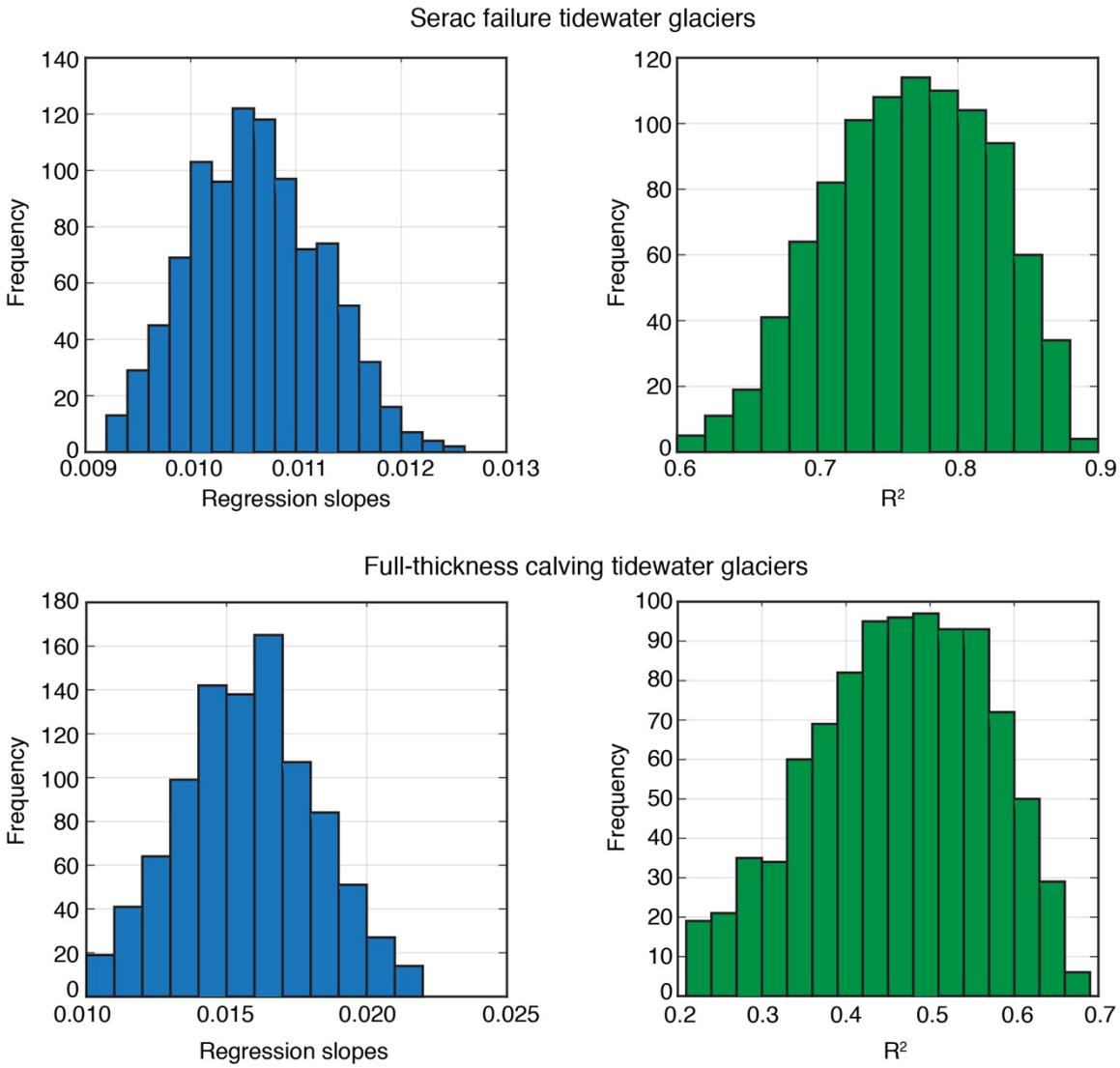

Figure 3.12. 95% confidence intervals for and linear regression slopes and coefficients of determination from bootstrap analysis evaluating the positive, scaled relationship between runoff and terminus retreat.

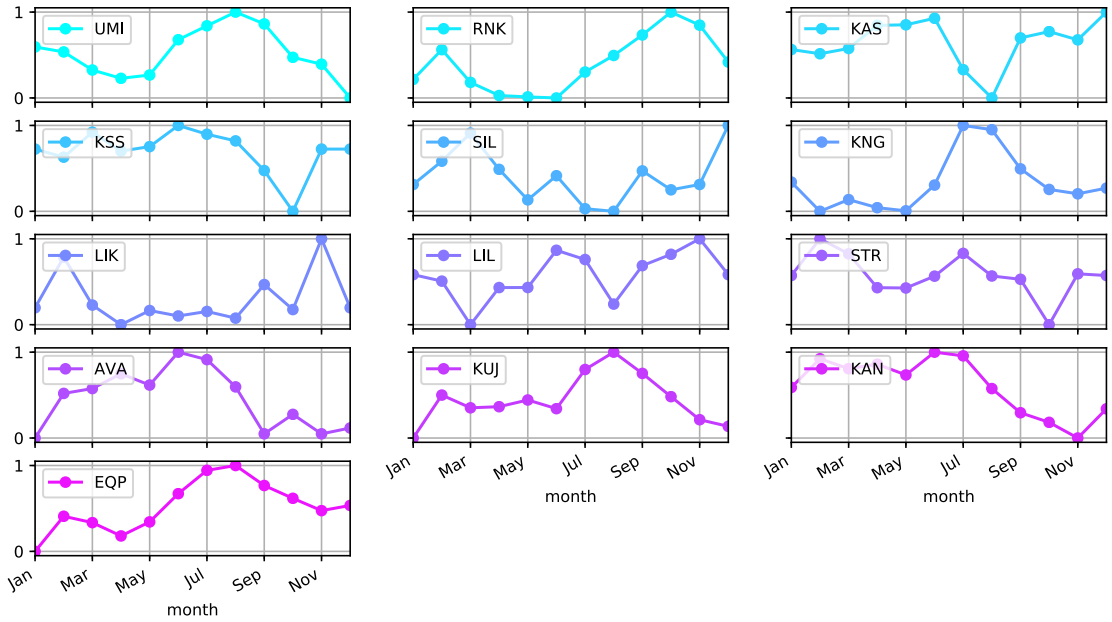

Figure 3.13. Minimum-maximum normalized, average seasonal terminus velocities for each glacier between 2013-2016. To describe seasonal cycles, we calculate monthly deviations from the mean annual velocity for each year. We then average monthly deviations for each glacier and use these values to produce a time series of normalized seasonal terminus velocities.

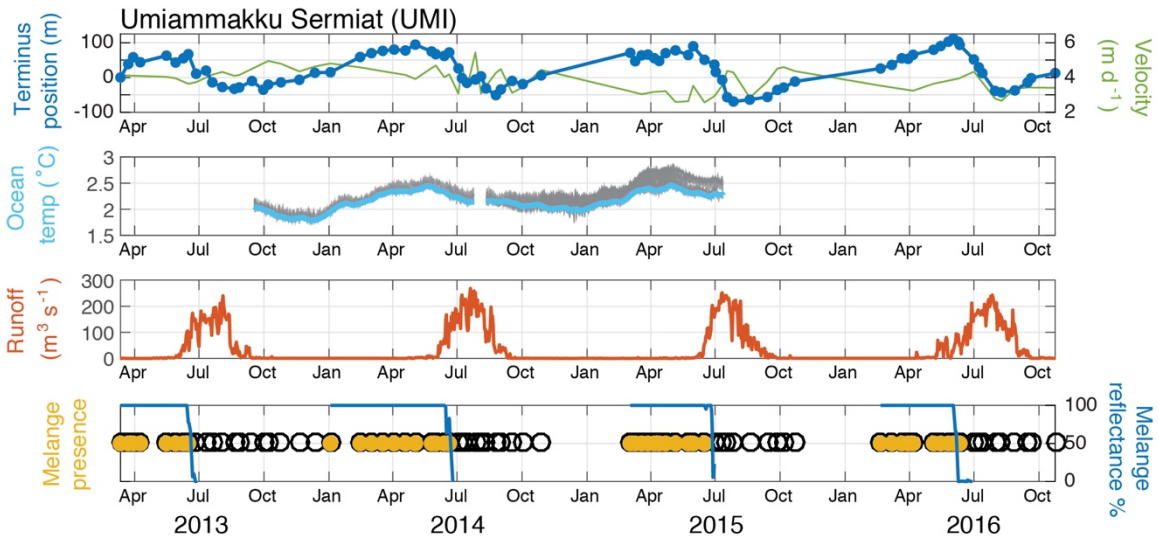

Figure 3.14. Umiammakku Sermiat (UMI) time series illustrating temporal relationships between terminus position changes and potential forcing mechanisms: a) mean terminus position and velocity; b) fjord ocean temperatures are from the RKS mooring (blue/grey) identified in Figure 3.1a. Light blue line represents the mean weekly mooring temperature from the sensor closest to grounding line depth; c) daily RACMO2.3p2 runoff estimates for the UMI catchment (red); d) confirmation of mélange presence (yellow circles) and all observations (empty black circles) from satellite imagery and time-lapse cameras plotted at an arbitrary y-axis position; and MODIS-based mélange reflectance coverage as a percentage of the total proglacial fjord sample polygon area (blue).

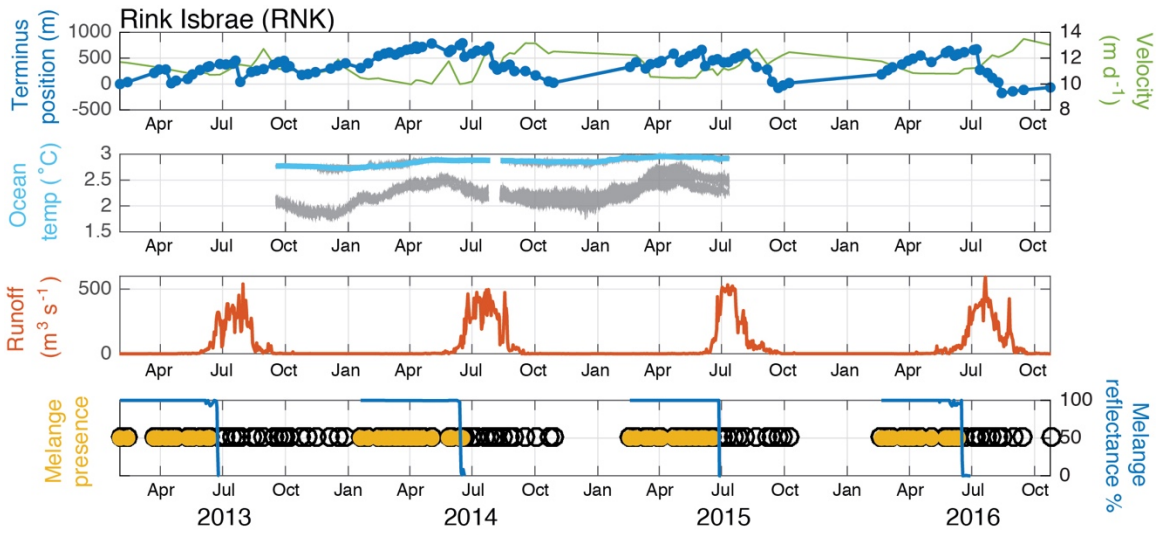

Figure 3.15. Rink Isbrae (RNK) time series. Same as above. Fjord ocean temperatures are from RKD and RKS moorings (blue/grey) identified in Figure 3.1a.

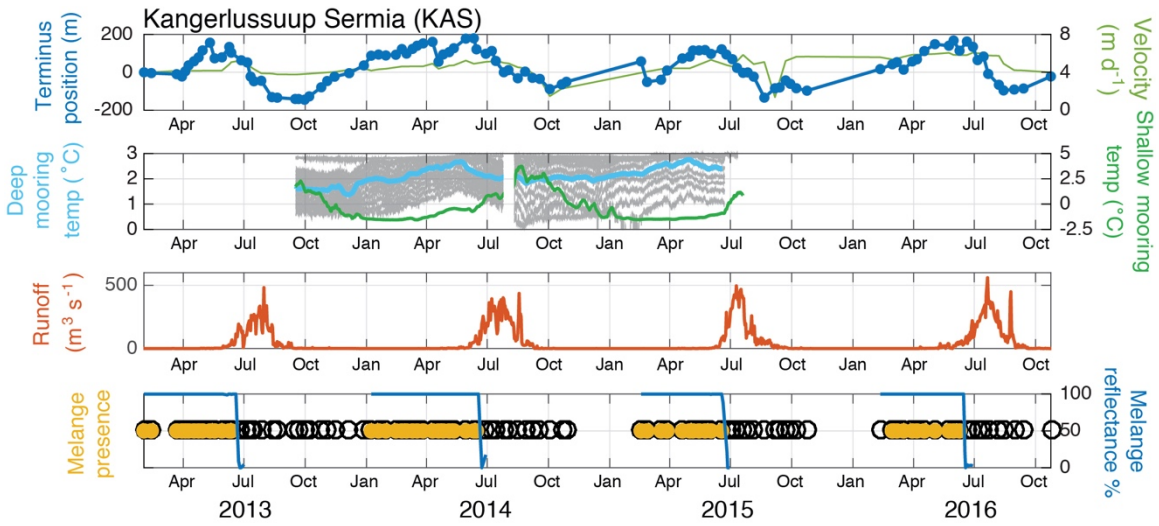

Figure 3.16. Kangerlussuup Sermia (KAS) time series. Same as above. Fjord ocean temperatures from KSD (blue/grey) and KSP (dark green) moorings identified in Fig. 1b.

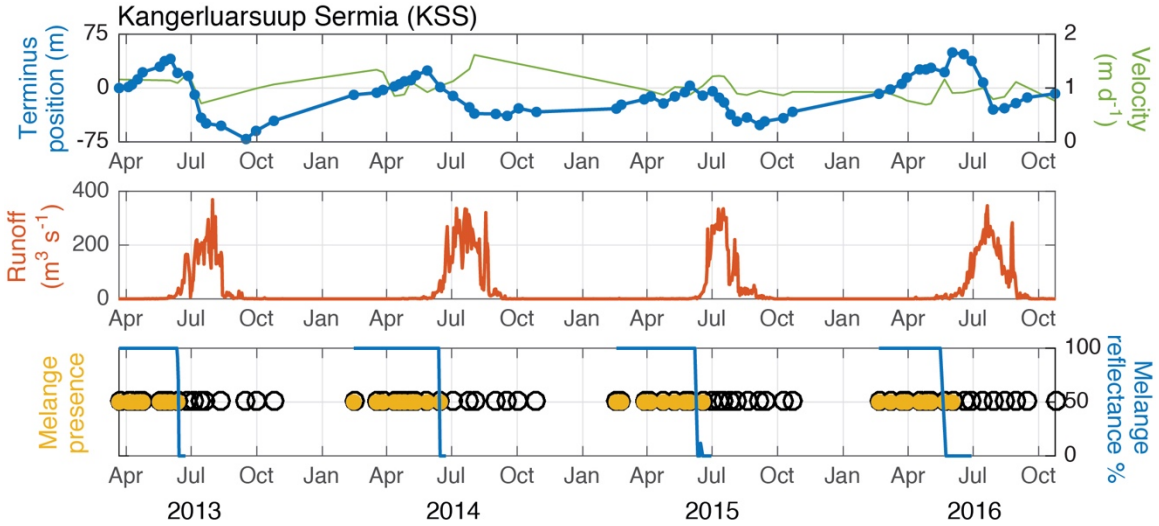

Figure 3.17. Kangerluarsuup Sermia (KSS) time series. Same as above. No direct ocean observations.

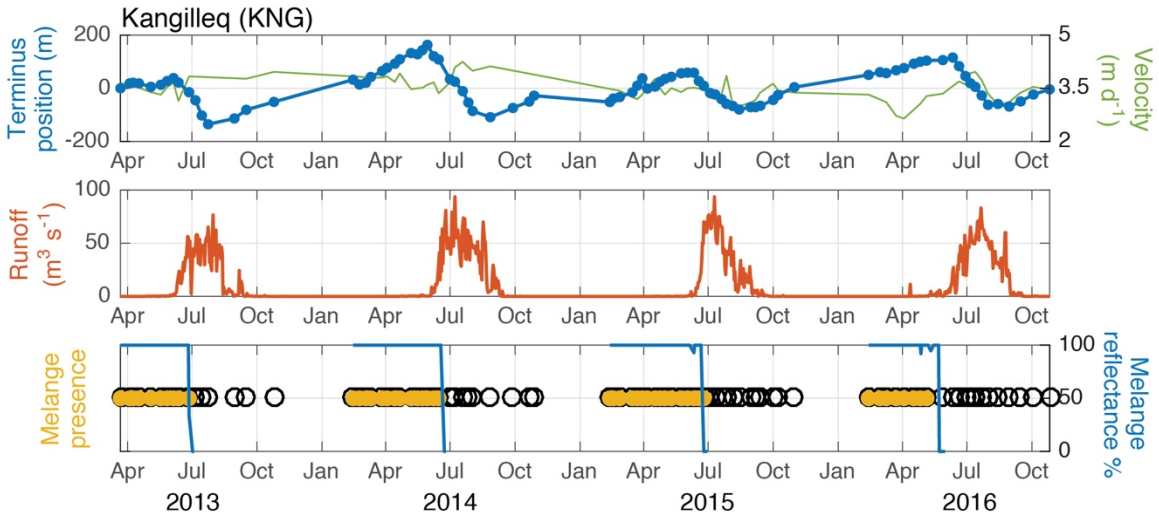

Figure 3.18. Kangilleq (KNG) time series. Same as above. No direct ocean observations.

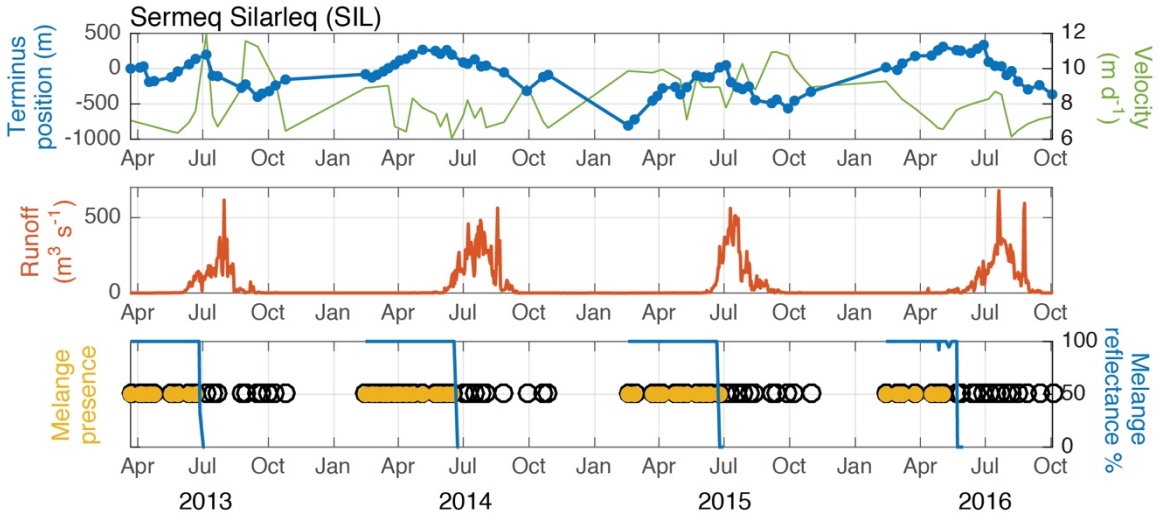

Figure 3.19. Sermeq Silarleq (SIL) time series. Same as above. No direct ocean observations.

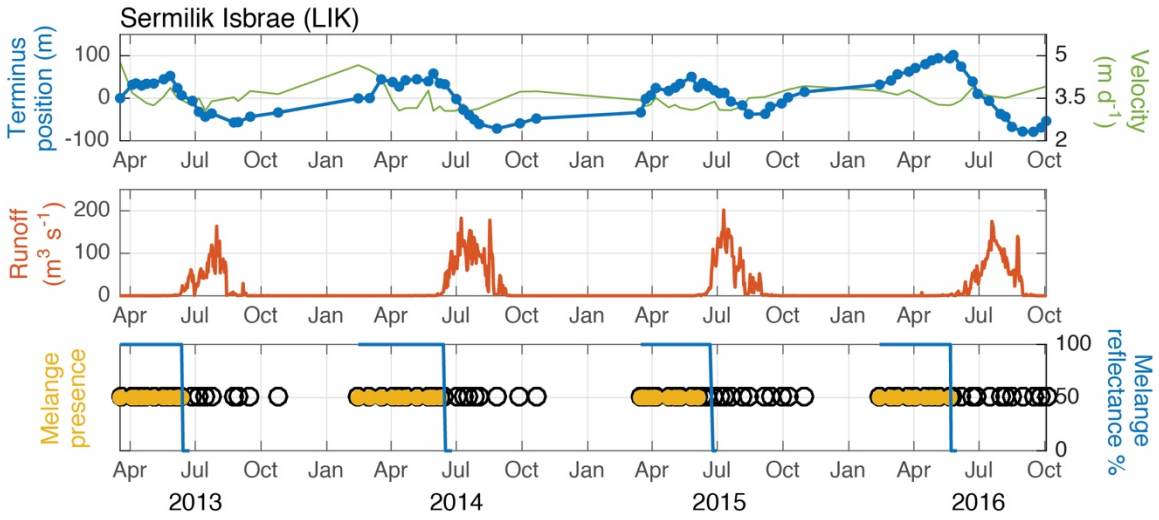

Figure 3.20. Sermilik Isbrae (LIK) time series. Same as above. No direct ocean observations.

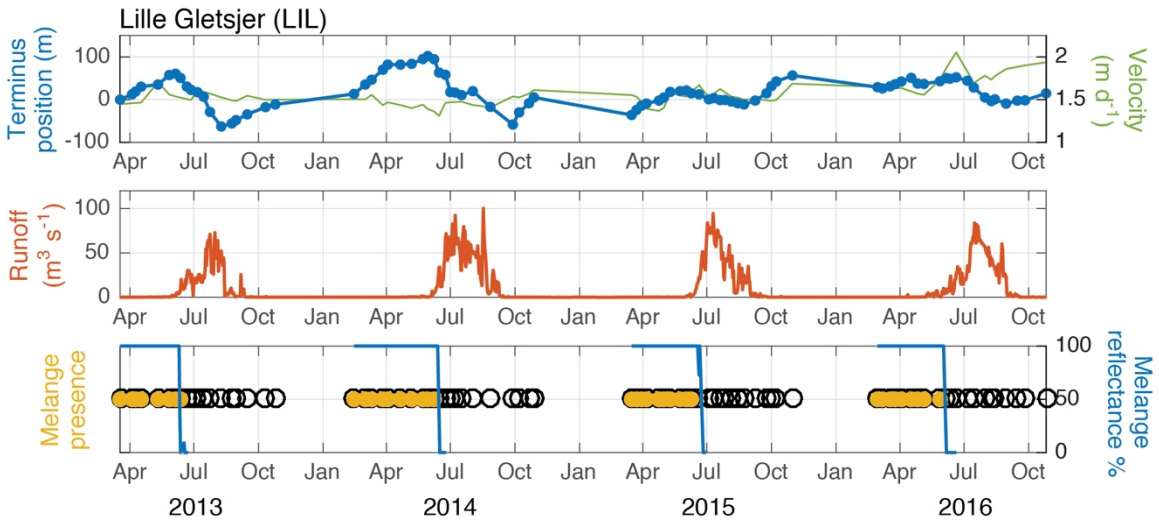

Figure 3.21. Lille Gletsjer (LIL) time series. Same as above. No direct ocean observations.

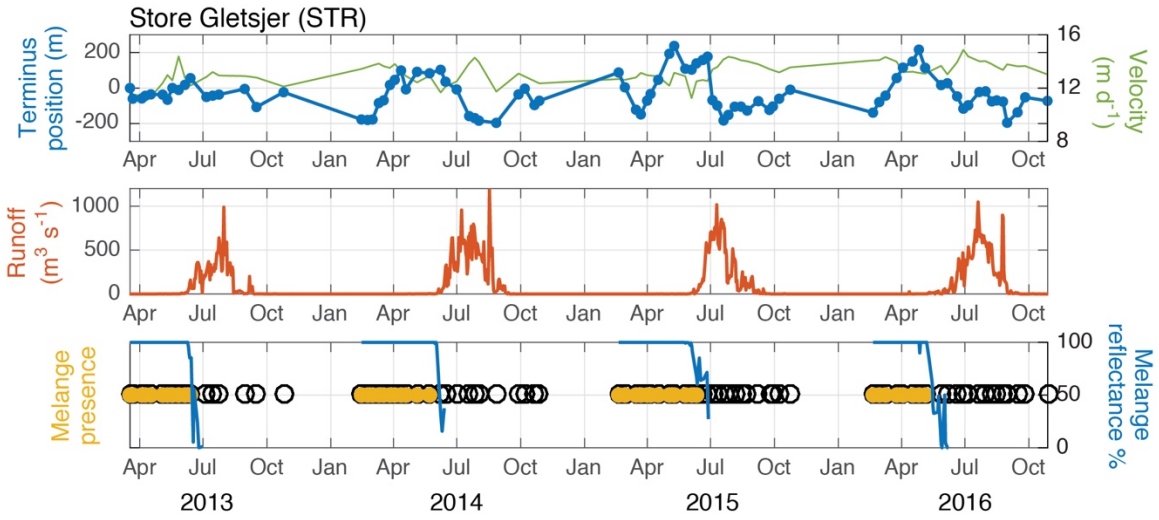

Figure 3.22. Store Gletsjer (STR) time series. Same as above. No direct ocean observations.

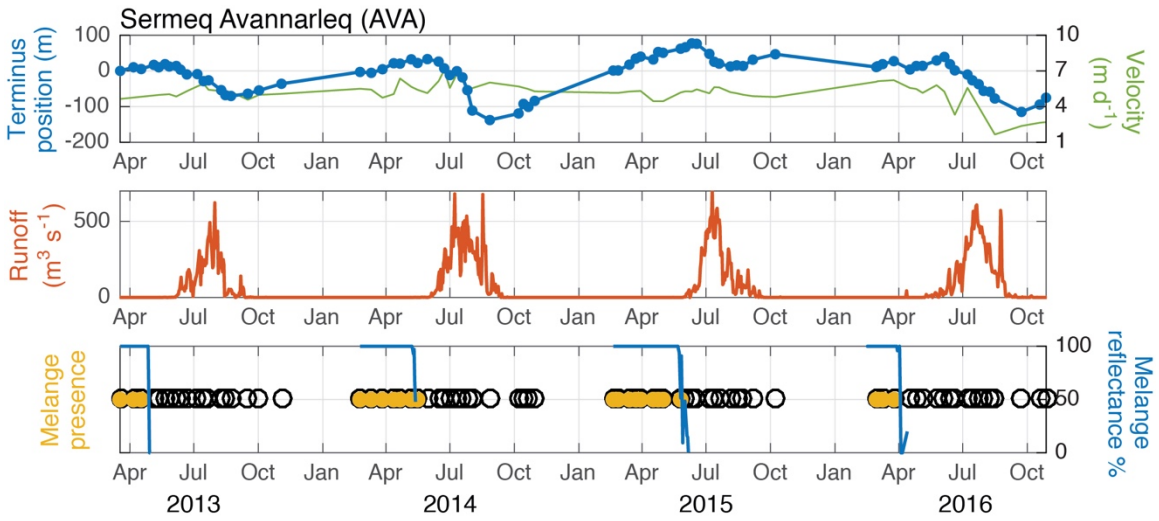

Figure 3.23. Sermeq Avannarleq (AVA) time series. Same as above. No direct ocean observations.

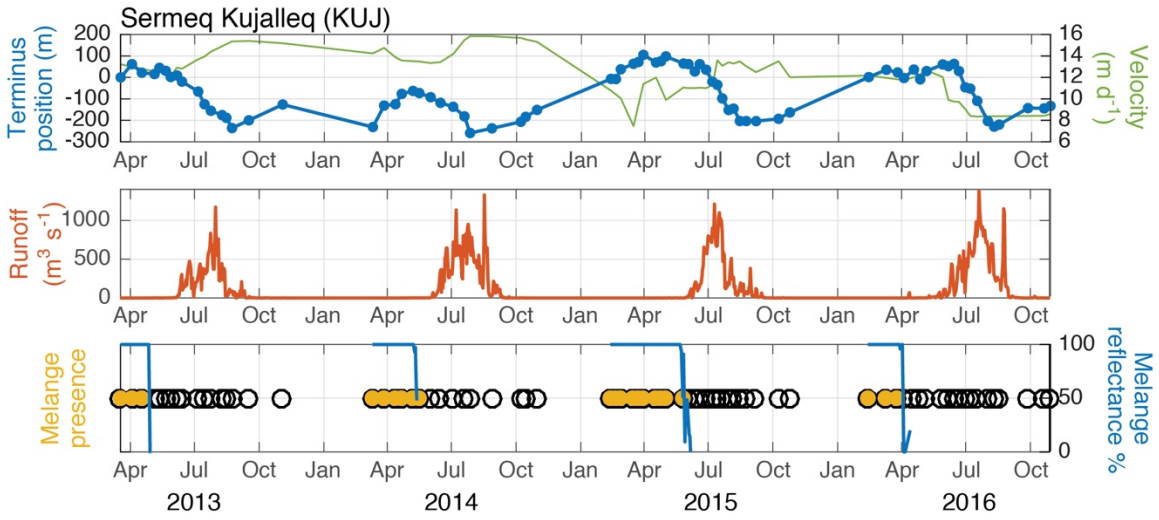

Figure 3.24. Sermeq Kujalleq (KUJ) time series. Same as above. No direct ocean observations.

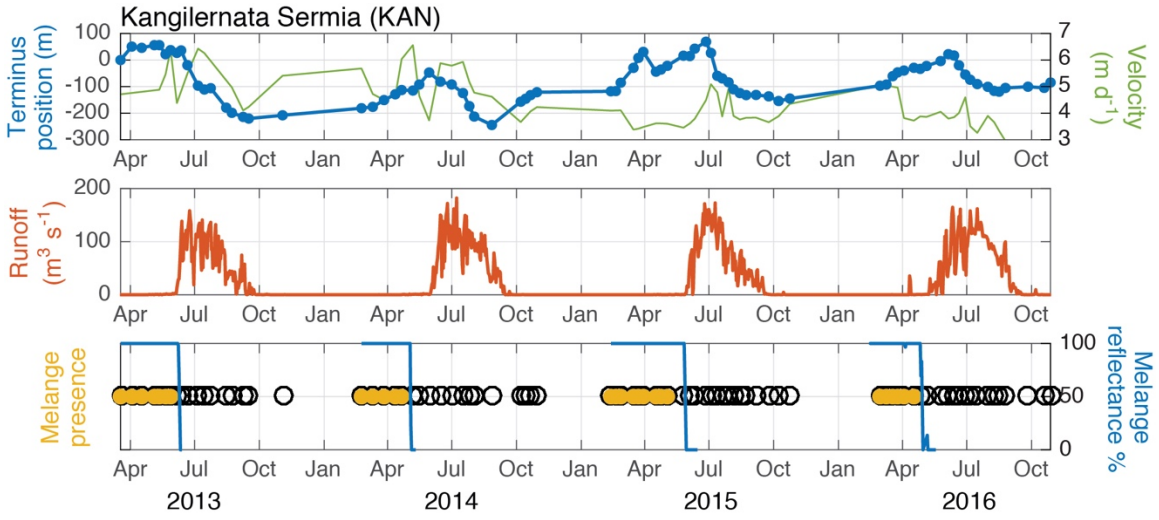

Figure 3.25. Kangilernata Sermia (KAN) time series. Same as above. No direct ocean observations.

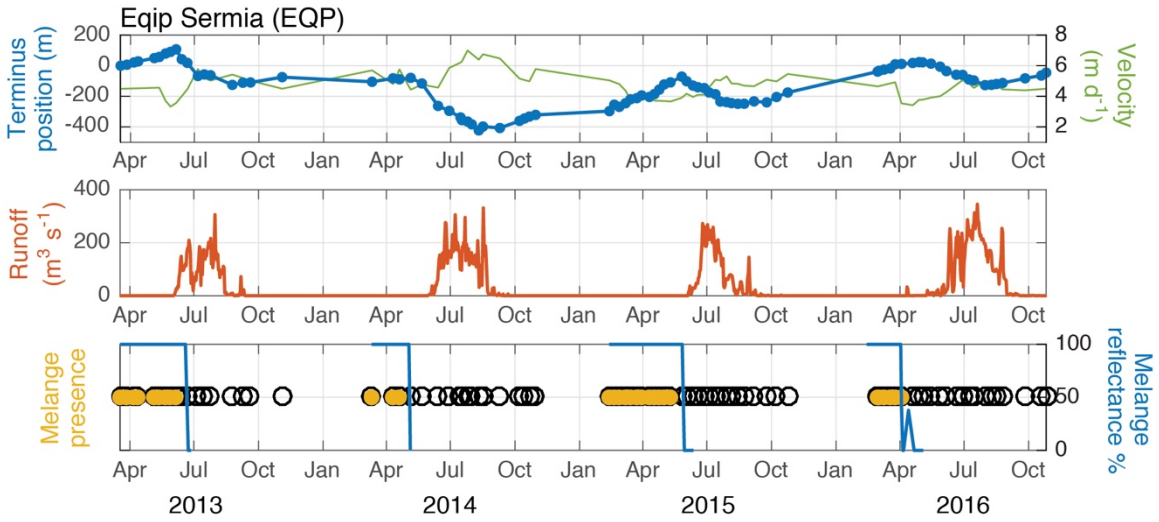

Figure 3.26. Eqip Sermia (EQP) time series. Same as above. No direct ocean observations.

Chapter 4. Diverse submarine terminus morphologies reveal insights into frontal ablation processes

4.1. Introduction

Greenlandic glaciers currently lose mass most rapidly where they terminate in the ocean [*Csatho et al.*, 2014; *Enderlin et al.*, 2014; *Felikson et al.*, 2017]. This pattern of mass loss is driven by enhanced frontal ablation, a combination of submarine melting and iceberg calving, due, in part, to recent increases in ocean thermal forcing and meltwater production at the Greenland Ice Sheet margin [*O'Leary and Christoffersen*, 2011; *Streneo and Heimbach*, 2013]. Increased frontal ablation can trigger terminus retreat, faster glacier flow and, in turn, rapid contributions to sea level rise [*Nick et al.*, 2009; *McFadden et al.*, 2011; *Seale et al*., 2011].

However, reproducing tidewater glacier terminus retreat records in ice sheet models remains elusive due to uncertainty in physical processes controlling frontal ablation rates and the absence of several observational datasets at the terminus [*Truffer and Motyka*, 2016]. Specifically, we lack direct imaging and interpretation of the submarine terminus face and constraints on the magnitude of subglacial discharge fluxes emerging at the grounding line. While submarine melting can drive significant ice loss at the glacier front [*Rignot et al*., 2010; *Motyka et al*., 2011; *Fried et al*., 2015], numerical simulations of subglacial plumes are missing first-order observations of outlet geometries, including their spatial distribution, width, depth and discharge flux. It may be possible to constrain these variables and understand other changes at the terminus

through examination of submarine terminus morphology. Ultimately, the interplay between submarine terminus morphologies and frontal ablation processes, such as calving, submarine melting and subglacial discharge, are largely unknown.

In this paper, we attempt to resolve these issues through the use of multibeam echo sonar data providing a detailed survey of submarine terminus morphologies across Kangerlussuup Sermia (KAS), a tidewater glacier in central West Greenland (71°27'N, 51°20'W; Figure 4.1). We identify and map previously unidentified characteristic morphologies that populate distinct terminus regions. We then use these morphologies to infer ablation processes acting at the terminus and their spatial distribution across the glacier front. Finally, we pair observations of the submarine terminus with a plume model [*Jenkins*, 2011; *Jackson et al.*, 2017] to estimate discharge fluxes and buoyant plume behavior within identified subglacial plume outlets.

4.2. Methods

4.2.1. Quantifying submarine terminus morphologies

To image terminus morphologies, we surveyed the submarine portion of the KAS terminus using a pole-mounted RESON SeaBat 7111 Multibeam Sonar System on 21 and 23 July 2013. The multibeam survey operated at 100 kHz with 301 equi-angle beams and we maximized vertical imaging of the terminus face by inserting a 15° wedge into the multibeam sonar system mount. During the survey we constrained the fjord sound velocity profile using in situ conductivity-temperature-depth (CTD) casts. Multibeam positioning data were acquired using an Applanix POS/MV model 320 positioning and

orientation system. We used Caris software to merge multibeam returns with the positioning and orientation data and the resulting point cloud data represent individual measurements of the terminus location. Multibeam return depths are referenced to mean sea level. The multibeam point cloud is accurate to within 3-5 m horizontally and 15-25 cm radially from the ship, as reported by the POS/MV and RESON systems, respectively.

In order to quantify and inventory submarine terminus face shapes across the width of the glacier, we binned the multibeam point cloud into 190 cross sections, each oriented locally normal to the terminus face (Figure 4.1). The mean spacing between cross sections was 27 m. At each cross section, we extracted all multibeam returns within 5 m on either side of the cross-section line and projected them onto a 2D cross section plane (e.g. Figure 4.2c), representing their vertical depth (z-coordinate) and distance along the cross section (x-coordinate). Because the density of multibeam returns is not consistent across the terminus, we extracted returns within 10 m of the cross section line in locations where the multibeam point cloud was less dense, in order to maintain a similar density at each cross section. We do not draw cross sections through or quantify terminus shapes across a ~200 m wide segment at the terminus center (termed the terminus prow), where the multibeam was unable to completely image the terminus face. The terminus prow is deeply undercut and collocated with a large, stable turbid subglacial plume that consistently reaches the fjord surface (*Fried et al.,* 2015; *Jackson et al.,* 2017), factors that, in combination, likely obstructed multibeam imaging. Thus, our dataset represents morphologies across the majority of the terminus and outside of the primary subglacial plume system. At each cross section, we manually removed seafloor

bathymetry and anomalous multibeam returns (e.g. Figure 4.2). We distinguished the seafloor using the sharp contrast in slope between the horizontal sedimentary seafloor and more vertical terminus face. In order to automatically demarcate the terminus face, we defined an interpolated terminus profile through every 2D cross section by calculating the mean x-coordinate at each depth (at 1 m-resolution) within an 11 m moving window, linearly interpolating across windows where multibeam data were absent. Finally, we resampled each interpolated terminus profile to 5 m vertical resolution and applied a moving average, low pass filter to eliminate local, high-frequency noise.

From this database of 190 interpolated terminus profiles, we automated the identification of morphological properties including; 1) the position and depth of the grounding line and; 2) the position and depth of the seaward-most point on the terminus face. The seaward-most point represents the local, farthest advanced terminus position in the proglacial fjord. To define terminus shapes, we calculated the terminus slope, $\theta(z)$, at midpoints along 5 m intervals, measured from the horizontal along each terminus profile. Using $\theta(z)$, we quantified the mean, minimum and maximum terminus slope at each profile location. Finally, we calculated the depth and length of undercutting and overcutting relative to the seaward-most point along each profile, simultaneously cataloging positions and depths of maximum undercutting and overcutting.

We present and analyze these data both in cross sectional and face (i.e. terminus normal) views. To project data along the terminus in a face view, we first calculated the total distance between adjacent cross sections. We define a terminus distance of zero at the northeast glacier margin (0 km in Figure 4.1), and the distance increases to the

southwest glacier margin. We used this distance to project depth dependent data at each terminus profile onto a 5 m grid representing the submarine terminus face. We linearly interpolated between data observed at each profile to map a detailed, complete view of morphology and shape across the entire submarine terminus face.

4.2.2. Terminus positions

In order to quantify changes in map-view terminus position (*dL/dt*) at KAS during the multibeam survey period, we captured successive terminus configurations on 16 July and 27 July 2013 using 20-m resolution TerraSAR-X satellite imagery (courtesy of the German Aerospace Center, DLR). From these images, we manually digitized terminus positions following *MacGregor et al.* [2012] using Esri ArcGIS software.

4.2.3. Modeling subglacial plumes

We use buoyant plume theory to model subglacial plumes at the terminus. In particular, we use the model to constrain subglacial discharge fluxes and explore processes that produce undercutting where we infer concentrated submarine melting. To accomplish this, we use the line plume model [*Jenkins*, 2011; *Jackson et al.*, 2017], which conserves volume, momentum, heat, and salt as the plume rises along the terminus face,

$$\frac{d}{dx}(bu) = \dot{e} + \dot{m}$$

$$\frac{d}{dx}(bu^2) = bg' \sin\theta - C_d u^2$$

$$\frac{d}{dx}(buT) = \dot{e}T_a + \dot{m}T_b - C_d^{1/2} u \Gamma_T (T - T_b)$$

$$\frac{d}{dx}(buS) = \dot{e}S_a + \dot{m}S_b - C_d^{1/2}u\Gamma_S(S - S_b)$$

where b, u, T and S are the plume width, velocity, temperature, and salinity, respectively, which are assumed uniform across the plume. The plume produces melting at rate $\dot{m}$ and entrains fjord water at rate $\dot{e}$, which follows the entrainment parametrization [*Pedersen*, 1980; *Jenkins* 2011] as $\dot{e} = \alpha \sin\theta\, u$. Here, $\alpha = 0.08$, which is an experimentally determined coefficient (Turner, 1979) and $\sin\theta$ is the sine of the terminus face slope. The reduced gravity of the plume, g', is defined through an equation of state [*Fofonoff and Millard*, 1983]. C_d is a drag coefficient, and Γ_T and Γ_S are heat and salt transfer coefficients, respectively. Fjord temperature T_a and salinity S_a are entrained in the plume at rate $\dot{e}$. Finally, interface temperature T_b, salinity S_b, and submarine melt rate $\dot{m}$ are defined using the standard three equations balancing heat and salt at the ice/ocean interface [*Holland and Jenkins*, 1999; *Jenkins*, 2011]. We track modeled depth-varying submarine melt rates and vertical plume velocity along the terminus face. We define the maximum plume height as the depth at which the modeled vertical plume velocity equals zero.

We constrain temperature and salinity stratification in the proglacial fjord at the time of the multibeam survey using a CTD cast collected < 1 km from the KAS terminus in July 2013 (Figure 4.11; Supporting Information). Casts collected at other fjord locations reveal spatially homogenous fjord stratification (Figure 4.11; Supporting Information). From these data, we convectively-adjusted temperature and salinity profiles for use in the plume model, following *Carroll et al*. [2016] and *Jackson et al*. [2017].

4.3. Results

4.3.1. Characteristic terminus shapes

The multibeam point cloud reveals significant vertical and horizontal heterogeneity in submarine terminus morphology. From this complexity, we identify four characteristic, or end-member, submarine morphologies that populate the KAS terminus face (Figure 4.3).

First, we find terminus profiles that are overcut defined by seaward-most points located at the grounding line (Figure 4.3b). Above the grounding line, the terminus face slopes glacier-ward at more than 90° and, in some cases, exceeding 120°. Total overcut lengths measured horizontally from the seaward-most point (at the grounding line) to the farthest observed glacier-ward positon can exceed 100 m. However, overcutting lengths are generally small and infrequently exceed 25 m. In addition, all overcut profiles are texturally rough, that is they include mid-depth notches defined by sharp changes in slope. Panel B in Figure 4.3 highlights this morphology; a distinct "bench" occurs between 120 and 150 m depth, where the terminus shape locally exceeds 130°.

Second, we find undulating morphologies defined by mid-depth seaward-most points, with small amounts of overcutting overlying undercut cavities. Overall, undulating morphologies are undercut, with undercutting extending 10s of meters beneath the terminus (Figure 4.3c and 4.3d). Terminus slopes within the relatively modest undercut cavities can approach 50-60°. Undulating locations feature prominent inflections where the terminus slope is 90° at the seaward-most point (e.g. Figure 4.3c), or, less frequently, at multiple depths (e.g. Figure 4.3d), above which the terminus is

overcut. While all undulating profiles are undercut, maximum undercutting can occur at the grounding line (e.g. Figure 4.3d), but also at intermediate depths (e.g. Figure 4.3c), below which the terminus face protrudes back into the proglacial fjord toward the grounding line forming a grounding line toe.

Third, multibeam data reveal gently undercut morphologies defined by shallow and relatively smooth slopes (Figure 4.3e). Terminus face slopes are restricted to 60-90° at these locations and decrease gradually with depth. Maximum undercutting is generally less than 100 m and consistently occurs at the grounding line, while seaward-most points occur at the depth closest to the tidewater line.

Finally, we confirm the presence of six deeply undercut morphologies (e.g. Figure 4.3f), defined by maximum undercutting at the grounding line that exceeds 100 m and frequently more than 200 m. Grounding line toes are absent at these locations. Generally, seaward-most points occur at intermediate depths, forming well-defined inflection points – or apexes – for the deeply undercut cavities below. Depths of seaward-most points range from 30 to 120 m below sea level. The terminus slope within these undercut cavities consistently approaches 45° and are as low as 30° in the most severe locations (Figure 4.4b). In contrast, the terminus shape approaches and exceeds 90° at the seaward-most point and above, respectively. These regions have been previously identified as subglacial plume outlets due to their unique, undercut morphology and collocation with subglacial channels [*Fried et al.,* 2015].

These characteristic morphologies are associated with local, short-term terminus position changes concurrent with the multibeam survey (Figure 4.3a). For example, the

overcut and gently undercut morphologies (cross sections B and E in Figure 4.3) are associated with areas of relatively quiescent, small-magnitude (20 m or less) terminus position changes. In contrast, we observe localized, large-magnitude terminus retreat (90 m or more) collocated with both the deeply undercut subglacial plume outlet and the more severely undercut undulating morphology (cross sections D and F in Figure 4.3). These latter morphologies share large amounts of undercutting extending both horizontally under glacier toward the grounding line and vertically along the terminus face, closer to the glacier surface.

4.3.2. Morphology distributions across the terminus

We examine the location, distribution and geometry of these morphological features by mapping (Figure 4.4) and calculating statistics (Figure 4.5) of the complete submarine terminus from the database of terminus profiles. Across the terminus face, seaward-most points define boundaries between overcutting and undercutting (pink markers in Figure 4.4a), and thus where the terminus slope is vertical (contour line in Figure 4.4b). The distance of the seaward-most point above the grounding line represents the vertical extent of undercutting, or overcutting if equal to zero (Figure 4.5b).

The majority of the terminus face is undulating, with moderate undercutting of 100 m or less (Figure 4.4). Nearly 40% of undulating regions exhibit grounding line grounding line toes (Figure 4.5d), where maximum undercutting occurs above the grounding line (e.g. between 500-700 m and 2500 – 3100 m in Figure 4.4). Including undulating profiles, we find that 77% of the terminus is undercut, with 55% of undercut cavities extending more than 100 m above the grounding line and towards the fjord

surface (shallow seaward-most points in Figure 4.5b). The six deeply undercut subglacial plume outlets comprise ~15% of the terminus face (Figure 4.5c) and are dispersed across the glacier front (Figure 4.4). Within these outlets, slopes steeper than 45° are not confined near the grounding line and can occur at intermediary depths throughout the outlet (e.g. outlet 5 near 900 m and outlet 1 near 4700 m in Figure 4.4b), creating cavities with concave and vaulted roofs. Gently undercut morphologies are anomalous and predominantly confined to a broad, ~350 m wide segment along the northeast terminus face (1300 – 1650 in Figure 4.4). The remaining 23% of the glacier front is overcut (Figure 4). Overcutting is distributed sporadically, but the largest overcutting is concentrated in deep water at the terminus center (Figure 4.4a).

Further, we calculate the mean slope at each terminus profile to constrain the distribution of shapes across the terminus (Figure 4.6). The median slope for all profiles is 83°, revealing that the average terminus is moderately undercut (Figure 4.6) and strongly influenced by undulating regions, for which the median slope is 79°. Median slopes decrease from overcut to deeply undercut characteristic morphologies. While undulating profiles have an expectedly large range of mean values, gently undercut regions have the smallest interquartile range and thus the smoothest, most consistent terminus slopes.

4.3.2.1. Anatomy of an overcut terminus face

To better constrain overcut geometries, we survey the suite of cross sections (Figure 4.7) through the broad, overcut region southeast of the terminus center (between 3600-3780 m in Figure 4.4). Here, overcut morphologies are laterally homogeneous

relative to disparate terminus shapes surrounding subglacial plume outlets (i.e. Figure 4.8). Terminus profiles are texturally rough; that is, they include mid-depth notches defined by sharp slope breaks (Figure 4.7). Overcut lengths are greatest (> 75 m) where the terminus slope forms a bench and locally exceeds 130° (profiles A and B in Fig. 4.7). This morphology diffuses across glacier and a shallower bench forms to the southeast (e.g. cross sections F, G and H in Figure 4.7).

4.3.2.2. Anatomy of a subglacial plume outlet

We examine the morphology of subglacial plume outlets in more detail by surveying the suite of terminus profiles surrounding outlet #2 (Figure 4.8). Cross sections (A–F in Figure 8) reveal abrupt and distinct morphological transitions through the outlet (between 4150-4275 m in Figure 4.4). The northern margin (cross section A in Figure 4.8) transitions to undulating morphologies (cross section B and C in Figure 8) with moderately undercut cavities (< 75 m under glacier) and small, protruding grounding line toes. These undulating shapes feature small overcut notches proximal to the tidewater line (Figure 8). While undercut cavities here are steepest at intermediate depths and strongly concave toward the fjord, the main subglacial plume outlet (cross sections D and E in Figure 8) is severely undercut (> 100 m) with a vaulted cavity roof that steepens (< 45°) toward the grounding line, and does not exhibit a grounding line toe. Within the outlet, undercutting exceeds 100 m and transitions from steeply undercut to predominantly vertical above the seaward-most point (Figure 8). The southern margin is defined by a minimally overcut (~10 m) terminus shape (cross section F in Figure 8).

4.3.3. Subglacial discharge fluxes in subglacial plume outlets

Previous modeling work has shown that terminus undercutting extends vertically from the grounding line to where buoyant plumes reach their maximum height at neutral buoyancy in the proglacial fjord [*Slater et al.*, 2017]. Thus, observed seaward-most points represent proxies for both the maximum plume height and the vertical extent of plume-driven melting within identified subglacial plume outlets. We use this knowledge and our direct observations of the subglacial plume outlet geometries to constrain discharge fluxes (Qsg) emerging from outlets at the grounding line using the line plume model (*Jenkins*, 2011). The model incorporates observed outlet widths and grounding line depths to estimate the subglacial discharge flux required to produce a subglacial plume whose maximum height matches the observed mean depth of the seaward-most point in each outlet (Table 4.1; Figure 4.9; Supporting Information). We measure outlet widths as the horizontal distance at the grounding line between 100 m undercut contours (Table 4.1). In the absence of additional constraints, we assume that all undercutting at these locations is plume-driven. Therefore, we take a conservative approach by assuming that seaward-most points represent the maximum potential vertical extent of plume-driven melt for each outlet.

We find that, in general, small estimated subglacial discharge fluxes produce buoyant plumes that match observed terminus face morphologies (Figure 4.9; Table 4.1). Modeled plumes rise rapidly at low discharges due to weak fjord stratification near the grounding line (Figure 4.9). Larger fluxes are required to generate plumes that rise

through strong gradients in fjord stratification at shallower depths (Figure 4.9; observed temperature and salinity stratification in Figure 4.11). Given incorporated outlet widths and grounding line depths, estimated discharge fluxes range from 2.5 to 36 $m^3 s^{-1}$, with a mean flux of 14 $m^3 s^{-1}$ between the six identified subglacial plume outlets (Figure 4.9). The total estimated discharge flux feeding the six outlets is 84 $m^3 s^{-1}$. In general, depths of seaward-most points vary by less than 20 m across subglacial plume outlets (Table 4.1). Smaller discharge fluxes would be required to match the deepest (maximum) seaward-most point depths alone. Modeled maximum melt rates range between 1.25 m d^{-1} and 2.5 m d^{-1}, with greater melting associated with plumes fed by the largest discharge fluxes (Figure 4.12).

Given observed fjord stratification (Figure 4.11), maximum plume heights are more sensitive to changes in subglacial discharge flux than changes to either outlet geometries, including widths and grounding line depths (Figure 4.10). In general, maximum plume heights increase (decrease) with narrower (wider) outlets and shallower (deeper) grounding lines (e.g. panel a in Figure 4.10), due to greater (smaller) initial plume velocity and lower (higher) entrainment of ambient fjord water. However, we find that increases in discharge flux produce a larger range of maximum plume heights than changes in outlet geometries for a given discharge flux (i.e. the range of maximum plume heights within panels 4.10a and 4.10f are smaller than the range between them). Additionally, the range of maximum plume heights is smaller for large discharges (e.g. Qsg = 30 $m^3 s^{-1}$) than for small discharges (e.g. Qsg = 1 $m^3 s^{-1}$) for the parameterized outlet widths and grounding line depths (Figure 4.10), suggesting that subglacial plumes

are most sensitive to geometric controls under low discharge fluxes and large fluxes diminish geometric influence. Indeed, independent of each outlet's unique width and grounding line depth, significantly larger discharge fluxes are required to force buoyant plumes through the strong density stratification (pycnocline) in upper 80 m of the water column and to the fjord surface (Table 4.1).

4.4. Discussion

4.4.1. Deep morphology

Our results interpret previously unappreciated diversity in submarine morphologies across a Greenlandic tidewater glacier terminus. In turn, for the first time, we use these morphologies to explore a range of frontal ablation processes across the terminus, including discharge fluxes feeding subglacial plumes, submarine melting and calving. We identify four characteristic morphologies ranging from overcut to deeply undercut near subglacial plume outlets, with most of the terminus characterized by an undulating undercut morphology (Figure 4.4). The median observed terminus slope is 83° (Figure 4.6), although slopes are steeper than 45° within subglacial plume outlets and exceed 120° at overcut locations (Figure 4.4b). Seaward-most points define the vertical limit of undercutting along the terminus face, the majority of which are located more than 100 m from the grounding line (Figure 4.4 and 4.5b). We expect morphologies observed in our dataset are similar to other Greenland tidewater glaciers with broadly similar flow dynamics and meltwater catchments.

Observed terminus morphologies are symptomatic of ice loss at the terminus from both calving and submarine melting, collectively referred to as frontal ablation [*Bartholomaus and Bassis*, 2014]. In general, ice loss below the seaward-most point could be explained as primarily due to melting, because subaerial calving is unlikely to form smooth, undercut and overhanging terminus shapes at depth. In contrast, ice loss above the seaward-most point could occur through a combination of calving and melting, with calving perhaps playing a leading role because surface textures above the seaward-most point are rough (e.g. Figure 4.3b).

4.4.2. Implications for calving

It is possible that large overcut morphologies (such as those in Figure 4.7) result from calving events because submarine melting would alternatively undercut and steepen the terminus face. This inference is supported by terminus position records at KAS, which confirm the terminus region with the largest overcutting (Figure 4.7) was collocated with ~150 m of local retreat before the multibeam survey between July 5 and 16 (see Chapter 3). These calving dominated, overcut morphologies are uncommon, comprising ~23% of the terminus and, unlike those shown in Figure 4.7, typically have relatively small overcut lengths of 50 m or less (Figure 4.4). We propose three calving mechanisms to produce large overcut morphologies. First, overcut shapes could trace the orientation of surface crevasses that penetrate into the glacier interior. However, it is unlikely that surface crevasses propagate seaward as they move toward the glacier bed. Second, overcut morphologies may form through a cascade effect. In this mechanism, the glacier front initially calves along a deeply penetrating crevasse, perhaps after connection

with an undercut cavity, and subsequently destabilizes shallow, secondary crevasses and seracs further up-glacier. This additional calving overcuts the terminus face by eroding the dense network of crevasses and damaged ice concentrated near the glacier surface. Third, crevasse tips could "short-circuit" and connect to the terminus face along subhorizontal lines of concentrated stress and tear. This mechanism would facilitate larger ice loss at shallower depths and also manifest benches, or notches, within the overcut terminus face (e.g. those observed in profiles A and B in Figure 4.7). Because of their rough surface texture defined by distinct mid-depth notches and benches, we suggest broadly overcut morphologies represent the integrated effect of multiple calving events.

We also find that small, shallow overcut notches near the tidewater line are widespread across the terminus and common to a range of characteristic terminus morphologies (e.g. at both overcut and undulating morphologies in profiles A and B in both Figure 4.7 and 4.8). These pervasive features could result from both enhanced shallow subsurface ambient melting following the diffusion of warm summer air temperatures through the near-surface water column (e.g. Figure 4.13) and tidal forcing, which permit frequent, small-magnitude serac calving, or sloughing.

Previous studies show that terminus undercutting can mechanically initiate calving [*Vieli et al.,* 2001; *O'Leary and Christoffersen,* 2013; *Bartholomaus et al.,* 2013] by connecting undercut cavities with overlying surface crevasses [*Fried et al.,* 2015]. Our observations provide new insights into this relationship by highlighting the diversity of undercutting styles present at the terminus and recognizing certain shapes that may

preferentially trigger calving. We argue that, given an equal distance of undercutting under glacier, undercutting focused at shallow depths more likely connects with depth penetrating surface crevasses and facilitates calving than undercutting confined near the grounding line. We provide evidence to support this interpretation. During the multibeam survey period, we observe localized terminus retreat exceeding 90 m above terminus morphologies with steep undercutting at shallow depths (profiles D and F in Figure 4.3). These morphologies are most likely to evolve after the start of the melt-season, when increases in subglacial discharge manifest large, mature melt-driven terminus undercutting (Figure 4.13). In contrast, we observe terminus advance where undercutting is restricted to deeper depths (profiles C and E in Figure 4.3) or where the terminus is overcut (profile A in Figure 4.3). We lack data with higher temporal resolution to better constrain this relationship; future work could focus on collecting coincident high-frequency time series observations of both the submarine terminus and calving front to better quantify this response.

4.4.3. Implications for subglacial plume outlets and discharge fluxes

Using a truncated line plume model [*Jenkins et al*., 2011; *Jackson et al*., 2017], we find that small subglacial discharge fluxes produce buoyant subglacial plumes that match observed terminus face morphologies (Figure 4.9; Table 4.1) These discharge fluxes resemble a more distributed, near-terminus subglacial drainage network, which is expected to support numerous, secondary subglacial plume outlets across the terminus [*Fried et al*., 2015]. Although incomplete multibeam data precluded its inclusion in this study, oceanographic measurements estimated the subglacial discharge flux emerging

from the large subglacial channel at the terminus prow to be ~200 $m^3 s^{-1}$ in July 2014 [*Jackson et al.*, 2017]. Assuming a similar flux there in July 2013, we estimate all subglacial plume outlets at KAS are fed by a total of ~284 $m^3 s^{-1}$ during the peak melt season, which marginally exceeds mean predicted runoff to the KAS terminus (~240 $m^3 s^{-1}$) estimated from the RACMO2.3 regional climate model in July 2013 (*Ettema et al*., 2009). We may underestimate discharge fluxes at outlets 4 and 5 because their seaward-most points occur at the top of the terminus cross sections and are unassociated with inflection points. While these small discharge fluxes drive significant and dispersed submarine melting across the terminus, secondary outlet locations do not experience commensurately large seasonal retreat compared to the terminus prow region where the largest, most persistent subglacial plume is located [*Fried et al*., 2015; *Jackson et al*., 2017]. Because terminus change from calving is concentrated at the terminus prow [*Fried et al*., 2015], we speculate that ~70% of the total discharge delivered to the terminus – the percentage of our budget estimated by *Jackson et al*. [2017] at the prow outlet – controls the majority of observed seasonal terminus position change at KAS.

Ultimately, vertical plume velocities and thus maximum plume heights are more sensitive to subglacial discharge flux than changes to outlet geometries (Figure 4.10). This sensitivity suggests increases in meltwater runoff and subglacial discharge in a warming climate could lead to more extensive, vigorous plumes and, in turn, greater ice fluxes lost to submarine melting. We find that, independent of outlet geometry, increasingly large discharge fluxes are required to produce plumes that penetrate strong upper-fjord stratification (Figure 4.9; Figure 4.11). Indeed, the majority of seaward-most

points in plume outlets reside between 60-80 m below sea level and below the fjord pycnocline, suggesting a possible feedback between fjord stratification, maximum plume heights and the morphology of the submarine terminus face (Figure 4.9; Figure 4.13). In turn, unrealistically large discharge fluxes are required to produce plumes that rise to the fjord surface (Table 4.1). Cumulatively, these discharge fluxes greatly exceed runoff estimates from regional climate models, which provides an explanation for the absence of observed surface plumes in the satellite record [*Fried et al.*, 2015]. Overall, our observations suggest smaller, secondary subglacial plume outlets drive substantial melting and undercutting, but remain undetected at the fjord surface due to their relatively small discharge fluxes.

Finally, our morphological observations broadly support recent numerical experiments simulating terminus face shapes produced by melting in subglacial plumes. *Slater et al.* [2017] found that small, preexisting subglacial channels are a required boundary condition to maintain undercutting at the grounding line within subglacial plume outlets. In the absence of channels, grounding line toes develop due to melt rate maxima that occur above the grounding line [*Carroll et al.*, 2016; *Slater et al.*, 2017]. We do not observe grounding line toes within plume outlets, which is perhaps indicative of a smooth channel to plume transition deep within the steeply undercut outlets. Undulating morphologies containing grounding line toes immediately adjacent to subglacial plume outlets (e.g. Figure 4.8), may be indicative of complex melting patterns at lateral plume margins not explicitly resolved in this study.

We expect that the results of this study apply to other tidewater glaciers around Greenland. Glaciers with small near-terminus surface gradients may release even more of their subglacial discharge through a distributed subglacial hydrologic network. In turn, this may drive greater rates of submarine melt. While glaciers similar in size to KAS calve predominantly via serac failure, more work is needed to identify connections between subglacial discharge and calving at glaciers with floating tongues and those dominated by larger-scale, slab-rotation calving events [e.g. *Murray et al*., 2015], if any relationship does exist.

4.5. Conclusions

Frontal ablation rates at tidewater glacier termini regulate the amount of dynamic ice loss from the Greenland ice sheet to the ocean. To better constrain processes and boundary conditions controlling frontal ablation, we have presented detailed constraints on the shape of the terminus and previously unrecognized submarine terminus morphologies. We find several characteristic, end-member morphologies that populate distinct submarine terminus regions and range from overcut to steeply undercut around subglacial plume outlets. In turn, these morphologies are indicative of calving and melting across the glacier front. We find that the majority of the terminus is undulating and undercut, sculpted by both subaerial calving at shallow depths and melting that manifests deep overhanging cavities. Our observations uncover styles of undercutting that more likely trigger calving above. We suggest that, given an equal length of undercutting under glacier, morphologies concave toward the fjord and with undercutting

concentrated at shallow depths more likely destabilize the terminus through connection with overlying surface crevasses than undercutting confined near the grounding line. In turn, overcut morphologies represent the integrated effect of multiple calving events and are more frequent at shallow depths due to the predominance of crevasses, seracs and low overburden pressures near the tidewater line. Calving induced, overcut regions are sporadic and comprise only ~23% of the terminus face. We argue observations of calving surfaces presented here could provide critical constraints for iceberg and calving resolving simulations.

Finally, we provide detailed constraints on the geometry and location of six deeply undercut (< 45°) subglacial plume outlets. We find that relatively small discharge fluxes, reminiscent of a distributed network, generate buoyant plumes that match observed outlet morphologies. Maximum subglacial plume heights are more sensitive to changes in discharge flux than changes to outlet geometries from which they emerge. Indeed, unrealistically large discharge fluxes are required to produce plumes that rise through strong upper-level ocean stratification and reach the fjord surface. As a result, undercutting generally remains below the fjord pycnocline. Together, these observations suggest secondary subglacial plumes are ubiquitous at tidewater glacier termini but remain undetected at the fjord surface due to their small discharge fluxes. While secondary subglacial plumes fed by small discharge fluxes drive significant melting and undercutting dispersed across the terminus, they do not drive equally large calving rates compared to the terminus center, where the majority (~70%) of subglacial discharge feeds a large, persistent plume observed at the fjord surface.

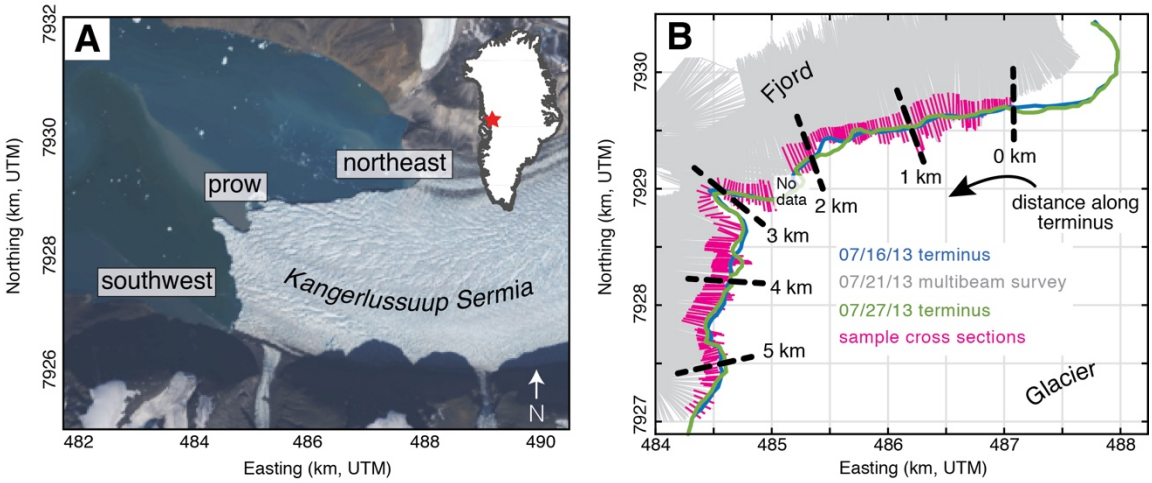

Figure 4.1. A) Landsat image showing location and overview of the terminus at Kangerlussup Sermia (KAS). B) Map showing locations of raw multibeam returns (grey); 190 sample cross sections through the multibeam point cloud (pink lines); map-view terminus positions on either side of the multibeam survey on 21-23 July 2013 (16 July 2013 in blue and 27 July 2013 in green); distance markers along the segmented terminus (black dashed lines) increasing from 0 km in the northeast to ~5.5 km in the southwest.

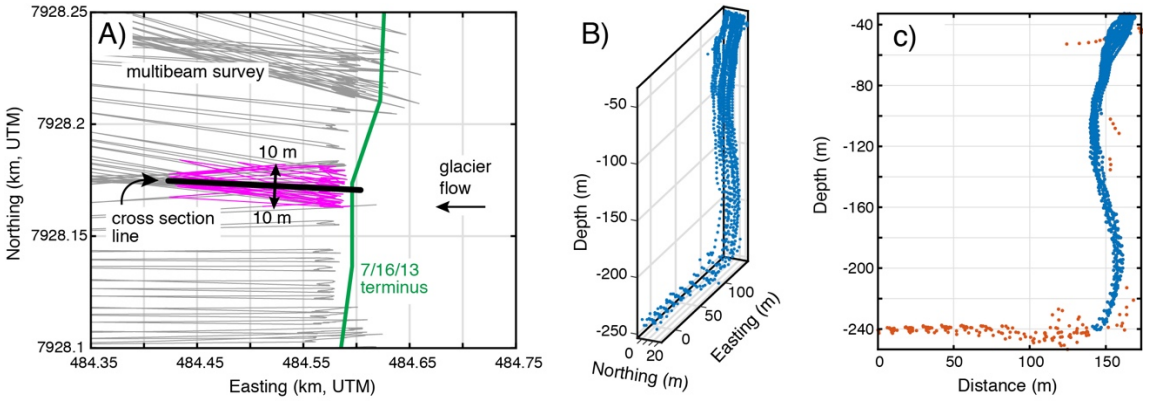

Figure 4.2. Example showing extraction of a terminus profile. A) Cross section line drawn through the multibeam point cloud survey. Multibeam returns collected within 10 m on either side of the cross section line shown in pink. B) Oblique view showing 3D multibeam point cloud along submarine terminus face and seafloor bathymetry. C) Cross section points projected onto a 2D plane. Seafloor bathymetry and anomalous multibeam returns (shown in red) are removed.

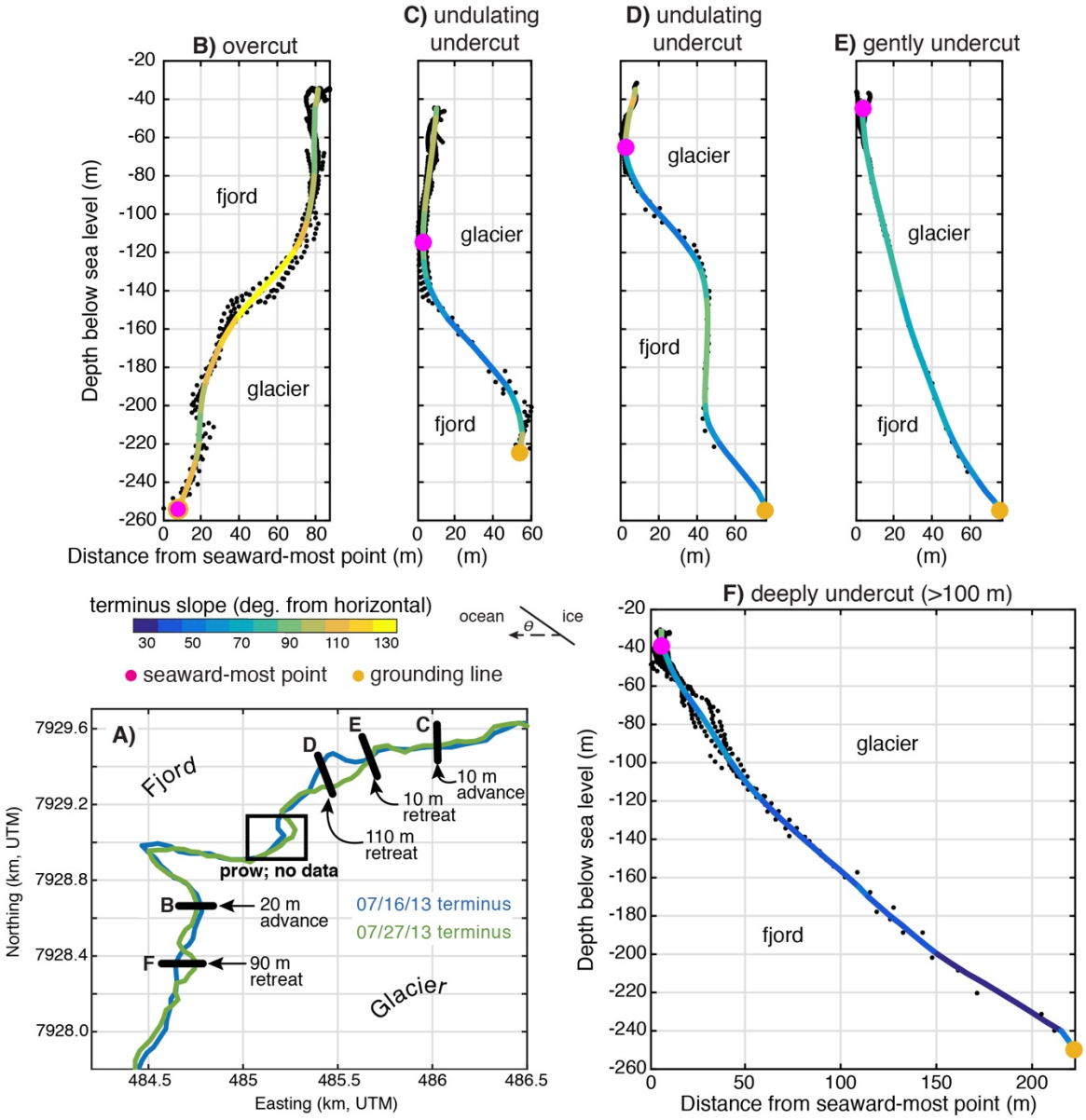

Figure 4.3. Terminus profiles showing characteristic, end-member terminus face morphologies at KAS. A) Map showing cross section locations and corresponding terminus position change before and after the multibeam survey; B) overcut; C and D) undulating undercut; E) gently undercut; F) deeply undercut (>100 m). Cross sections share the same length scale and have equal aspect ratios. Terminus profiles are colored according to the terminus slope, the angle from horizontal. The seaward-most point and grounding line are shown as pink and yellow markers, respectively. Multibeam returns are shown in black in each profile.

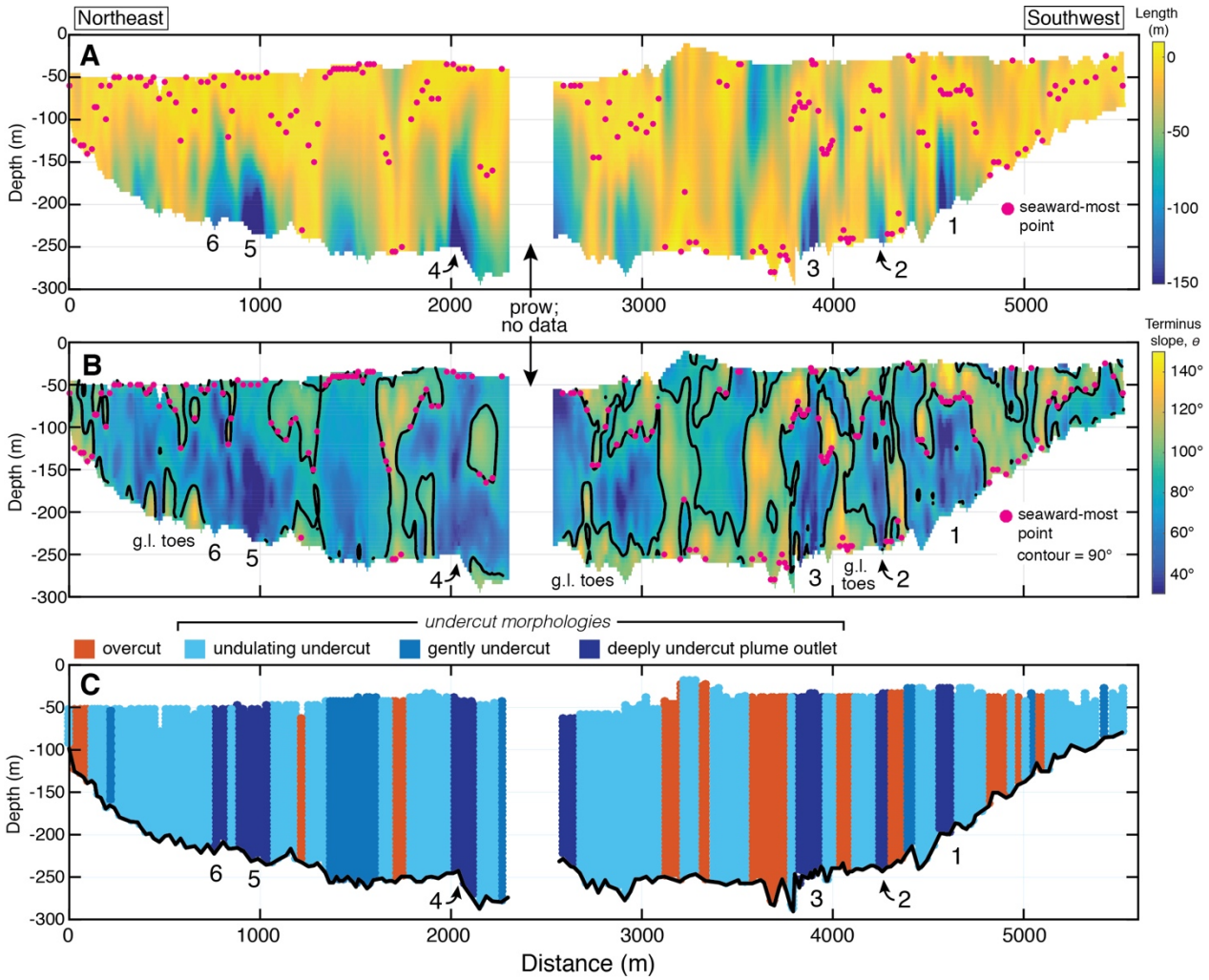

Figure 4.4. Face view of terminus-wide submarine morphologies and slopes between the northeast and southwest terminus margins (left to right). A) Terminus face position relative to the local seaward-most point. Undercut and overcut positions farthest from the seaward-most point are shown in the color scale. Identified subglacial plume outlets are labeled 1-6. B) Terminus slope $\theta(z)$, measured from the horizontal. 90° contour line shown in black. Examples of grounding line toes are annotated. Seaward-most points are shown as pink markers. C) Distribution of characteristic morphologies as identified in terminus profiles.

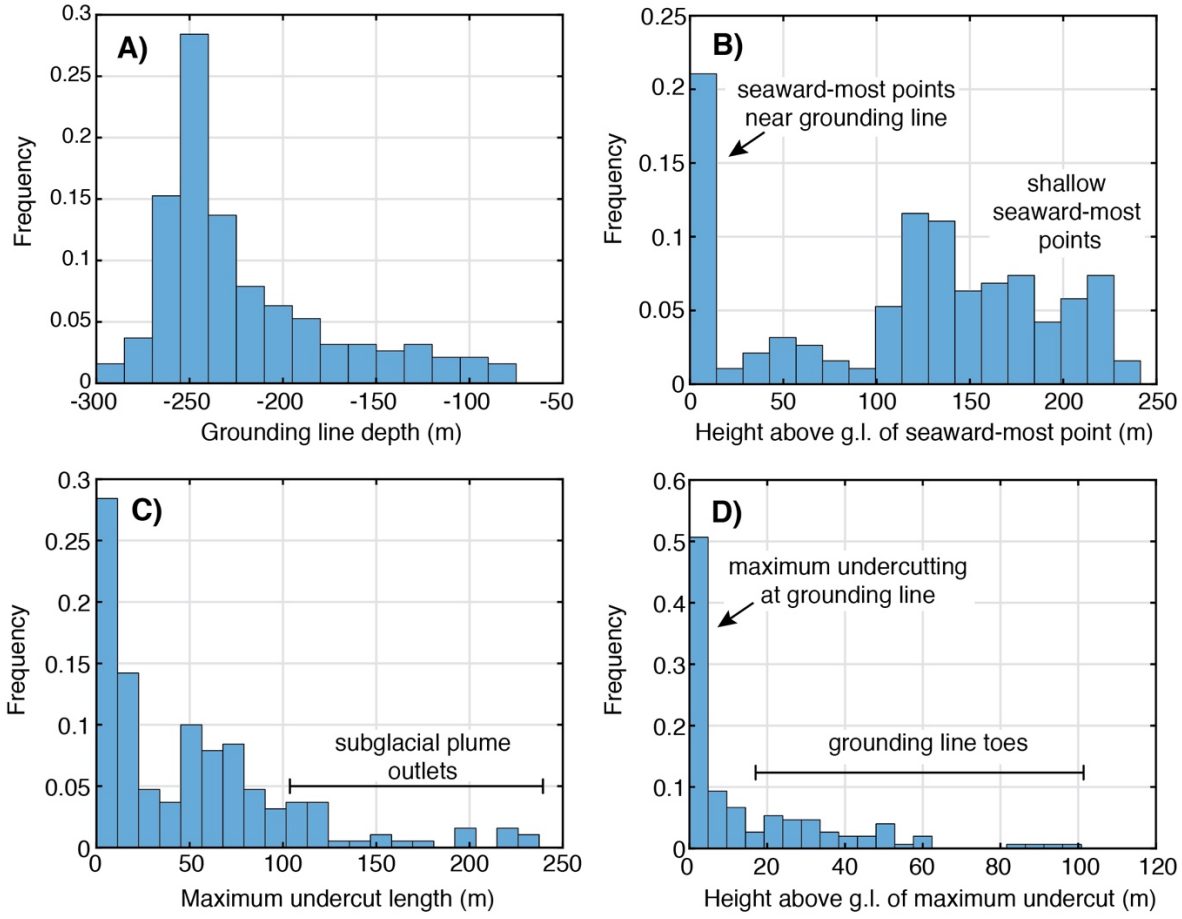

Figure 4.5. Normalized histograms showing morphological data collected at terminus profiles: A) grounding line depth; B) height above grounding line of seaward-most point; C) maximum undercut length (measured relative to the local seaward-most point); D) height above grounding line of maximum undercutting (only includes undercut profiles).

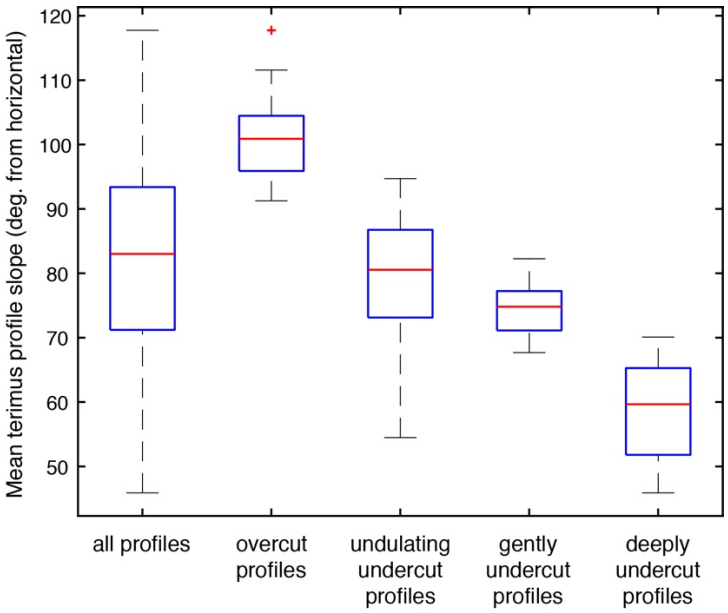

Figure 4.6. Box plots depicting quartiles and distributions for mean, minimum and maximum terminus slopes, θ, calculated at each terminus profile.

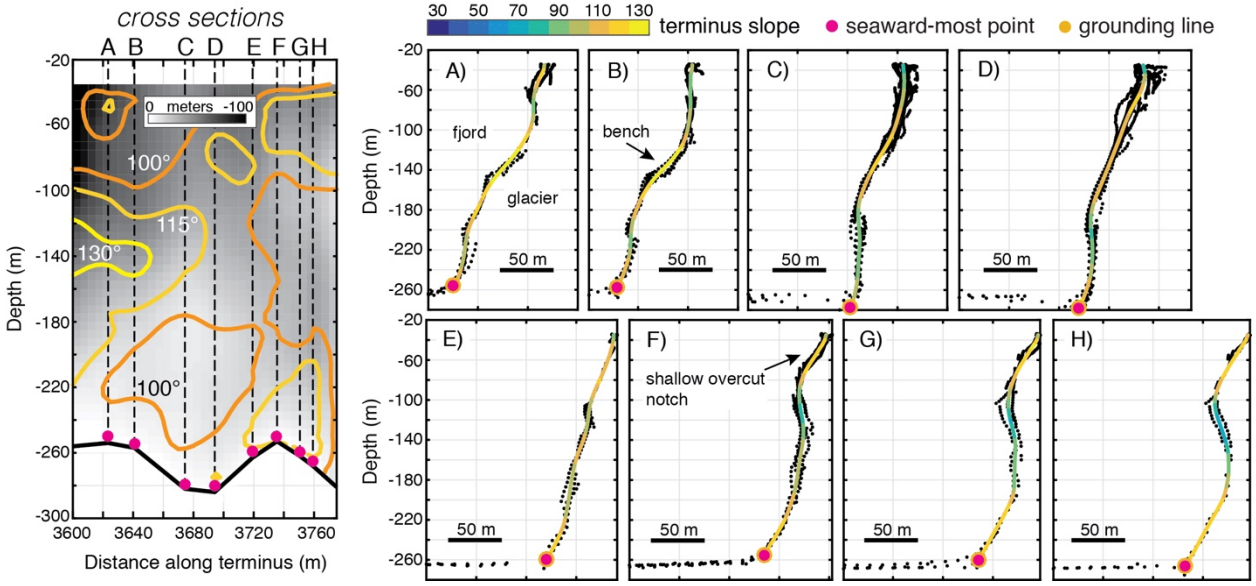

Figure 4.7. Survey of terminus cross sections through a broad overcut region. Face view at left shows cross section locations overlying terminus slope contours (orange to yellow) and a colormap of terminus face position (grayscale) relative to local seaward-most point (pink markers). Cross sections at right show multibeam returns, including the proglacial seafloor and terminus face profiles colored according to the terminus slope. Cross sections share the same length scale and have equal aspect ratios. Seaward-most points and grounding line positions are shown as pink and yellow markers, respectively.

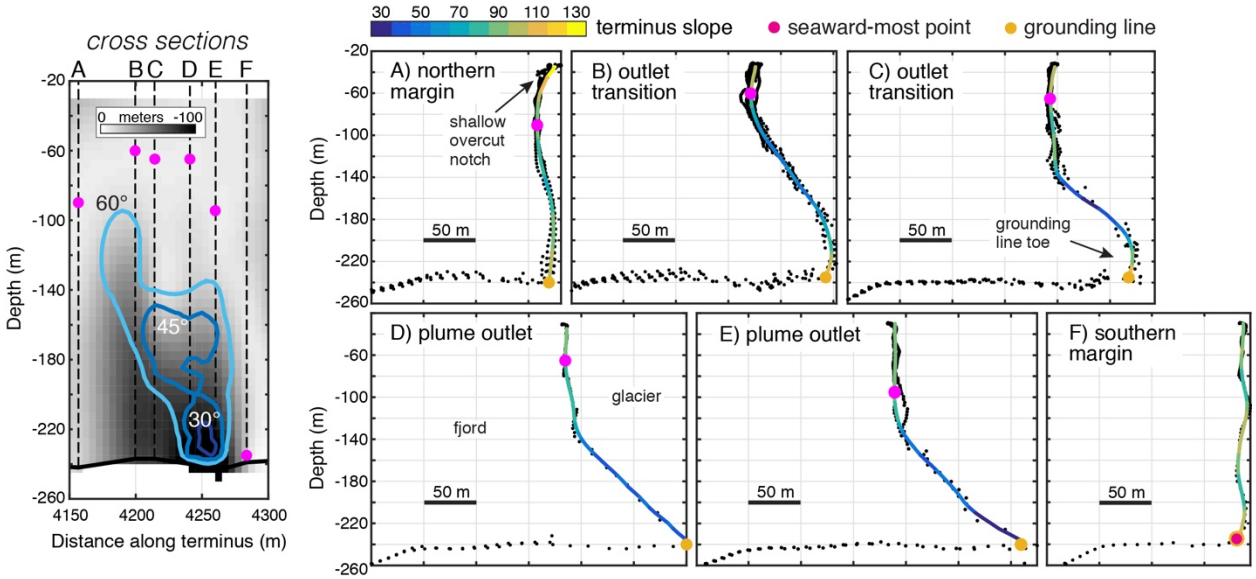

Figure 4.8. Survey of terminus cross sections through subglacial plume outlet #2. Face view at left shows northeast to southwest (left to right) trending cross section locations overlying terminus slope contours (blue) and a colormap of terminus face position (grayscale) relative to local seaward-most point (pink markers). Cross sections at right show multibeam returns, including the proglacial seafloor and terminus face profiles colored according to the terminus slope. Cross sections share the same length scale and have equal aspect ratios. Seaward-most points and grounding line positions are shown as pink and yellow markers, respectively.

Table 4.1. Subglacial plume outlet geometries and estimated discharge fluxes

subglacial plume outlet	grounding line depth (m)	conduit width (m)	mean seaward-most point depth (m)	max seaward-most point depth (m)	min seaward-most point depth (m)	Qsg to match mean seaward-most point depth ($m^3 s^{-1}$)	Qsg to rise to fjord surface ($m^3 s^{-1}$)
1	-200	70	-70	-70	-65	3.5	87
2	-240	30	-80	-95	-65	2.5	47
3	-245	85	-60	-90	-30	13	130
4	-250	115	-40	-40	-30	36	185
5	-225	120	-50	-50	-45	24	166
6	-220	90	-80	-120	-50	4.5	121

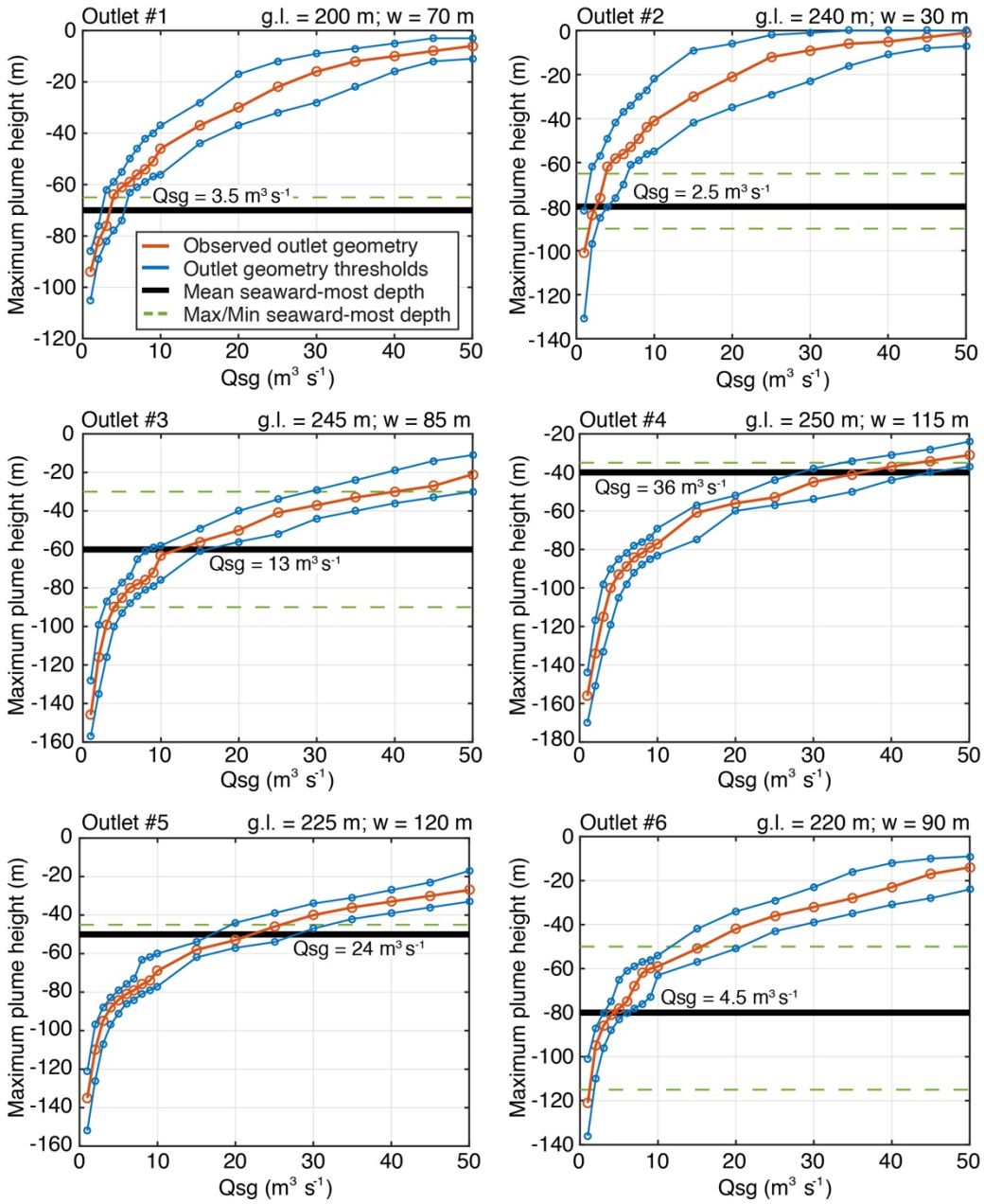

Figure 4.9. Modeled maximum plume height (depth where vertical plume velocity equals zero) versus subglacial discharge flux for six observed subglacial plume outlets. Red lines show maximum plume depths using observed grounding line depths and outlet widths (table 1). Blue lines consider threshold scenarios using deeper grounding lines/wider outlets and shallower grounding lines/more narrow outlets. Solid black horizontal lines denote mean depth of seaward-most points in each outlet (Table 1). Green dashed lines denote minimum and maximum depths of seaward-most points in each outlet. We annotate the subglacial discharge flux that produces the best fit to each mean seaward-most point depth.

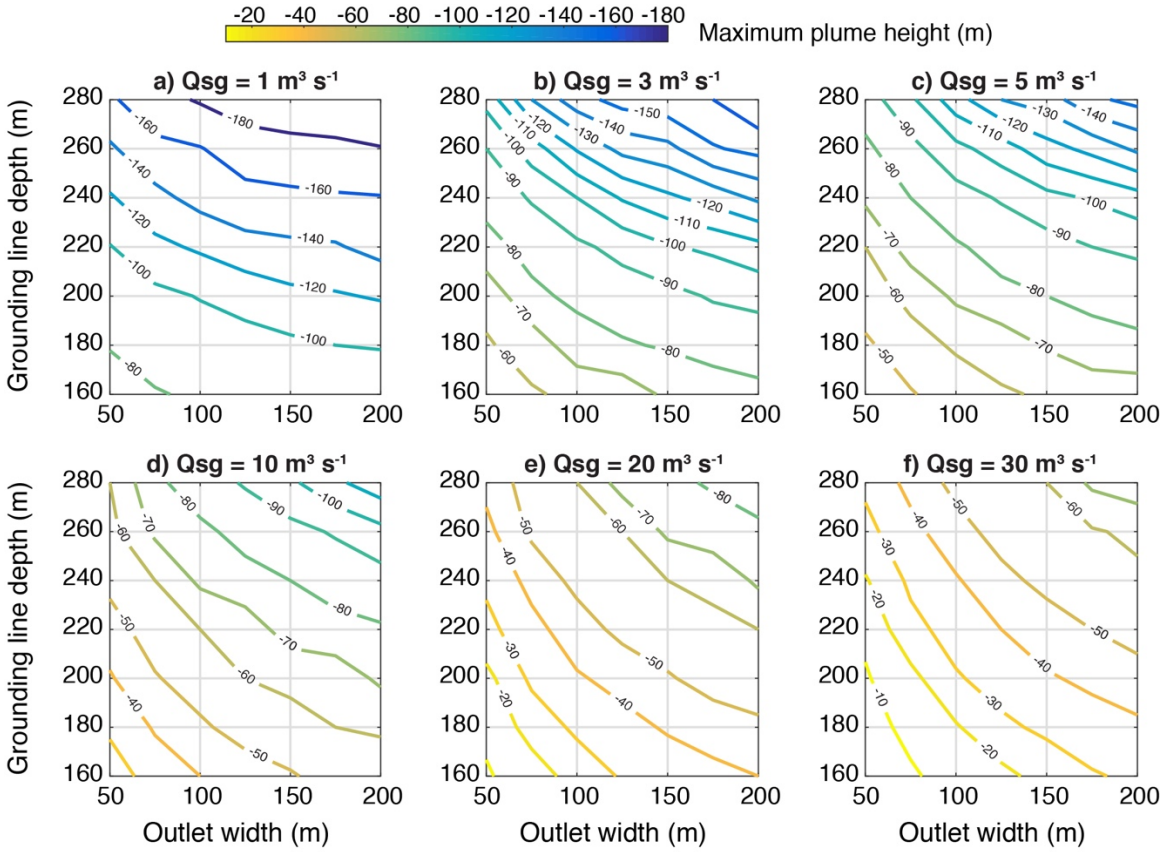

Figure 4.10. Parameter spaces showing modeled maximum plume heights (depth where vertical plume velocity equals zero) for varying outlet geometries under different subglacial discharge flux (Qsg) scenarios (a-f). Contours represent lines of equal maximum plume heights.

4.6. Supporting Information

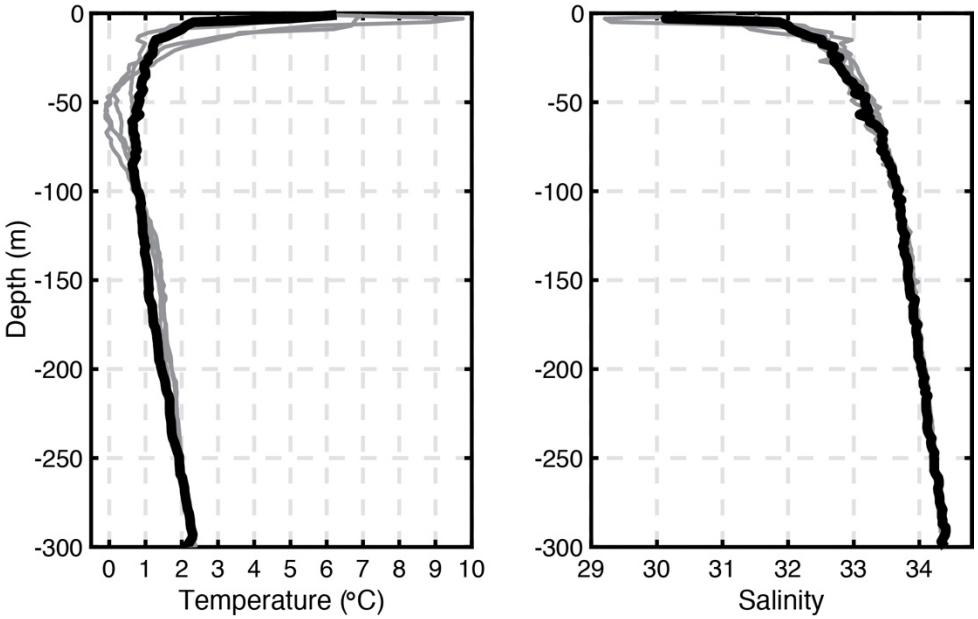

Figure 4.11. Temperature and salinity stratification in the Kangerlussuup Sermia proglacial fjord. T/S profiles from CTD cast collected closest to the KAS terminus (71°47'N, 51°40'W) is shown in bold black. Additional CTD casts collected in the fjord are shown in grey.

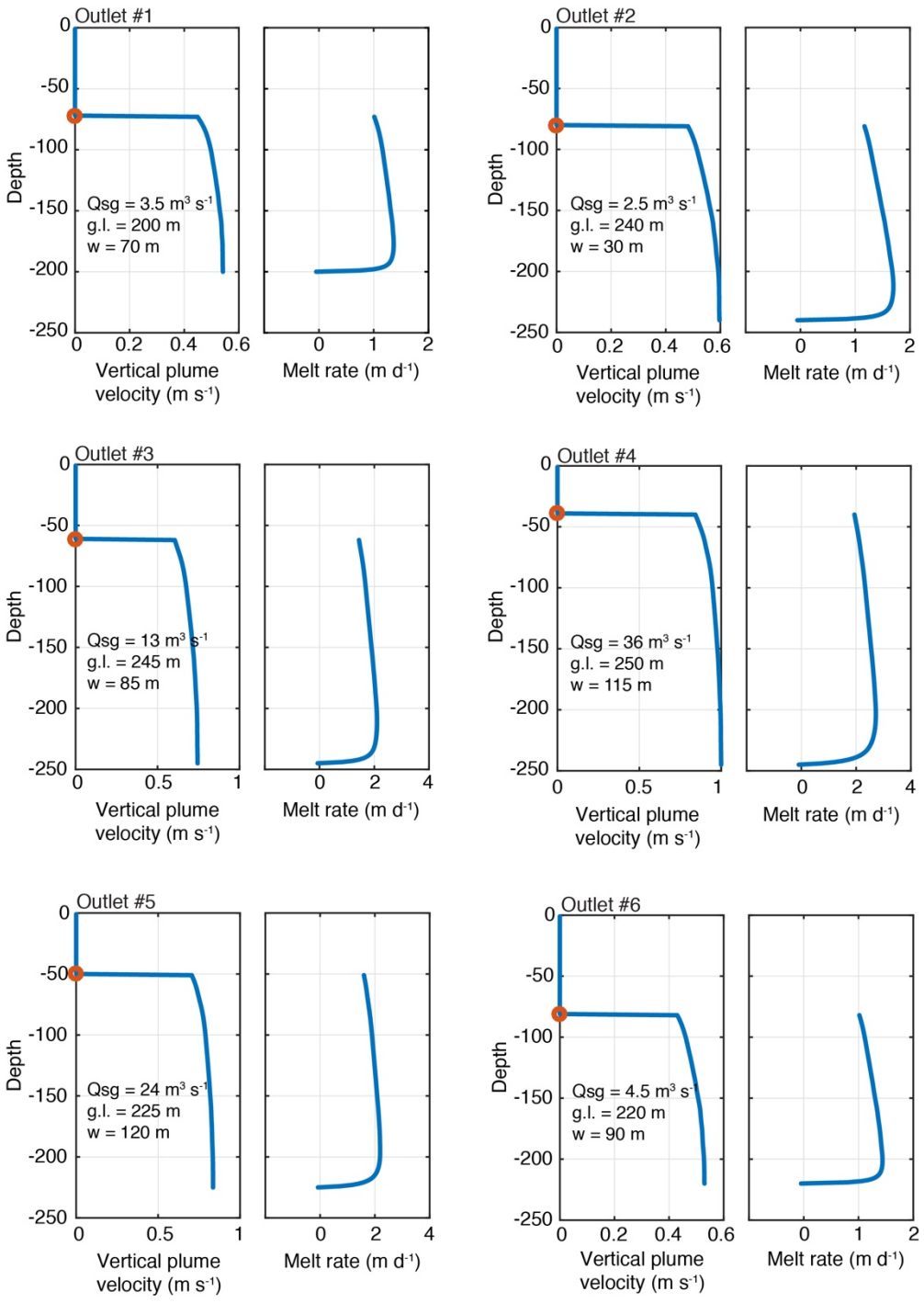

Figure 4.12. Depth-varying vertical plume velocity and melt rate profiles for the six identified subglacial plume outlets for subglacial discharge fluxes that produce plumes whose maximum height matches depth of mean observed seaward-most point. Individual outlet geometries (widths and grounding line depths) are noted.

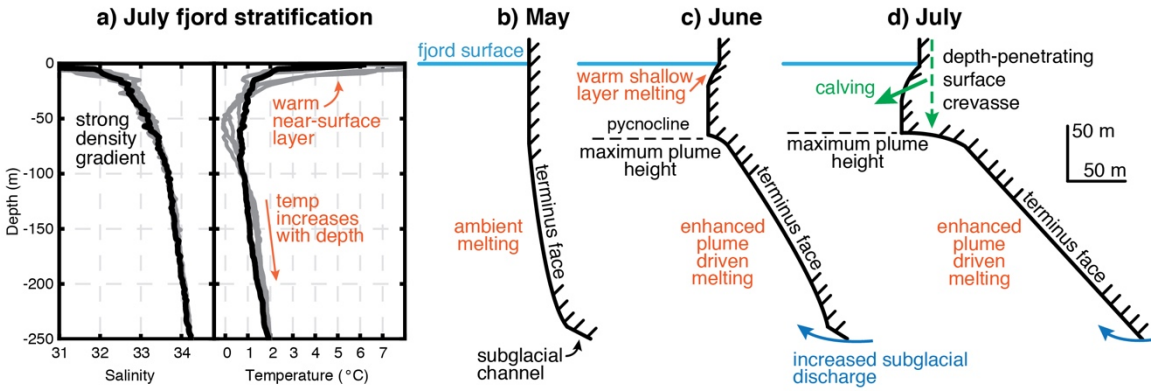

Figure 4.13. Conceptual schematic showing a) July fjord stratification at KAS and b-d) hypothesized evolution of the terminus face between May (prior to summer melt season) and July (peak melt season and timing of multibeam survey and CTD casts). Increased undercutting is caused by enhanced convection and plume driven melting following seasonal increases in subglacial discharge. Maximum plume heights are influenced by strong fjord density gradients and mark the vertical extent of plume driven melting. Shallow overcut thermal notches may form in response to melting from warm near-surface ocean water and sloughing (small-magnitude calving) of the glacier front. Eventually, depth-penetrating surface crevasses may connect with undercut cavities and trigger calving. Depth scale is consistent across the figure.

Chapter 5. Conclusions

5.1. Synthesis

The work presented in this dissertation focuses on processes acting at the terminus of tidewater glaciers that impact frontal ablation and, in turn, changes in terminus position. The terminus region is highly dynamic due to its linkages to the atmosphere, ocean and ice sheet systems. All of these systems can impact terminus position on a range of timescales. In turn, given a sufficient terminus retreat, terminus perturbations can mediate inland ice dynamics through feedbacks involving increased ice flow and surface thinning. Thus, gaining a more complete understanding of controls on ice loss at the terminus and terminus positions through time is fundamental to predicting future dynamic mass loss from the Greenland Ice Sheet (GrIS).

Despite this importance, prior to recent campaigns to image the submarine terminus using multibeam echo sounding, direct knowledge of the morphology of the tidewater glacier terminus and frontal ablation processes occurring there were limited. To attempt to resolve these issues, I pair a multibeam survey of the submarine terminus face with a suite of remote sensing observations to show that meltwater runoff and discharge-driven submarine melting impact the terminus in more complex ways than previously appreciated. In central west Greenland, submarine melt rates are responsible for significant fluxes of ice loss to the ocean and local responses to discharge-driven melting can dominate glacier-wide terminus position adjustments on seasonal timescales. In turn,

glacier outlet geometry and calving flux mediate terminus sensitivity to runoff and submarine melting. Systems with deep grounding lines and ice fluxes that significantly exceed submarine melting can advance hundreds of meters over short time periods, which may supersede undercutting and ice loss from submarine melt. Ultimately, the analysis and conclusions presented in the previous chapters are a pursuit in emergentism. Isolated processes acting at the terminus eventually give rise to the behavior of larger tidewater glacier systems. In turn, the process-oriented results in this dissertation present a clearer view of how environmentally-driven frontal ablation will directly impact regional terminus positions and dynamics in a warming climate.

5.2. Dissertation Summary

Our knowledge of processes controlling submarine melt were traditionally obscured by limited observations of the submarine terminus. This dissertation presents the first estimation of submarine melt rates at each point along the terminus of a tidewater glacier using direct observations from multibeam sonar. While inferred melt rates are similar in magnitude to estimates at other tidewater glacier systems from heat and salt budgets [e.g. *Rignot et al*., 2010; *Motyka et al*., 2013] and mass continuity [*Motyka et al*., 2011], I find previously unrecognized heterogeneity in melt rates across the glacier front. This melt pattern is driven by the presence of numerous, secondary deeply undercut subglacial plume outlets that are situated outside of the main subglacial channel network. While the main subglacial channel produces persistent turbid sediment plumes at the fjord surface and expectedly large melt rates, the distributed subglacial network drives

significant submarine melt elsewhere, locally in excess of 3.0 m d^{-1}. Thus, secondary outlets disperse melt across the terminus, rather than focusing melt at one location. As a result, the combined influence of secondary plume outlets increases the total flux of ice lost to the ocean from submarine melting. Moving forward, I argue that numerical models need to account for rapid melting at smaller, more abundant subglacial plume outlets when exploring causes for terminus perturbations.

I use multibeam sonar to reveal previously unaccounted for morphological complexity at the ice/ocean interface. While the majority of the terminus is undercut, morphologies range from overcut to steeply undercut at subglacial plume outlets. The diversity of observed terminus shapes represents, in turn, the range of frontal ablation processes occurring at the terminus. Previous work hypothesized that terminus undercutting from submarine melting may mechanically destabilize the terminus and induce calving [*O'Leary and Christoffersen*, 2013; *Bartholomaus et al*., 2013]. I advance this understanding and find that undercut terminus morphologies likely trigger serac failures and subaerial calving by connecting with finely-spaced overlying surface crevasses. In turn, large, deep, and perhaps compounding, calving events are the most likely mechanism to produce observed overcutting across the terminus face. Large overcut morphologies are limited across the glacier front, suggesting that large-magnitude calving events are not the primary cause of frontal ablation at the glacier studied.

Observed terminus face morphologies have myriad applications to explore frontal ablation processes. Critical to our understanding of submarine melting and ice loss at the

terminus is the spatial distribution and magnitude of subglacial discharge fluxes. Few studies have validated runoff from regional climate models [e.g. *Smith et al*., 2015] and none in the submarine environment. Previous modeling work shows that glacier fronts become strongly undercut at the maximum height reached by subglacial plumes [*Slater et al*., 2017]. We use this information and direct observations of outlet geometries in a plume model [*Jenkins*, 2011] to estimate subglacial discharge fluxes required to produce subglacial plumes whose maximum height rises to undercut cavity roofs. The resulting model experiments find that generally small discharge fluxes feed numerous, secondary subglacial plume outlets. Integrated discharge at all terminus outlets exceed average RACMO runoff estimates by ~50 m^3 s^{-1} over the period of interest. While these relatively small discharge fluxes drive significant melt rates and steeply undercut morphologies, terminus positions remain relatively stable at these locations, due, in part to the fact that subglacial plumes do not reach the fjord surface and are constrained by the fjord pycnocline. Indeed, model experiments reveal that, given observed outlet geometries, unrealistically large discharge fluxes are required to drive subglacial plumes through shallow pycnocline and to the fjord surface.

I expand on these insights to explore environmental controls on seasonal terminus positions at a suite of tidewater glaciers in central west Greenland. Previously, we have critically lacked comparative studies that quantify and attribute terminus changes to individual forcing mechanisms, such as ocean temperature, meltwater runoff production, and sea ice, and in different glacier settings. I demonstrate that seasonal terminus positions are more sensitive to increases in runoff, than to mélange coverage or ocean

thermal forcing in the proglacial fjord. The strength of this relationship varies between two glacier types based on their outlet geometry and calving style. At tidewater glaciers that calve primarily through small-magnitude (1-10's of meters) serac failure events, localized retreat from submarine melting strongly determines seasonal terminus cycles through the formation of calving embayments around subglacial plumes. Additionally, seasonal terminus advance better corresponds to runoff cessation and the slowdown of frontal ablation through submarine melting than mélange formation and the inhibition of terminus calving. In contrast, deep termini susceptible to buoyancy forces calve through large magnitude (10-100's of meters) slab-rotation or tabular rift events that are less dependent on runoff variations. Comparatively, these glaciers are most likely to respond to mélange conditions. Ocean thermal forcing plays a secondary role in determining seasonal terminus positions and its impact is contingent on entrainment in buoyant subglacial plumes [*Motyka et al*., 2013].

5.3. Future Directions

The research in this dissertation opens several critical questions currently impeding forecasts of dynamic mass loss from the GrIS. In particular, a full understanding of the mechanical coupling between melt-driven terminus undercutting and calving remains elusive. Better constraints on this critical relationship requires more comprehensive and high-spatiotemporal resolution field monitoring, combining multibeam echo surveys of the submarine terminus face with ice flow measurements from ground-based interferometric radar and oceanographic observations in the

proglacial fjord. Similarly, while recent studies have taken holistic approaches to modeling the effect of submarine melting on terminus position changes over time (e.g. *Rignot et al*., 2016b), more detailed frontal ablation budgets are needed to evaluate the varying importance of submarine melting versus calving in time and space. While frontal ablation is relatively easy to measure using remote sensing observations of terminus positons and ice velocities, the independent components of melting and calving must be identified to build a complete process understanding of terminus mass loss for use in numerical models. Such budgets could be achieved through the installation of time lapse cameras to capture terminus calving and velocity and near-terminus weather stations to estimate runoff forcing a subglacial plume model over an entire melt season.

Several transformative applications of the existing multibeam sonar dataset remain. First, the vertical variation in submarine melting may be inferred along terminus profiles assuming the terminus is in a steady state shape and ice velocity does not vary with depth [e.g. *Slater et al*., 2017]. With knowledge of the terminus face slope, θ, and terminus velocity, v, the vertical variation in melt rate can be calculated as $\dot{m} = v(\sin\theta)$, where high curvature along the terminus profile indicates rapidly changing melt rates with depth [*Slater et al*., 2017]. This method does not rely on entrainment parameterizations and thus presents a potentially impactful comparison for plume models. Additionally, investigations of vertically-varying surface roughness along the submarine terminus face may further constrain and distinguish frontal ablation processes acting there, particularly if calving manifests rougher textures in comparison to smooth submarine melting surfaces.

References

Amundson, J. M., M. Fahnestock, M. Truffer, J. Brown, Lüthi MP, and R. J. Motyka (2010), Ice mélange dynamics and implications for terminus stability, Jakobshavn Isbrae, Greenland, *J. Geophys. Res.*, *115*, F01005.

Andrews, L. C., G. A. Catania, M. J. Hoffmann, J. D. Gulley, M. P. Luthi, C. Ryser, R. L. Hawley, and T. A. Neumann (2014), Direct observations of evolving subglacial drainage beneath the Greenland Ice Sheet, *Nature*, *514*, 80-83, doi:10.1038/nature13796.

Bartholomaus, T. C., C. Larsen, and S. O'Neel (2013), Does calving matter? Evidence for significant submarine melt, *Earth and Plan. Sci. Lett.*, *380*, 21–30.

Bartholomaus, T. C., and J. Bassis (2014), Progress and challenges to understanding iceberg calving around the Greenland Ice Sheet, *US CLIVAR VARIATIONS*, *12*, 2, 40-45.

Bartholomaus, T. C., L. A. Stearns, D. A. Sutherland, E. L. Shroyer, J. D. Nash, R. T. Walker, G. Catania, D. Felikson, D. Carroll, M. J. Fried, B. P. Y. Noel, and M. R. van den Broeke (2016), Contrasts in the response of adjacent fjords and glaciers to ice-sheet surface melt in west Greenland, *Ann. Glaciol.*, *57*, 73, 25-38.

Brinkerhoff, D., M. Truffer, and A. Aschwanden (2017), Sediment transport drives tidewater glacier periodicity, *Nat. Commun.*, *8*, 90.

Carr, J. R., A. Vieli, and C. Stokes (2013), Influence of sea ice decline, atmospheric warming, and glacier width on marine-terminating outlet glacier behavior in northwest Greenland at seasonal to interannual time scales, *J. Geophys. Res. Earth Surf.*, *118*, 1210–1226, doi:10.1002/jgrf.20088.

Carr, J. R., C. Stokes, and A. Vieli (2014), Recent retreat of major outlet glaciers on Novaya Zemlya, Russian Arctic, influenced by fjord geometry and sea-ice conditions, *J. Glaciol.*, *60*, 219, 155-170.

Carroll, D., D. A. Sutherland, E. L. Shroyer, J. D. Nash, G. Catania, and L. A. Stearns (2015), Modeling turbulent subglacial meltwater plumes: implications for fjord-scale buoyancy-driven circulation, *J. Phys. Oceanog.*, *45*, 2169-2185.

Carroll, D., D. A. Sutherland, B. Hudson, T. Moon, G. A. Catania, E. L. Shroyer, J. D. Nash, T. C. Bartholomaus, D. Felikson, L. A. Stearns, B. P. Y. Noël, and M. R. van den Broeke (2016), The impact of glacier geometry on meltwater plume structure and submarine melt in greenland fjords, *Geophys. Res. Lett.*, *43*, 18, 9739-9748.

Cassotto, R., M. Fahnestock, J. M. Amundson, M. Truffer, and I. Joughin (2015), Seasonal and interannual variations in ice melange rigidity and its impact on terminus stability, Jakobshavn Isbrae, Greenland, *J. Glaciol.*, *61*, 225, 76–88.

Catania, G. A., and T. A. Neumann (2010), Persistent englacial drainage features in the Greenland Ice Sheet, *Geophys. Res. Lett.*, *37*, L02501.

Catania, G. A., L. A. Stearns, D. A. Sutherland, M. J. Fried, T. C. Bartholomaus, M. Morlighen, E. Shroyer, and J. Nash (in press), Geometric controls on tidewater glacier retreat in central western Greenland, *J. Geophys. Res. Earth Surf.*

Chauché, N., A. Hubbard, J.-C. Gascard, J. E. Box, R. Bates, M. Koppes, A. Sole, P. Christoffersen, and H. Patton (2014), Ice–ocean interaction and calving front morphology at two west Greenland tidewater outlet glaciers, *Cryosphere*, *8*, 1457–1468.

Chu, V. W., L. C. Smith, A. K. Rennermalm, R. R. Forster, and J. E. Box (2012), Hydrologic controls on coastal suspended sediment plumes around the Greenland Ice Sheet, *Cryosphere*, *6*, 1–19.

Cook, S., T. Zwinger, I. C. Rutt, S. O'Neel, and T. Murray (2012), Testing the effect of water in crevasses on a physically based calving model, *Ann. Glaciol*,. *53*, 90–96. doi: 10.3189/2012AoG60A107.

Cook, S., I. C. Rutt, T. Murray, A. Luckman, T. Zwinger, N. Selmes, A. Goldsack, and T.D. James (2014), Modelling environmental influences on calving at Helheim Glacier in eastern Greenland, *Cryosphere*, *8*, 827–841. doi: 10.5194/tc-8-827-2014.

Cooks, A. J., P. R. Holland, M. P. Meredith, T. Murray, A. Luckman, and D. G. Vaughan (2016), Ocean forcing of glacier retreat in the western Antarctic Peninsula, *Science*, *353*, 6296, 283-286.

Csatho, B. M., A. F. Schenk, C. J. van der Veen, G. Babonis, K. Duncan, S. Rezvanbehnahani, M. R. van den Broeke, S. B. Simonsen, S. Nagarajan, and J. H. van Angelen (2014), Laser altimetry reveals complex pattern of Greenland ice sheet dynamics, *Proc. Natl. Acad. Sci. U.S.A.*, *111*, 52, 18478–18483.

Cuffey, K., and W. Paterson (2010), The physics of glaciers 4th edition, Butterworth-Heinemann, Burlington, MA.

Davison, A. C. and D. V. Hinkley, Bootstrap Methods and their Applications. Cambridge University Press Cambridge, Cambridge Series in Statistical and Probabilistic Mathematics, 1997.

De Juan, J., P. Elosegui, M. Nettles, T. B. Larsen, J. L. Davis, G. S. Hamilton, L. A. Stearns, M. L. Andersen, G. Ekstrom, A. P. Ahlstrom, L. Stenseng, S. Abbas Khan, and R. Forsberg (2010), Sudden increase in tidal response linked to calving and acceleration at a large Greenland outlet glacier, *Geophys. Res. Lett.*, *37*, L12501.

Enderlin, E. M., I. M. Howat, S. Jeong, M. J. Noh, J. H. Angelen, and M. R. Broeke (2014), An improved mass budget for the Greenland ice sheet, *Geophys. Res. Lett.*, *41*, 866–872.

Ettema, J., M. R. van den Broeke, E. van Meijgaard, W. J. van de Berg, J. L. Bamber, J. E. Box, and R. C. Bales (2009), Higher surface mass balance of the Greenland Ice Sheet revealed by high-resolution climate modeling, *J. Geophys. Res*., *36*, L12501, doi:10.1029/2009GL038110.

Fahnestock, M., T. Scambos, T. Moon, A. Gardner, T. Haran, and M. Klinger (2015), Rapid large-area mapping of ice flow using Landsat 8, *Remote Sens. Environ.*, *185*, 84-94.

Felikson, D., T. C. Bartholomaus, G. A. Catania, N. J. Korsgaard, K. H. Kjaer, M. Morlighem, B. Noel, M. van den Broeke, L. A. Stearns, E. L. Shroyer, D. A. Sutherland, and J. D. Nash (2017), Inland thinning on the Greenland Ice Sheet controlled by outlet glacier geometry, *Nat. Geosci.*, *10*, 366-369.

Fofonoff, P., and R. C. Millard (1983), Algorithms for computation of fundamental properties of seawater, Unesco Tech. Pap. in Mar. Sci., 44, Division of Marine Sciences, Unesco, Place de Fontenoy, Paris, France.

Fried, M. J., G. A. Catania, T. C. Bartholomaus, D. Duncan, M. Davis, L. A. Stearns, J. Nash, E. Shroyer, and D. Sutherland (2015), Distributed subglacial discharge drives significant submarine melt at a Greenland tidewater glacier, *Geophys*. *Res. Lett.*, *42*, 21, 9328–9336.

Holland, D. M., R. Thomas, B. de Young, M. H. Ribergaard, and B. Lyberth (2008), Acceleration of Jakobshavn Isbrae triggered by warm subsurface ocean waters, *Nat. Geosci.*, *1*, 10, 659-664.

Holland, D. M., and A. Jenkins (1999), Modeling thermodynamic ice-ocean interactions at the base of an ice shelf, *J. Phys. Oceanogr*., *29*, 8, 1787–1800.

Howat, I. M., I. Joughin, M. Fahnestock, B. E. Smith, and T. Scambos (2008), Synchronous retreat and acceleration of southeast Greenland outlet glaciers 2000–2006: ice dynamics and coupling to climate, *J. Glaciol*., *54*, 187, 646–660.

Howat, I., J. Box, Y. Ahn, A. Herrington, and E. McFadden (2010), Seasonal variability in the dynamics of marine-terminating outlet glaciers in Greenland, *J. Glaciol.*, *56*, 198, 601–613.

Howat, I.M., and A. Eddy (2011), Multi-decadal retreat of Greenland's marine-terminating glaciers, *J. Glaciol., 57*, 203, 389-396.

Howat, I. 2017. *MEaSUREs Greenland Ice Velocity: Selected Glacier Site Velocity Maps from Optical Images, Version 2*. [subsets: W69.95N, W70.55N, W70.90N, W71.25N, W71.65N, W72.00N]. Boulder, Colorado USA. NASA National Snow and Ice Data Center Distributed Active Archive Center. [accessed July 2017].

Howat, I. M., A. Negrete, and B. E. Smith (2014), The Greenland Ice Mapping Project (GIMP) land classification and surface elevation datasets, *Cryosphere*, *8*, 453–478.

Inall, M. E., T. Murray, F. R. Cottier, K. Scharrer, T. J. Boyd, K. J. Heywood, and S. L. Bevan (2014), Oceanic heat delivery via kangerdlugssuaq fjord to the south-east greenland ice sheet, *J. Geophys. Res. Oceans*, *119*, 631–645, doi:10.1002/2013JC009295.

Jackson, R. H., F. Straneo, and D. A. Sutherland (2014), Externally forced fluctuations in ocean temperature at Greenland glaciers in non-summer months, *Nat. Geosci.*, *7*, 503-508.

Jackson, R. H., E. L. Shroyer, J. D. Nash, D. A. Sutherland, D. Carroll, M. J. Fried, G. A. Catania, T. C. Bartholomaus, and L. A. Stearns (2017), Near-glacier surveying of a subglacial discharge plume: Implications for plume parameterizations, *Geophys. Res. Lett*., *44*, 6886–6894, doi:10.1002/2017GL073602.

James, T. D., T. Murray, N. Selmes, K. Scharrer, and M. E. O'Leary (2014), Buoyant flexure and basal crevassing in dynamic mass loss at Helheim Glacier, *Nat. Geosci.*, *7*, 593–596.

Jenkins, A. (2011), Convection-driven melting near the grounding lines of ice shelves and tidewater glaciers, *J. Phys. Oceanogr.*, *41*, 2279–2294.

Joughin, I., S. B. Das, M. A. King, B. E. Smith, I. M. Howat, and T. Moon (2008), Seasonal speedup along the western flank of the Greenland Ice Sheet, *Science*, *320*, 781-783.

Joughin, I., B. Smith, I. Howat, T. Scambos, and T. Moon (2010), Greenland Flow Variability from Ice-Sheet-Wide Velocity Mapping, *J. Glaciol*., *56*, 415-430.

Joughin, I., I. Howat, B. Smith, and T. Scambos (2011, updated 2016). *MEaSUREs Greenland Ice Velocity: Selected Glacier Site Velocity Maps from InSAR, Version 1*. [subsets: W69.95N, W70.55N, W70.90N, W71.25N, W71.65N, W72.00N]. Boulder, Colorado USA. NASA National Snow and Ice Data Center Distributed Active Archive Center. [accessed July 2017].

Joughin, I., B. E. Smith, I. M. Howat, D. Floricioiu, R. B. Alley, M. Truffer, and M. Fahnestock (2012), Seasonal to decadal scale variations in the surface velocity of Jakobshavn Isbrae, Greenland: Observation and model-based analysis, *J. Geophys. Res*., *117*, F02030, doi:10.1029/2011JF002110.

Kimura, S., P. R. Holland, A. Jenkins, and M. Piggot (2014), The effect of meltwater plumes on the melting of a vertical glacier face. *J. Phys. Oceanogr*, *44*, 3099–3117.

Klinck, J. M., J. J. O'Brien, and H. Svendsen (1981), A simple model of fjord and coastal circulation interaction, *J. Phys. Oceanogr*., *11*, 1612–1626.

Kjeldsen, K. K., N. J. Korsgaard, A. A. Bjork, S. A. Khan, J. E. Box, S. Funder, N. K. Larsen, J. L. Bamber, W. Colgan, M. van den Broeke, M. Siggard-Andersen, C. Nuth, A. Schomacker, C. S. Andresen, E. Willerslev, and K. H. Kjaer (2015), Spatial and temporal distribution of mass loss from the Greenland ice sheet since AD 1900, *Nature*, *528*, 396-400.

Luckman, A., T. Murray, R. De Lange, and E. Hanna (2006), Rapid and synchronous ice dynamic changes in East Greenland, *Geophys. Res. Lett*., *33*, L03503, 10.1029/2005GL025428.

Luckman, A., D. I. Benn, F. Cottier, F. Nilsen, and M. Inall (2015), Calving rates at tidewater glaciers vary strongly with ocean temperature, *Nat. Commun.*, *6*, 8566.

MacGregor, J. A., G. A. Catania, M. S. Markowski, and A. G. Andrews (2012), Widespread rifting and retreat of ice-shelf margins in the eastern Amundsen Sea Embayment between 1972 and 2011, *J. Glaciol.*, *58*, 209, 458–466.

McFadden, E., I. Howat, I. Joughin, B. E. Smith, and Y. Ahn (2011), Changes in the dynamics of marine terminating outlet glaciers in west Greenland (2000-2009), *J. Geophys. Res.*, *116*, F02022.

McMillan, M., A. Leeson, A. Shepherd, K. Briggs, T. W. K. Armitage, A. Hogg, P. K. Munneke, M. van den Broeke, B. Noel, W. J. van de Berg, S. Ligtenberg, M. Horwath, A. Groh, A. Muir, and L. Gilbert (2016), A high-resolution record of Greenland mass balance, *Geophys. Res. Lett.*, *43*, 7002-7010.

McNabb, R. W., and R. Hock (2014), Alaska tidewater glacier terminus positions, 1948-2012, *J. Geophys. Res. Earth Surf.*, *119*, 2, 153–167.

Medrzycka, D., D. Benn, J. E. Box, L. Copeland, and J. Balog (2016), Calving behavior at Rink Isbrae, West Greenland, from time-lapse photos, *Arc, Ant and Alpine Res*, *48*, 163-278.

Meier, M. F and A. Post (1987), Fast tidewater glaciers. *J. Geophys. Res*., 92, B9, 9051-9058.

Mercer, J. H. (1961), The response of fjord glaciers to changes in the firn limit, *J. Glaciol*., 3, 850–858.

Moon, T., and I. Joughin (2008), Changes in ice front positions on Greenland's outlet glaciers from 1992 to 2007, *J. Geophys. Res.*, *113*, F02022.

Moon, T., I. Joughin, B. Smith, M. R. van den Broeke, W. J. van de Berg, B. Noël, and M. Usher (2014), Distinct patterns of seasonal Greenland glacier velocity, *Geophys. Res. Lett.*, *41*, 7209-7216.

Moon, T., I. Joughin, and B. E. Smith (2015), Seasonal to multiyear variability of glacier surface velocity, terminus position, and sea ice/ice mélange in northwest Greenland, *J. Geophys. Res. Earth Surf.*, *120*, 818–833.

Morlighem, M., E. Rignot, J. Mouginot, H. Seroussi, and E. Larour (2014), Deeply incised submarine glacial valleys beneath the Greenland Ice Sheet, *Nat. Geosci.*, *7*, 418-422.

Morlighem, M., C. Williams, E. Rignot, L. An, J. E. Arndt, J. Bamber, G. Catania, N. Chauché, J. A. Dowdeswell, B. Dorschel, I. Fenty, K. Hogan, I. Howat, A. Hubbard, M. Jakobsson, T. M. Jordan, K. K. Kjeldsen, R. Millan, L. Mayer, J. Mouginot, B. Noël, C. O'Cofaigh, S. J. Palmer, S. Rysgaard, H. Seroussi, M. J. Siegert, P. Slabon, F. Straneo, M. R. van den Broeke, W. Weinrebe, M. Wood, and K. Zinglersen (2017), BedMachine v3: Complete bed topography and ocean bathymetry mapping of Greenland from multi-beam echo sounding combined with mass conservation, *Geophys. Res. Lett*., *44*, 21.

Mortensen, J., K. Lennert, J. Bendtsen, and S. Rysgaard (2011), Heat sources for glacial melt in a sub-Arctic fjord (Godthabsfjord) in contact with the Greenland Ice Sheet, *J. Geophys. Res.*, *116*, C1, C01013.

Motyka, R., L. Hunter, K. Echelmeyer, and C. Connor (2003), Submarine melting at the terminus of a temperate tidewater glacier, LeConte Glacier, Alaska, USA., *Ann. Glaciol.*, *36*, 57–65.

Motyka, R., M. Truffer, M. Fahnestock, J. Mortenson, S. Rysgaard, and I. Howat (2011), Submarine melting of the 1985 Jakobshavn Isbrae floating ice tongue and the triggering of the current retreat, *J. Geophys. Res.*, *116*, F01007.

Motyka, R., W. P. Dryer, J. Amundson, M. Truffer, and M. Fahnestock (2013), Rapid submarine melting driven by subglacial driven by subglacial discharge, LeConte Glacier, Alaska, *Geophys. Res. Lett.*, *40*, 5153-5158.

Motyka, R. J., R. Cassotto, M. Truffer, K. K. Kjeldsen, D. van As, N. J. Korsgaard, M. Fahnestock, I. Howat, P. L. Langen, J. Mortensen, K. Lennert, and S. Rysgaard (2017), Asynchronous behavior of outlet glaciers feeding Godthabsfjord (Nuup Kangerlua) and the triggering of Narsap Sermia's retreat in SW Greenland, *J. Glaciol.*, *63*, 238, 288-308.

Murray, T., K. Scharrer, T. D. James, S. R. Dye, E. Hanna, A. D. Booth, N. Selmes, A. Luckman, A. L. C. Hughes, S. Cook, and P. Huybrechts (2010), Ocean regulation hypothesis for glacier dynamics in southeast Greenland and implications for ice sheet mass changes, *J. Geophys. Res.*, *115*, F03026.

Murray, T., K. Scharrer, N. Selmes, A. D. Booth, T. D. James, S. L. Bevan, J. Bradley, S. Cook, L. Cordero Llana, Y. Drocourt, L. Dyke, A. Goldsack, A. L. Hughes, A. J. Luckman, and J. McGovern (2015a), Extensive retreat of Greenland tidewater glaciers, 2000-2010, *Arc, Ant and Alpine Res*, *47*, 427-447.

Murray, T., N. Selmes, T. D. James, S. Edwards, I. Martin, T. O'Farrell, R. Aspey, I. Rutt, M. Nettles, and T. Bauge (2015b), Dynamics of glacier calving at the ungrounded margin of Helheim Glacier, southeast Greenland, *J. Geophys. Res. Earth Surf.*, *120*, 964–982.

Noh, M. J. and I. M. Howat (2015), Automated stereo-photogrammetric DEM generation at high latitudes: Surface Extraction from TIN-Based Search Minimization (SETSM) validation and demonstration over glaciated regions, *GIScience and Rem. Sens., 52*, 198-217.

Nick, F. M., A. Vieli, I. M. Howat, and I. Joughin (2009), Large-scale changes in Greenland outlet glacier dynamics triggered at the terminus, *Nat. Geosci.*, *2*, 110–114.

Nilsen, F., F. Cottier, R. Skogseth, and S. Mattsson (2008), Fjord-shelf exchanges controlled by ice and brine production: The interannual variation of Atlantic Water in Isfjorden, Svalbard, *Cont. Shelf Res.*, *28*, 1838–1853, doi:10.1016/j.csr.2008.04.015.

Noël, B., W. J. van de Berg, J. M. van Wessem, E. van Meijgaard, D. van As, J. T. M. Lenaerts, S. Lhermitte, P. K. Munneke, C. J. P. Paul Smeets, L. H. van Ulft, R. S. W. van Wal, and M. R van den Broeke (2018), Modelling the climate and surface mass balance of polar ice sheets using RACMO2, Part 1: Greenland (1958-2016), *Cryosphere*, *12*, 811-831.

O'Leary, M., and P. Christoffersen (2013), Calving on tidewater glaciers amplified by submarine frontal melting, *Cryosphere*, *7*, 119–128.

Pedersen, F. B. (1980), Dense bottom currents in rotating ocean, *J. Hydraul. Div.*, *106*, 1291–1308.

Pfeffer, W. T. (2007), A simple mechanism for irreversible tidewater glacier retreat, *J. Geophys. Res.*, *112*, F03S25, doi:10.1029/2006JF000590.

Powell, R. D. (1991), Grounding-line systems as second-order controls on fluctuations of tidewater termini of temperate glaciers, *in* Anderson, J. B., and Ashley, G. M., eds.. Glacial marine sedimentation; Paleoclimatic significance: Boulder, Colorado, Geological Society of America Special Paper 261.

Rosenau, R., M. Scheinert, and R. Dietrich (2015), A processing system to monitor Greenland outlet glacier velocity variations at decadal and seasonal time scales utilizing the Landsat imagery. *Remote Sens. Environ.*, *169*, 1-19, doi: 10.1016/j.rse.2015.07.012 [accessed July 2017].

Rignot, E., M. Koppes, and I. Velicogna (2010), Rapid submarine melting of the calving faces of west greenland glaciers, *Nat. Geosci.*, *3*, 187–191.

Rignot, E., I. Velicogna, M. R. van den Broeke, A. Monaghan, A and J. Lenaerts (2011), Acceleration of the contribution of the Greenland and Antarctic ice sheets to sea level rise, *Geophys. Res. Lett., 38*, L05503.

Rignot, E., I. Fenty, Y. Xu, C. Cai, and C. Kemp (2015), Undercutting of marine-terminating glaciers in West Greenland, *Geophys. Res. Lett.*, *42*, 5909–5917.

Rignot, E., I. Fenty, Y. Xu, C. Cai, I. Velicogna, C. O. Cofaigh, J. A. Dowdeswell, W. Weinrebe, G. Catania, and D. Duncan (2016a), Bathymetry data reveal glaciers vulberable to ice-ocean interaction in Uummannaq and Vaigat glacial fjords, west Greenland, *Geophys. Res. Lett.*, *43*, 2667-2674.

Rignot, E., Y. Xu, D. Menemenlis, J. Mouginot, B. Scheuchl, X. Li, M. Morlighem, H. Seroussi, M. van den Broeke, I. Fenty, C. Cai, L. An, and B. de Fleurian (2016b), Modeling of ocean-induced ice melt rates of five West Greenland glaciers over the past two decades, *Geophys. Res. Lett.*, *43*, 6374-6382.

Scambos, T., M. Fahnestock, T. Moon, A. Gardner, and M. Klinger (2016), *Global Land Ice Velocity Extraction from Landsat 8 (GoLIVE), Version 1*. [subsets: p009_r010, p011_r011, p012_r009]. Boulder, Colorado USA. NSIDC: National Snow and Ice Data Center. doi: http://dx.doi.org/10.7265/N5ZP442B. [accessed July 2017].

Schild, K. M., and G. S. Hamilton (2013), Seasonal variations of outlet glacier terminus position in Greenland, *J. Glaciol.*, *59*, 216, 759-770.

Schoof, C. (2010), Ice-sheet acceleration driven by melt supply variability, *Nature*, *468*, 7325, 803-806.

Sciascia, R., F. Straneo, C. Cenedese, and P. Heimbach (2013), Seasonal variability of submarine melt rate and circulation in an East Greenland fjord, *J. Geophys. Res. Oceans*, *118*, 2492–2506.

Seale, A., P. Christoffersen, R. I. Mugford, and M. O'Leary (2011), Ocean forcing of the Greenland Ice Sheet: Calving fronts and patterns of retreat identified by automatic satellite monitoring of eastern outlet glaciers, *J. Geophys. Res. 116*, F03013.

Shepherd, A., and 46 others (2012), A reconciled estimate of ice-sheet mass balance, *Science*, *338*, 1183–1189.

Shreve, R. L. (1972), Movement of water in glaciers, *J. Glaciol.*, *11*, 62, 205-214.

Shroyer, E. L., L. Padman, R. M. Samelson, A. Munchow, and L. A. Stearns (2017), Seasonal control of ice-shelf melt by the ocean's response to sea-ice cover in Nares Strait, *J. Glaciol*., *63*, 238), 324-330.

Sikonia, W.G. and A. Post (1980), Columbia Glacier, Alaska; recent ice loss and its relationship to seasonal terminal embayments, thinning, and glacial flow, *U.S. Geological Survey Hydrologic Investigations Atlas, 619*, 1-3.

Slater, D. A., P. W. Nienow, T. R. Cowton, D. N. Goldberg, and A. J. Sole (2015), Effect of near-terminus subglacial hydrology on tidewater glacier submarine melt rates, *Geophys. Res. Lett.*, *42*, 2861-2868.

Slater, D. A., P. W. Nienow, D. N. Goldberg, T. R. Cowton, and A. J. Sole (2017), A model for tidewater glacier undercutting by submarine melt, *Geophys. Res. Lett., 44*, 2360-2368.

Smith, L. C., V. W. Chu, K. Yang, C. J. Gleason, L. H. Pitcher, A. K. Rennermalm, C. L. Legleiter, A. E. Behar, B. T. Overstreet, S. E. Moustafa, M. Tedesco, R. R. Forster, A. L. LeWinter, D. C. Finnegan, Y. Sheng, and J. Balog (2015), Efficient meltwater drainage through supraglacial streams and rivers on the southwest Greenland ice sheet, *Proc. Natl. Acad. Sci. U.S.A.*, *112*, 1001-1006.

Straneo, F., G. S. Hamilton, D. A. Sutherland, L. A. Stearns, F. Davidson, M. O. Hammill, G. B. Stenson, and A. Rosing-Asvid (2010), Rapid circulation of warm tropical waters in a major, East Greenland glacial fjord, *Nat. Geosci.*, *3*, 182-186.

Straneo, F., R. Curry, D. A. Sutherland, G. Hamilton, C. Cenedese, K. Vage, and L. A. Stearns (2011), Impact of fjord dynamics and glacial runoff on the circulation near Helheim Glacier, *Nat. Geosci. 4*, 322–327.

Straneo, F., and P. Heimbach (2013), North Atlantic warming and the retreat of Greenland's outlet glaciers, *Nature*, *504*, 36-43.

Straneo, F., P. Heimbach, O. Sergienko, G. Hamilton, G. Catania, S. Griffies, R. Hallberg, A. Jenkins, I. Joughin, R. Motyka, W. T. Pfeffer, S. F. Price, E. Rignot, T. Scambos, M. Truffer, and A. Vieli (2013), Challenges to understanding the dynamic response of Greenland's marine terminating glaciers to oceanic and atmospheric forcing, *Bull. Amer. Meteor. Soc.*, *94*, 1131-1144.

Straneo, F., and C. Cenedese (2015), The dynamics of Greenland's glacial fjords and their role in climate, *Ann. Rev. Marine Sci., 7*, 89-112.

Sutherland, D. A., F. Straneo, and R. S. Pickart (2014), Characteristics and dynamics of two major Greenland glacial fjords, *J. Geophys. Res. Oceans*, *119*, 3767–3791, doi:10.1002/2013JC009786.

Todd, J., and P. Christoffersen (2014), Are seasonal calving dynamics forced by buttressing from ice mélange or undercutting by melting? Outcomes from full-Stokes simulations of Store Glacier, West Greenland, *Cryosphere*, *8*, 2353–2365.

Turner, J. S. (1979), Buoyancy Effects in Fluids, Cambridge Univ. Press, Cambridge, U. K.

Truffer, M., and R. Motyka (2016), Where glaciers meet water: Subaqueous melt and its relevance to glaciers in various settings, *Rev. Geophys*., *54*, 220-239.

van den Broeke, M. R., J. Bamber, J. Ettema, E. Rignot, E. Schrama, W. J. van de Berg, E. van Meijgaard, I. Velicogna, and B. Wouters (2009), Partitioning recent Greenland mass loss, *Science*, 326, 984–986.

van den Broeke, M. R., E. M. Enderlin, I. A. Howat, P. K. Munneke, B. P. Y. Noël, W. J. van de Berg, E. van Meijgaard, and B. Wouters (2016), On the recent contribution of the Greenland ice sheet to sea level change, *Cryosphere*, *10*, 1933-1946.

van der Veen, C. J. (1996), Tidewater calving, *J. Glaciol.*, *42*, 375–385.

Velicogna, I. (2009), Increasing rates of ice mass loss from the Greenland and Antarctic ice sheets revealed by GRACE, *Geophys. Res. Lett., 36*, 19.

Velicogna, I., T. C. Sutterley, and M. R. van den Broeke (2014), Regional acceleration in ice mass loss from Greenland and Antarctica using GRACE time-variable gravity data, *J. Geophys. Res. Space Phys.*, *41*, 8130–8137.

Vieli, A., M. Funk, and H. Blatter (2001), Flow dynamics of tidewater glaciers: a numerical modelling approach, *J. Glaciol.*, *47*, 159, 595-606.

Wagner, T. J. W., T. D. James, T. Murray, and D. Vella (2016), On the role of buoyant flexure in glacier calving, *Geophys. Res. Lett.*, *43*, 232-240.

Walter, J. I., J. E. Box, S. Tulaczyk, E. E. Brodsky, I. M. Howat, Y. Ahn, and A. Brown (2012), Oceanic mechanical forcing of a marine-terminating Greenland glacier, *Ann. Glaciol.*, *53*, 60, 181–192.

Xu, Y., E. Rignot, D. Menemenlis, and M. Koppes (2012), Numerical experiments on subaqueous melting of Greenland tidewater glaciers in response to ocean warming and enhanced subglacial discharge, *Ann. Glaciol., 53*, 60, 229–234.

Xu, Y., E. Rignot, D. Menemenlis, and M. Mar Flexas (2013), Subaqueous melting of Store Glacier, west Greenland from three-dimensional, high-resolution numerical modeling and ocean observations, *Geophys. Res. Lett., 40*, 17, 4648-4653.